Variational time integrators in computational solid mechanics

Thesis by

Adrián Lew

In Partial Fulfillment of the Requirements

for the Degree of

Doctor of Philosophy

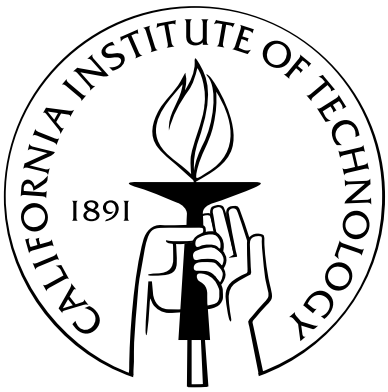

California Institute of Technology

Pasadena, California

2003

(Defended May 21, 2003)

To

Patry,

Jorge and Diana,

Melisa and Damián,

Manolo Tarchitzky

Acknowledgements

I have greatly enjoyed my years at Caltech, not only because of the sunny beaches and close ski resorts of Southern California, but fundamentally because of the group of people with whom I shared these years. Having Michael Ortiz as thesis advisor has been a very enjoyable and fruitful experience. He has encouraged me to work on topics I had never before imagined I would, has taught me to be fearless of innovation and avid of self-renovation, and has been a constant driving force to embrace the scientific endeavor with passion and enthusiasm. I am deeply thankful for his guidance and support. I have also been very fortunate to meet Jerry Marsden at an early stage of my thesis work. He has certainly been and is a model to follow and look up to, but most importantly, it has always been a fascinating experience to talk and listen to him and to participate of the various activities his diverse range of interest generate. His characteristic research and writing style has definitively shaped my career. Professor Ravichandran has been the experienced mentor and friend I needed when planning my future steps. His dedication to mentoring students is truly an example I expect to follow. I would like to thank him for his guidance and support, and I am looking forward to continue listening more of his anecdotes in the future.

I would like to thank Kaushik Bhattacharya and Rob Phillips for the many interesting discussions we had during these years. Having Deborah Sulsky, Matt West, Raul Radovitzky, Patrizio Neff, Kyle Caspersen, Mark Scheel, Lee Lindblom, Matías Zielonka and Johannes Zimmer as collaborators has made research only more fun and interesting, and the long hours spent on it more enjoyable. I expect to continue our collaboration and friendship in the future. Deborah and Raul have also acted as mentors at different stages, and I would like to thank them for that. I will miss the afternoon strolls to the coffee house with my officemates in the room at the basement: Bill, John, Matt, Matias and Olga, and formerly Marisol, Enzo, Olivier, Puru and Rena. Marta and Lydia truly deserve separate credits, they have always showed patience and responsiveness whenever I rushed for their help. During these years I have enjoyed innumerable visits to the Athenaeum, outdoor adventures and sports with Julian, Florian, Alex and Pedro. They have generously offered me their friendship since the first day I arrived to the US, and made me feel at home away from home.

I am ultimately indebted to my family, my parents Jorge and Diana and my siblings Melisa and Damián, who have always been a source of unconditional support and encouragement. Their love

has provided me with the enthusiasm to face new projects and constantly seek novel challenges. I just want to thank them for that.

My wife, Patricia, has been my secret source of support, enthusiasm and optimism. I am immensely grateful to her for having filled my life of love, joy and happiness.

Abstract

This thesis develops the theory and implementation of variational integrators for computational solid mechanics problems, and to some extent, for fluid mechanics problems as well. Variational integrators for finite dimensional mechanical systems are succinctly reviewed, and used as the foundations for the extension to continuum systems. The latter is accomplished by way of a space–time formulation for Lagrangian continuum mechanics that unifies the derivation of the balance of linear momentum, energy and configurational forces, all of them as Euler-Lagrange equations of an extended Hamilton's principle. In this formulation, energy conservation and the path independence of the J- and L-integrals are conserved quantities emanating from Noether's theorem. Variational integrators for continuum mechanics are constructed by mimicking this variational structure, and a discrete Noether's theorem for rather general space–time discretizations is presented. Additionally, the algorithms are automatically (multi)symplectic, and the (multi)symplectic form is uniquely defined by the theory. For instance, in nonlinear elastodynamics the algorithms exactly preserve linear and angular momenta, whenever the continuous system does.

A class of variational algorithms is constructed, termed *asynchronous variational integrators* (AVI), which permit the selection of independent time steps in each element of a finite element mesh, and the local time steps need not bear an integral relation to each other. The conservation properties of both synchronous and asynchronous variational integrators are discussed in detail. In particular, AVI are found to nearly conserve energy both locally and globally, a distinguishing feature of variational integrators. The possibility of adapting the elemental time step to exactly satisfy the local energy balance equation, obtained from the extended variational principle, is analyzed. The AVI are also extended to include dissipative systems. The excellent accuracy, conservation and convergence characteristics of AVI are demonstrated via selected numerical examples, both for conservative and dissipative systems. In these tests AVI are found to result in substantial speedups, at equal accuracy, relative to explicit Newmark.

In elastostatics, the variational structure leads to the formulation of discrete path-independent integrals and a characterization of the configurational forces acting in discrete systems. A notable example is a discrete, path-independent J-integral at the tip of a crack in a finite element mesh.

Contents

List of Figures

List of Tables

Chapter 1

Introduction and overview

The goal of this thesis is to present a new framework and a fresh perspective on the formulation of computational algorithms for solid and fluid mechanics. Despite the undeniable success of the finite element and related methods, the quest for building virtual laboratories where virtual experiments could be performed demands the careful crafting of newer and more powerful algorithms, but most importantly, it demands the creation of a new level of understanding of mechanics when the continuum is discretized. The theory of Discrete Mechanics has been and is being developed to fulfill this need. In particular, this thesis contains the formulation of the theory for solid mechanics and some fluid mechanics problems.

The cornerstone of the theory of Discrete Mechanics consists of discretizing Hamilton's principle of stationary action in Lagrangian mechanics. While this idea is standard for elliptic problems, in the form of Galerkin and finite element methods (see, e.g., Johnson [1987]), it has only been applied relatively recently to derive variational time stepping algorithms for mechanical systems. We refer to Marsden and West [2001] for an extensive survey of the previous literature, as well as for a detailed overview of the framework for problems described by ordinary differential equations (ODE).

A discrete mechanical system is defined as one for which trajectories can be described with a finite number of parameters. In a nutshell, the theory of Discrete Mechanics prescribes two steps to derive the governing equations for the motion of the discrete mechanical system. The first step consists in postulating an action sum. The second step defines the motion, by stating that it should render the action sum stationary with respect to admissible variations of the trajectory, a fact that is expressed through the *discrete Euler–Lagrange equations* (DEL). For instance, for a system composed of springs and masses an action sum is naturally defined by computing the value of the exact action over piecewise linear trajectories in time with a given time step. For this type of construction, a theorem proved in Marsden and West [2001] states that the discrete trajectories are close to the ones of the continuous mechanical system whenever the discrete action approximates the continuous one. In other words, the DEL equations naturally define an integration algorithm, a *variational integrator*.

The remarkable conservation properties of the resulting algorithms represent perhaps the most profound consequence of the variational structure of the theory. This is precisely stated in the existence of a discrete version of Noether's theorem (see, e.g., Marsden and Ratiu [1994]), namely, there is a conserved quantity associated with each symmetry of the discrete mechanical system. In other words, if one constructs the discrete variational principle to respect the symmetry (such as rotational invariance for angular momentum), then there will be a corresponding conserved quantity that is exactly respected by the discrete algorithm. Of course it is well known (and examples are given in Lew et al. [2003b]) that standard, unstructured, even more highly accurate algorithms do not have this property.

But there is more to the story. In addition to the superb conservation properties, every algorithm constructed from the theory is symplectic (see, e.g., Marsden and West [2001]), in the same way the flow of the continuous system is (see, e.g., Marsden and Ratiu [1994]). Symplectic algorithms have often been observed computationally to possess remarkable near energy preserving behavior, which makes them very attractive for long–time integration. Simplecticity is a statement about the way nearby trajectories of the mechanical system evolve. Liouville's theorem, which states that any open set in phase space is evolved isochorically by the mechanical system, can be regarded as a direct consequence of the symplecticity of the flow of the continuous system. This by itself may seem somewhat mathematical and irrelevant at first sight, but it is the key to understanding the remarkable energy behavior of variational schemes. We shall explain the notion of symplecticity in concrete and easy to understand terms in the text, but it is a deep notion that underlies all of modern geometric mechanics. In particular, through a process called *backward error analysis*, it is the key to understanding this approximate energy conservation. The basic idea is to show that the algorithm is exactly energy conserving (up to exponentially small terms) for a *nearby* Hamiltonian system. This is important work of many people; we refer to Hairer and Lubich [2000] for one of these and to Marsden and West [2001] for additional references.

Variational integrators are symplectic-momentum preserving methods, and under appropriate conditions, they nearly preserve energy. The construction of constant time step symplectic-momentum preserving methods that exactly conserve energy is not possible, according to a result in Ge and Marsden [1988] (the exception being certain integrable systems). It is because of this result that the literature divided into those favoring symplectic-momentum methods and those favoring energy-momentum methods. Amongst the latter, contributions were made by Simo et al. [1992], Gonzalez [1996] and Gonzalez and Simo [1996]. Kane et al. [1999a] circumvented the result in Ge and Marsden [1988] by allowing the time step to change during the computation, in such a way that the energy of the complete system is preserved. The resulting algorithms are symplectic-energy-momentum time integrators for finite degree of freedom mechanical systems (such as the N-body problem or rigid body mechanics). Conditions for the solvability of the time step were investigated there. It is

appropriate to mention, however, that exactly preserving the energy by adjusting the time step is sometimes at conflict with other considerations, such as stability analysis or computational efficiency.

Widely used algorithms can be recast into the discrete mechanics framework, such as some versions of Newmark, as done in Kane et al. [2000]. In molecular dynamics symplectic algorithms are known to perform very well. The ability of variational integrators to capture statistical quantities right has long been known, even in the face of chaotic dynamics where small perturbations can lead to large errors in specific trajectories. A neat example is presented in Lew et al. [2003b] in the computation of the average kinetic energy of a system of interacting particles. The theory sheds light on some of the reasons for the observed good behavior of these algorithms; but fundamentally, it facilitates and guides the construction of integration schemes in nonstandard situations.

The theory is not limited to conservative systems. The extension of the theory to dissipative or forced systems has been carried out in Kane et al. [2000] through the application of the Lagrange-D'alembert variational principle. This guarantees that the discretization of the conservative part of the forces retains good preservation properties, which proves to be fundamental to correctly capturing the dissipation rate in weakly dissipative systems (see Kane et al. [2000]). Additionally, if there are constraints present, then one can still use, very effectively, variational methods. The constraints are realized in terms of the Lagrangian augmented by suitable penalty functions. Variational methods have also been applied to collision algorithms, as in Kane et al. [1999b], Pandolfi et al. [2002], Fetecau et al. [2002] and references therein. The main achievement in these works is to show that properties of variational integrators remain valid right through the collision process.

Chapter 2 reviews the basic aspects of the theory of Discrete Mechanics, briefly described above. We made every effort to provide a description of the theory in simple and elementary terms, directed to those readers who are not very familiar with differential geometry terminology. This chapter, as well as Lew et al. [2003b], are intended to be an introduction to the subject. To fully understand the theory, it is best to work intrinsically on manifolds as opposed to relying on generalized coordinates. We refer the reader to Marsden and West [2001] for the intrinsic version. The chapter also includes a few new components, such as a discussion of when a given algorithm is variational, conditions for a variational algorithm to derive from a minimum principle, and the treatment of two-point constraints, so necessary for solid mechanics applications.

The extension of the idea of variational integrators to the PDE context was made in Marsden et al. [1998]. They showed, in a demonstration example, that the method was very promising for variational integrators in a space–time context. This can be considered to be the starting point of this thesis, where we added several innovative ideas and furthered the theoretical developments to efficiently address continuum mechanics problems, with an emphasis on solid mechanics applications.

The crucial step in carrying over the ideas from the ODE case to continuum mechanics is to switch from discretizing an open set of the real line to discretizing an open set in space–time. The

action sum is constructed by adding contributions from all discrete regions in space–time, normally called discrete Lagrangians, and the trajectories are obtained by applying Hamilton's principle as in the finite–dimensional case. A discrete Noether's theorem is also obtained in this context, having a powerful additional feature. Not only does it guarantee the conservation of global quantities, such as total angular momentum, but it also shows that the resulting algorithms possess detailed conservation properties at the local level as well. This is just a consequence of the local character of the Lagrangian, and therefore the discrete Lagrangians, for continuum mechanics. For more general Lagrangians this is of course not necessarily true.

In adopting the space–time perspective one is naturally led to consider algorithms based on multiresolution discretizations, *both* in space and time. We propose herein a class of powerful discretizations based on a decomposition of space, with finite elements for instance, and the freedom to choose the size of the time interval over each spatial domain, i.e., the time step at each point in space–time. The resulting variational algorithms are termed *asynchronous variational integrators* (AVI). In particular, when applied to dynamical systems defined by the finite element method, AVIs permit the selection of different time steps for each element. The local time steps need not bear an integral relation to each other, and the integration of the elements may, therefore, be carried out *asynchronously*.

The asynchronous algorithms developed within this thesis share many features with multi-time step integration algorithms, sometimes termed subcycling methods. These algorithms have been developed in Neal and Belytschko [1989] and Belytschko and Mullen [1976], mainly to allow stiff elements, or regions of the model, to advance at smaller time steps than the more compliant ones. In its original version, the method grouped the nodes of the mesh and assigned to each group a different time step. Adjacent groups of nodes were constrained to have integer time step ratios (see Belytschko and Mullen [1976]), a condition that was relaxed in Neal and Belytschko [1989] and Belytschko [1981]. Recently an implicit multi-time step integration method was developed and analyzed in Smolinski and Wu [1998]. We also mention the related work done by Hughes and Liu [1978] and Hughes et al. [1979]. The freedom to choose the time step for each element, subject to stability considerations, as well as the way nodes are updated, are the distinguishing features of the asynchronous algorithms introduced here.

The use of multi-time step methods in structural dynamics is clearly advantageous for elaborate geometries, where the minimum geometric feature could be much smaller than the overall dimensions of the structure. While with synchronous algorithms there is probably no other choice than approximating the geometry to remove the small scale features, with AVIs no such thing is necessary. Likewise, it is known that the construction of three–dimensional tetrahedral meshes often suffers from the presence of very flat or bad aspect ratio elements, termed *slivers*, which similarly to small geometric features, drive the time step for synchronous explicit algorithms down severely.

AVIs sidestep these difficulties by allowing each element or region of space to advance at their own intrinsic pace. There are, in addition, several other application areas that badly need AVI-like algorithms, most notably with the fast development of complex multiscale material models. In this context, the core of the computational cost for finite element simulations has shifted from assembling forces and computing displacements to the elemental computations, which usually involve the use of elaborate material constitutive models. In addition to the thermoelastic problem, other physical processes are often considered as well, such as plastic deformation, chemical reactions and phase transitions. Highly spatially localized timescales can be induced by any or all of these processes. For instance, the propagation of a detonation wave in a thermoelastic material induces the usually faster timescale of the chemical reaction in the region surrounding the detonation front. Not only do we need spatially resolved meshes to accurately capture the detonation front, but the use of AVIs becomes essential if any meaningful time is to be reached by the simulation. We note additionally that despite the growing computational power provided by highly parallel machines, solutions are still obtained by advancing forward in time, which makes AVIs even more fundamental for large-scale simulations in the near future.

There are also many connections between the multi-time step impulse method (also known as Verlet-I and r-RESPA), which is popular in molecular dynamics applications, and the AVI algorithm here (see Grubmüller et al. [1991] and Tuckerman et al. [1992]). Thus, when applied to a system of ODEs the AVI method may be regarded as a fully asynchronous generalization of the impulse method.

Chapter 3 fully develops the theory and implementation of AVIs for continuum mechanics problems. It introduces a particular class of space–time discretization and defines the discrete Lagrangians. It then analyzes the momentum conservation properties, and provides the expressions for the preserved discrete linear and angular momentum. Notice that once the action sum has been postulated, all of the relevant discrete mechanical quantities emanate uniquely from the theory, even in cases where otherwise only expert guessing or "luck" would be required. Several numerical examples for hyperelastic and thermoelastic materials are presented to illustrate the versatility and robustness of the new concepts. In particular, we use AVIs to simulate the propagation of a high-explosive detonation wave within a solid canister. To numerically capture the shock preceding the detonation wave we briefly present an artificial viscosity scheme developed in Lew et al. [2001], as well as the extension of AVIs to dissipative systems.

In addition to conservation of linear and angular momentum, stemming from rigid body translation and rotation invariance of the Lagrangian, it is customary to have other quantities conserved as well, such as energy and the J, L and M path integrals in solid mechanics. These quantities can also be derived from Noether's theorem, provided the right symmetries are considered. In Chapter 4 an elegant space–time formulation of Lagrangian mechanics is presented, which includes temporal,

material and spatial variations and symmetries as special cases. Even though similar formulations have been known for some time, we felt it deserved to be included to make the parallel between the continuous and discrete theories of Mechanics complete and transparent. This formulation unites energy, configurational forces and the Euler–Lagrange equations within a single picture, and naturally delivers the aforementioned conservation laws.

In particular, energy conservation can be regarded both as one of the Euler–Lagrange equations stemming from the space–time formulation, as well as the conservation law associated with invariance under time translations. Correspondingly, in the discrete picture we consider the AVI's time steps as part of the dynamical variables, and obtain the associated discrete Euler–Lagrange equations. These equations can be recognized as local energy balance equations, and are expected to be satisfied by choosing the value of the time step at each point in space–time. In this case, a discrete version of Noether's theorem guarantees the *exact* conservation of energy both locally and globally. Perhaps the greatest difference with the continuum case is that the DEL equations expressing the local linear momentum balance do not imply the DEL equation expressing the local energy balance. As we shall have the opportunity to see in Chapter 4, there are good reasons for this and it has very important consequences.

Unfortunately, the local energy balance equation generally involves the unknown time step in a highly nonlinear way. Very often it is not possible to find a suitable time step that satisfies this equation. Nevertheless, as the numerous examples in Chapter 4 show, even without deliberately adjusting the time step to achieve exact conservation these algorithms possess remarkable local and global energy conservation properties, which probably originate from their symplectic and variational nature.

One of the most pleasing aspects of the space–time picture of Lagrangian mechanics is that it contains elastostatics as a particular case, in which the action becomes the potential energy of the system and Hamilton's principle translates into seeking the minimum energy configuration. Configurational forces (see, e.g., Gurtin [2000]), the driving forces behind phase transformations and crack propagation for instance, are obtained from the space–time formulation on an equal footing with energy, in as much as time and spatial coordinates are regarded on an equal footing. The static J and L path independent integrals, widely used in fracture mechanics and to compute forces over inclusions and defects, are the conserved quantities related to configurational forces. They stem from the invariance of the elastic energy of a homogeneous material under rigid translations and rotations in the reference configuration.

The similarities between configurational forces and energy go even farther. The equilibrium of configurational forces is also obtained as one of the Euler–Lagrange equations of the space–time formulation, and it is identically satisfied whenever the local linear momentum balance is. Nevertheless, in the discrete setting the balance of configurational forces has to be requested separately,

and it reduces to a set of equations where the parameters defining the spatial discretization, i.e., the positions of the nodes, have to be solved for. The resulting mesh adaption methodology is termed *variational arbitrary Lagrangian–Eulerian* (VALE) method, and it was initially developed and proposed in Thoutireddy and Ortiz [2003]. In Chapter 4 the discrete path independent J and L integrals are defined and shown to be preserved over any closed surface in the mesh.

The analog to symplecticity in the continuum mechanics setting is termed multisymplecticity, and it is briefly discussed in Chapter 4. In some cases, multisymplecticity reduces to well known and easy to understand principles, including the Betti reciprocity principle and other well known reciprocity principles in mechanics.

The theory is by no means concluded. There are numerous applications still to be developed, such as to the evolution of microstructure, to electrodynamics, to fluid mechanics and to numerical relativity, where more complex symmetries are involved. Similarly to continuum mechanics, the clear understanding of the continuous systems is used to guide the development of discrete analogues of the geometric structure. This is one of the most appealing and distinguishing aspects of this methodology, and truly makes pursuing this task a worthy one.

Chapter 2

Variational time integrators for ODE

In this chapter we review the fundamental facts about variational integrators and Discrete Mechanics. The chapter summarizes the main results of the theory in very simple and easy to understand terms, while we add a few more. The original contributions in this chapter include the formulation of two–point constraints and the discussions in sections 2.8 and 2.9. For a thorough and comprehensive description of the theory we refer the reader to Marsden and West [2001].

For the sake of readability, we confine ourselves in this thesis to work in coordinates. We do include, however, geometrical asides in order to hint at the more general manifold picture. These short but explanatory paragraphs have been included in Lew et al. [2003b], and they have been mainly written by Matt West while collaborating in the aforementioned manuscript.

2.1 The basic idea

A bumper sticker explaining how to construct variational integrators would read

"*Approximate the action instead of directly approximating the equations of motion.*"

This simple idea turns out to be very powerful, as we shall have the opportunity to explore in this thesis. In fact, it has underpinned the solutions to elastostatics problems with the finite element method for fifty years now. To explain the implications of the above bumper sticker, in the following we briefly review the Lagrangian formulation of the mechanics of a conservative system, and then we mimic this process at the discrete level to construct variational integrators.

Continuous time Lagrangian mechanics We consider a conservative mechanical system with a Lagrangian $L(q, \dot{q})$, where $q = (q^1, q^2, \ldots, q^n)$ is a point in the configuration space Q. In Lagrangian mechanics the trajectories of the system are obtained from Hamilton's principle, namely, we seek

curves $q(t)$ for which the action functional

$$S[q(t)] = \int_a^b L(q, \dot{q}) dt \tag{2.1}$$

is stationary when compared with other curves with the same endpoints at times a and b. In other words, $q(t)$ should satisfy

$$\delta S = \int_a^b \left[\frac{d}{dt} \frac{\partial L}{\partial \dot{q}} - \frac{\partial L}{\partial q} \right] \cdot \delta q \, dt + \frac{\partial L}{\partial \dot{q}} \cdot \delta q \Big|_a^b = 0, \tag{2.2}$$

for all variations δq such that $\delta q(a) = \delta q(b) = 0$. The corresponding Euler–Lagrange equations are

$$\frac{d}{dt} \frac{\partial L}{\partial \dot{q}} - \frac{\partial L}{\partial \dot{q}} = 0. \tag{2.3}$$

For completeness, we recall the definition of a variation of a curve $q(t)$ as given in Marsden and Ratiu [1994]. Consider a one–parameter family of curves $q^\varepsilon(t)$ in Q such that $q^0(t) = q(t)$. Associated to $q^\varepsilon(t)$ we define a *variation* $\delta q(t)$ as

$$\delta q(t) = \frac{\partial q^\varepsilon(t)}{\partial \varepsilon} \Big|_{\varepsilon=0}.$$

Discrete time Lagrangian mechanics. A variational integrator for a conservative mechanical system is constructed by approximating the action integral (2.1) with an *action sum*

$$S_d = \sum_{k=0}^{N-1} L_d(q_k, q_{k+1}, t_k, t_{k+1}), \tag{2.4}$$

where L_d is the *discrete Lagrangian* and (q_k, t_k), $k = 0, \ldots, N$, are the points and times defining the discrete trajectory. The discrete Lagrangian is constructed as a good approximation to the action functional for the exact trajectory $q(t)$, i.e.,

$$L_d(q(t_k), q(t_{k+1}), t_k, t_{k+1}) \approx \int_{t_k}^{t_{k+1}} L(q, \dot{q}) \, dt. \tag{2.5}$$

Note that we have taken the discrete Lagrangian to be a function of two points in Q and two times. We shall see examples of more general dependence later in the thesis, especially in the formulation of higher-order integrators[1] and asynchronous methods.

The discrete trajectory follows after applying the *discrete variational principle*, namely, we seek points $\{q_k\}_{k=0,\ldots,N}$ such that the discrete action sum is stationary under all admissible variations

[1] It is possible, however, to recast an n-point discrete Lagrangian into a 2-point one, see Marsden and West [2001]

that keep the end points q_0, q_N fixed. The variations of the S_d follow from

$$\delta S_d = D_1 L_d(q_0, q_1, t_0, t_1) \cdot \delta q_0 + D_2 L_d(q_{N-1}, q_N, t_{N-1}, t_N) \cdot \delta q_N + \sum_{k=1}^{N-1} [D_1 L_d(q_k, q_{k+1}, t_k, t_{k+1}) + D_2 L_d(q_{k-1}, q_k, t_{k-1}, t_k)] \cdot \delta q_k. \quad (2.6)$$

We obtain in this way the *discrete Euler–Lagrange* equations

$$D_1 L_d(q_k, q_{k+1}, t_k, t_{k+1}) + D_2 L_d(q_{k-1}, q_k, t_{k-1}, t_k) = 0, \quad (2.7)$$

where we henceforth denote with $D_i L_d$ the slot derivative with respect to the i-th argument in L_d. Assuming that the sequence of time steps is set *a priori*, equation (2.7) implicitly defines a mapping $(q_{k-1}, q_k) \to (q_k, q_{k+1})$, the algorithm to advance the solution in time given initial conditions (q_0, q_1).

The geometric picture. The connection between the continuous and discrete variational principles is graphically represented in Figure 2.1. This geometric interpretation becomes of utmost importance when analyzing symmetries and conservation laws of the continuous and discrete variational principles, as we shall see later. A thorough description of the underlying geometry for variational integrators is provided in Marsden and West [2001].

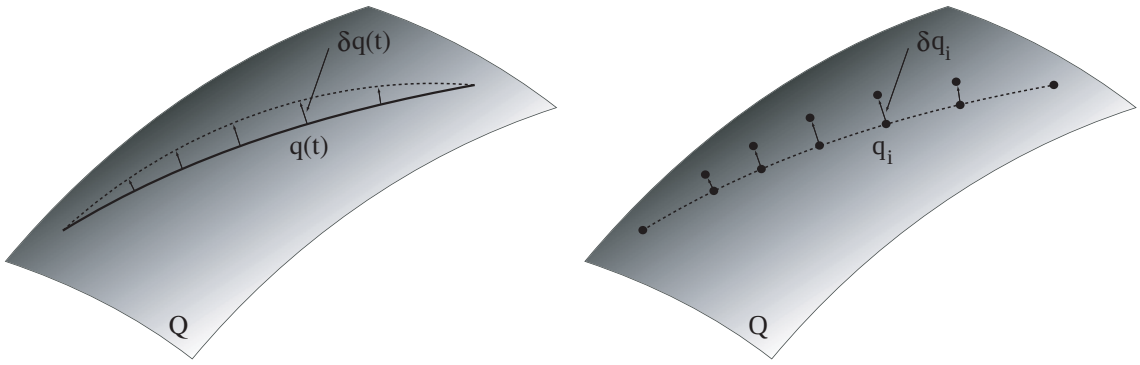

(a) Continuous variational principle

(b) Discrete variational principle

Figure 2.1: For the continuous variational principle we compare curves in the configuration space Q, while for the discrete variational principle the comparison is between neighboring points in Q. In both cases, the variations δq are tangent to Q.

Order of accuracy. As mentioned previously, we request the discrete Lagrangian to be a good approximation to the action functional for the exact solution of the problem. In Marsden and West [2001] this statement is made precise and we reproduce it here. A discrete Lagrangian is of *order r*

if

$$L_d(q_0, q_1, t_0, t_1) = \int_{t_0}^{t_1} L(q(t), \dot{q}(t))dt + \mathcal{O}(t_1 - t_0)^{r+1}, \tag{2.8}$$

where $q(t)$ is the unique solution of the Euler–Lagrange equations for L with $q(t_0) = q_0$ and $q(t_1) = q_1$. It can then be proven [Marsden and West, 2001, Theorem 2.3.1] that if L_d is of order r then the corresponding variational integrator is also of order r, so that

$$q_k = q(t_k) + \mathcal{O}(\Delta t)^{r+1}.$$

To design high order variational integrators we must therefore construct discrete Lagrangians which accurately approximate the action integral.

2.1.1 Examples of discrete Lagrangians.

We show now some examples of discrete Lagrangians generating well–known numerical schemes for classical mechanical systems, i.e., Lagrangians of the type $L(q, \dot{q}) = \frac{1}{2} q^{\mathsf{T}} M q - V(q)$, where M is a positive definite symmetric matrix and $V : Q \to \mathbb{R}$ is the potential energy of the system. For a more complete description of these and other examples, see Marsden and West [2001] or Lew et al. [2003b].

Generalized midpoint rule. The discrete Lagrangian for the generalized midpoint rule is

$$\begin{aligned} L_d^{\mathrm{mp},\alpha}(q_0, q_1, t_0, t_1) &= (t_1 - t_0) L\left((1-\alpha)q_0 + \alpha q_1, \frac{q_1 - q_0}{t_1 - t_0}\right) \\ &= \frac{t_1 - t_0}{2} \left(\frac{q_1 - q_0}{t_1 - t_0}\right)^{\mathsf{T}} M \left(\frac{q_1 - q_0}{t_1 - t_0}\right) - (t_1 - t_0) V\Big((1-\alpha)q_0 + \alpha q_1\Big), \end{aligned} \tag{2.9}$$

where $\alpha \in [0, 1]$. The discrete Euler–Lagrange equations (2.7) are thus

$$\begin{aligned} &M\left(\frac{q_{k+1} - q_k}{t_{k+1} - t_k} - \frac{q_k - q_{k-1}}{t_k - t_{k-1}}\right) \\ &= -(t_{k+1} - t_k)(1-\alpha)\nabla V\Big((1-\alpha)q_k + \alpha q_{k+1}\Big) - (t_k - t_{k-1})\alpha \nabla V\Big((1-\alpha)q_{k-1} + \alpha q_k\Big). \end{aligned} \tag{2.10}$$

Note that for constant time step, i.e., $t_k - t_{k-1} = const.$, and $\alpha = 0$ we recover the second-order Newmark explicit scheme.

Generalized trapezoidal rule. The discrete Lagrangian that generates the generalized trapezoidal rule is

$$L_d^{\mathrm{tr},\alpha}(q_0,q_1,t_0,t_1) = (t_1-t_0)(1-\alpha)L\left(q_0,\frac{q_1-q_0}{t_1-t_0}\right) + (t_1-t_0)\alpha L\left(q_1,\frac{q_1-q_0}{t_1-t_0}\right) \tag{2.11}$$
$$= \frac{t_1-t_0}{2}\left(\frac{q_1-q_0}{t_1-t_0}\right)^{\mathsf{T}} M\left(\frac{q_1-q_0}{t_1-t_0}\right) - (t_1-t_0)\Big((1-\alpha)V(q_0)+\alpha V(q_1)\Big),$$

where $\alpha \in [0,1]$. The corresponding discrete Euler–Lagrange equations are

$$M\left(\frac{q_{k+1}-q_k}{t_{k+1}-t_k} - \frac{q_k-q_{k-1}}{t_k-t_{k-1}}\right) = -\left[(t_{k+1}-t_k)(1-\alpha)+(t_k-t_{k-1})\alpha\right]\nabla V(q_k). \tag{2.12}$$

This method is explicit for all α.

Time finite elements (Galerkin) methods. Both the generalized midpoint and generalized trapezoidal discrete Lagrangians discussed above can be viewed as particular cases of using finite elements to compute the action integral. In general, for each time interval $[t_0,t_1]$ we can construct a discrete Lagrangian by choosing a set of basis functions $N_a(\tau)$, $a=0,\ldots,s$, and a quadrature rule (τ_i,w_i), $i=1,\ldots,Q$. Here τ_i and w_i are the times and weights of the quadrature rule, respectively. The discrete Lagrangian is then given by

$$L_d^{G,s,\mathrm{full}}(q_0,\ldots,q_s,t_0,t_1) = (t_1-t_0)\sum_{i=1}^{Q} w_i L\left(\sum_{a=0}^{s} q_a N_a(\tau_i), \sum_{a=0}^{s} q_a \frac{dN_a}{d\tau}(\tau_i)\right). \tag{2.13}$$

This is an $(s+1)$-point discrete Lagrangian. We can recast it into a 2-point discrete Lagrangian whenever q_0 and q_s are the only shared degrees of freedom between elements, i.e., only N_0 and N_s are nonzero at t_0 and t_1. The 2-point discrete Lagrangian is

$$L_d^{G,s}(q_0,q_s,t_0,t_1) = \operatorname*{ext}_{q_1,\ldots,q_{s-1}} L_d^{G,s,\mathrm{full}}(q_0,\ldots,q_s,t_0,t_1), \tag{2.14}$$

where $\operatorname{ext}_{q_1,\ldots,q_{s-1}} L_d^{G,s,\mathrm{full}}$ means that $L_d^{G,s,\mathrm{full}}$ should be evaluated at the critical values of $q_1,\ldots,q_{s-1}$. Note that this is equivalent to requesting these degrees of freedom to satisfy their corresponding discrete Euler–Lagrange equations.

Of course one can also work directly with the discrete Lagrangian (2.13) whenever (2.14) cannot be obtained. This happens, for example, when trying to obtain continuous velocities across time intervals.

The use of time finite elements to derive integration algorithms was proposed and analyzed by several authors, see for instance Fried [1969], Argyris and Scarpf [1969] or Bottasso [1997]. The discrete mechanics framework sheds a new perspective on these algorithms, exposing not only the

remarkable conservation properties, but providing also convergence analysis through new powerful mathematical tools, such as Γ-convergence (see Müller and Ortiz [2003]), and because of the nice geometric properties of the integrators, backward error analysis (Hairer and Lubich [1997]; Reich [1999]; Hairer et al. [2002]).

2.2 Conservation properties

We now review the derivation of Noether's theorem both in the discrete and continuous cases.

2.2.1 Noether's theorem and momentum conservation

One of the important features of variational systems is that symmetries of the system lead to momentum conservation laws of the Euler–Lagrange equations, a classical result known as Noether's theorem.

Consider a one–parameter group of curves $q^\varepsilon(t)$, with $q^0(t) = q(t)$, which have the property that $L(q^\varepsilon(t), \dot{q}^\varepsilon(t)) = L(q(t), \dot{q}(t))$ for all ε. When the Lagrangian is invariant in this manner then we have a symmetry of the system, and we write

$$\xi(t) = \left.\frac{\partial q^\varepsilon(t)}{\partial \varepsilon}\right|_{\varepsilon=0} \tag{2.15}$$

for the infinitesimal symmetry direction.

The fact that the Lagrangian is invariant means that the action integral is also invariant, therefore its derivative with respect to ε is zero. If $q(t)$ is a solution trajectory then we can set the Euler–Lagrange term in equation (2.2) to zero to obtain

$$0 = \left.\frac{\partial}{\partial \varepsilon}\right|_{\varepsilon=0} \int_0^T L\big(q(t), \dot{q}(t)\big)\, dt = \frac{\partial L}{\partial \dot{q}}\big(q(T), \dot{q}(T)\big) \cdot \xi(T) - \frac{\partial L}{\partial \dot{q}}\big(q(0), \dot{q}(0)\big) \cdot \xi(0). \tag{2.16}$$

The terms on the right–hand side above are the final and initial momentum in the direction ξ, which are thus equal. This is the statement of *Noether's theorem*.

As examples, consider the one–parameter groups $q^\varepsilon(t) = q(t) + \varepsilon v$ and $q^\varepsilon(t) = \exp(\varepsilon\Omega)q(t)$ for any vector v and skew–symmetric matrix Ω. The transformations give translations and rotations, respectively, and evaluating (2.16) for these cases gives conservation of linear and angular momentum, assuming that the Lagrangian is indeed invariant under these transformations.

Geometric aside. More generally, we may consider an arbitrary Lie group G, with Lie algebra $\mathfrak{g}$, rather than the one–dimensional groups taken above. The analogue of $\xi(t)$ is then the infinitesimal generator $\xi_Q : Q \to TQ$, for any $\xi \in \mathfrak{g}$, corresponding to an action of G on Q whose lift to TQ leaves L invariant. Equation (2.16) then becomes $(\partial L/\partial \dot{q}) \cdot \xi_Q|_0^T = 0$, which means that the momentum

map $J_L : TQ \to \mathfrak{g}^*$ is conserved, where $J_L(q,\dot{q}) \cdot \xi = (\partial L/\partial \dot{q}) \cdot \xi_Q(q)$. While we must generally take many one–parameter groups, such as translations by any vector v, to show that a quantity such as linear momentum is conserved, with this general framework we can take $\mathfrak{g}$ to be the space of all vs, and thus obtain conservation of linear momentum with only a single group, albeit multidimensional.

2.2.2 Discrete time Noether's theorem and discrete momenta

A particularly nice feature of the variational derivation of momentum conservation is that we simultaneously derive both the expression for the conserved quantity and the theorem that it is conserved. By using the variational derivation in the discrete time case, we can thus obtain the definition of discrete time momenta, as well as a discrete time Noether's theorem implying that they are conserved.

Take a one–parameter group of discrete time curves $\{q_k^\varepsilon\}_{k=0}^N$ such that $L_d(q_k^\varepsilon, q_{k+1}^\varepsilon, t_k, t_{k+1}) = L_d(q_k, q_{k+1}, t_k, t_{k+1})$ for all ε and k, with $q_k^0 = q_k$. The infinitesimal symmetry for such an invariant discrete Lagrangian is written

$$\xi_k = \left.\frac{\partial q_k^\varepsilon}{\partial \varepsilon}\right|_{\varepsilon=0}. \tag{2.17}$$

Invariance of the discrete Lagrangian implies invariance of the action sum, and therefore its ε derivative is zero. Assuming that $\{q_k\}$ is a solution trajectory, then (2.6) becomes

$$0 = \left.\frac{\partial}{\partial \varepsilon}\right|_{\varepsilon=0} \sum_{k=0}^{N-1} L_d(q_k^\varepsilon, q_{k+1}^\varepsilon, t_k, t_{k+1}) = D_1 L_d(q_0, q_1, t_0, t_1) \cdot \xi_0 + D_2 L_d(q_{N-1}, q_N, t_{N-1}, t_N) \cdot \xi_N. \tag{2.18}$$

We thus have the *discrete Noether's theorem*

$$-D_1 L_d(q_0, q_1, t_0, t_1) \cdot \xi_0 = D_2 L_d(q_{N-1}, q_N, t_{N-1}, t_N) \cdot \xi_N. \tag{2.19}$$

An alternative statement of (2.19) is obtained by noticing that $0 = D_1 L_d(q_0, q_1, t_0, t_1) \cdot \xi_0 + D_2 L_d(q_0, q_1, t_0, t_1) \cdot \xi_1$, as L_d is invariant. By replacing in (2.19) we obtain

$$D_2 L_d(q_{N-1}, q_N, t_{N-1}, t_N) \cdot \xi_N = D_2 L_d(q_0, q_1, t_0, t_1) \cdot \xi_1, \tag{2.20}$$

which gives a precise definition of the discrete momentum $D_2 L_d(q_k, q_{k+1}, t_k, t_{k+1}) \cdot \xi_{k+1}$ in the direction of the symmetry $(\xi_0, \ldots, \xi_N)$.

More generally, the discrete Noether's theorem is valid between any two discrete times $t_k < t_{k+n}$. It follows, for instance, after considering the discrete action sum obtained by adding the n discrete Lagrangians between t_k and t_{k+n} only.

Consider the example discrete Lagrangian (2.9) with $\alpha = 0$, and assume that $q \in Q \equiv \mathbb{R}^3$ and that V is a function of the norm of q only. This is the case of a particle in a radial potential

for example. Then the discrete Lagrangian is invariant under rotations $q_k^\varepsilon = \exp(\varepsilon\Omega)q_k$, for any skew–symmetric matrix $\Omega \in \mathbb{R}^{3\times 3}$. Evaluating (2.19) in this case gives

$$q_N \times M\left(\frac{q_N - q_{N-1}}{t_N - t_{N-1}}\right) = q_1 \times M\left(\frac{q_1 - q_0}{t_1 - t_0}\right). \tag{2.21}$$

We have thus computed the correct expressions for the discrete angular momentum, and shown that it is conserved. Note that while this expression may seem obvious, in more complicated examples this will not be the case.

Geometric aside. As in the continuous case, we can extend the above derivation to multidimensional groups and define a fully discrete momentum map $J_{L_d} : Q \times Q \to \mathfrak{g}^*$ by $J_L(q_0, q_1) \cdot \xi = D_2L_d(q_0, q_1) \cdot \xi_Q(q_1)$, for all $\xi \in \mathfrak{g}$. In fact there are two discrete momentum maps, corresponding to D_1L_d and D_2L_d, but they are equal whenever L_d is invariant.

2.3 Forcing and dissipation

The extension of variational integrators to systems with forcing and dissipation was first proposed in Kane et al. [2000]. We briefly review their derivation here.

For continuous mechanical systems with forcing and dissipation, the equations of motion can be obtained from the Lagrange-D'alembert variational principle. We seek trajectories $q(t)$ such that

$$\delta \int_a^b L(q(t), \dot{q}(t))\, dt + \int_a^b F(q(t), \dot{q}(t)) \cdot \delta q\, dt = 0 \tag{2.22}$$

for all variations $\delta q(t)$ that satisfy $\delta q(a) = \delta q(b) = 0$, where $F(q, \dot{q})$ is an arbitrary forcing function. The discrete trajectory is obtained by analogy through the *discrete Lagrange-D'alembert* variational principle

$$\delta S_d + \sum_{k=0}^{N-1} \left[F_d^-(q_k, q_{k+1}, t_k, t_{k+1}) \cdot \delta q_k + F_d^+(q_k, q_{k+1}, t_k, t_{k+1}) \cdot \delta q_{k+1}\right] = 0, \tag{2.23}$$

where F_d^- and F_d^+ are called the left and right discrete forces, respectively. These forces should satisfy

$$F_d^-(q_k, q_{k+1}, t_k, t_{k+1}) \cdot \delta q_k + F_d^+(q_k, q_{k+1}, t_k, t_{k+1}) \cdot \delta q_{k+1} \approx \int_{t_k}^{t_{k+1}} F(q(t), \dot{q}(t)) \cdot \delta q\, dt. \tag{2.24}$$

Notice that when using time-finite-elements to discretize the trajectory we naturally obtain expressions for F_d^- and F_d^+ from equation (2.24). The discrete Lagrange-D'alembert principle is equivalent to the discrete variational principle when $F_d^\pm$ are zero. Consequently, the discretization of the con-

servative part of the mechanical system still preserves all properties of variational integrators. This is clearly advantageous for weakly dissipative systems, since the integrators obtained through the discrete Lagrange-D'alembert principle capture the dissipation rate very accurately, see Kane et al. [2000], Lew et al. [2003b] for numerical examples.

Non-autonomous Lagrangians. The construction of variational integrators for mechanical systems with non-autonomous Lagrangians, i.e., $L(q, \dot{q}, t)$, is also accomplished by using the discrete variational principle (see, e.g.,Marsden and West [2001]). In this case the discrete Lagrangian will typically present an explicit dependence on t_k or t_{k+1}, instead of on $(t_{k+1} - t_k)$ only.

2.4 Constraints

The variational framework provides a natural way to impose holonomic constraints through Lagrange multipliers. In this context we seek trajectories $q(t)$ of the mechanical system satisfying $g(q(t)) = 0$ for all t, where g is a function taking values in Q. The simplest and geometrically meaningful discrete approach is to satisfy the constraint at every point q_k of the discrete trajectory. We extend therefore the discrete action sum to account for the pointwise constraints

$$S_d = \sum_{k=0}^{N-1} \left[L_d(q_k, q_{k+1}, t_k, t_{k+1}) + \lambda_{k+1} \cdot g(q_{k+1}) \right]. \tag{2.25}$$

After applying the discrete variational principle with both $\{q_k\}$ and $\{\lambda_k\}$ as dynamical variables, we obtain the *constrained discrete Euler–Lagrange* equations

$$D_2 L_d(q_{k-1}, q_k, t_{k-1}, t_k) + D_1 L_d(q_k, q_{k+1}, t_k, t_{k+1}) = -\lambda_k \cdot \nabla g(q_k) \tag{2.26a}$$

$$g(q_{k+1}) = 0, \tag{2.26b}$$

which can be solved for λ_k and q_{k+1}, given (q_{k-1}, q_k).

Two–point constraints. Occasionally, we may find it convenient to impose the constraints not at the discrete points of the discrete trajectory, but at some intermediate states. A typical example appears when using the generalized midpoint rule (2.9) with $\alpha = 1/2$ in problems involving incompressible materials. In these cases, it is often convenient to enforce the incompressibility constraint in the same configuration used to evaluate the internal forces, given by $(q_k + q_{k+1})/2$.

Let $f : Q \times Q \to Q$ be the function returning the intermediate state $f(q_k, q_{k+1})$. The discrete

action sum is now extended as

$$S_d = \sum_{k=0}^{N-1} \left[L_d(q_k, q_{k+1}, t_k, t_{k+1}) + \lambda_{k+1} \cdot g[f(q_k, q_{k+1})] \right], \tag{2.27}$$

and the constrained discrete Euler–Lagrange equations are given by

$$\begin{aligned} D_2 L_d(q_{k-1}, q_k, t_{k-1}, t_k) + D_1 L_d(q_k, q_{k+1}, t_k, t_{k+1}) = & \qquad (2.28a) \\ -\lambda_{k+1} \cdot \nabla g[f(q_k, q_{k+1})] \cdot D_1 f(q_k, q_{k+1}) & \\ -\lambda_k \cdot \nabla g[f(q_{k-1}, q_k)] \cdot D_2 f(q_{k-1}, q_k) & \\ g[f(q_k, q_{k+1})] = 0. & \qquad (2.28b) \end{aligned}$$

Equations (2.28) should be solved for λ_{k+1} and q_{k+1}, given λ_k and (q_k, q_{k-1}). However, we note that a starting procedure for λ_1 is needed, since it cannot be determined from equations (2.28). This is a pathology of the above formulation. One possible and natural starting procedure is

$$-p_0 + D_1 L_d(q_0, q_1, t_0, t_1) = -\lambda_1 \cdot \nabla g[f(q_0, q_1)] \cdot D_1 f(q_0, q_1) \tag{2.29a}$$

$$g[f(q_0, q_1)] = 0, \tag{2.29b}$$

where q_0 and p_0 are the given initial position and linear momentum, and we solve for q_1 and λ_1. This starting procedure returns a value for λ_1, computed by simultaneously imposing the correct constraint for the intermediate state $f(q_0, q_1)$.

2.5 Symplecticity

In addition to the conservation of energy and momenta, Lagrangian mechanical systems also conserve another quantity known as a symplectic bilinear form. Although not very well known in the engineering community, the symplectic bilinear form is occasionally considered as fundamental as the Hamiltonian or the Lagrangian by the geometric mechanics community. It is the purpose of this section to define the symplectic form and show its conservation, both in the continuous and discrete cases, in very elementary terms. For a rigorous treatment of the subject the reader is referred to Marsden and Ratiu [1994].

Symplectic form. A *symplectic* form Ω in a finite–dimensional vector space Z is an invertible skew–symmetric bilinear form on Z. The pair (Z, Ω) is called a *symplectic vector space*.

More generally, we consider Ω itself to be a smooth function of $z \in Z$, and we indicate it Ω_z. Given two vectors $z_1, z_2 \in Z$, $\Omega_z(z_1, z_2)$ is the value of the skew–symmetric bilinear form at z when

contracted with the vectors z_1 and z_2[2]

Symplectic map. If (Z, Ω) and (Y, Ξ) are symplectic vector spaces, a smooth map $f : Z \to Y$ is called symplectic if it preserves the symplectic forms, that is, if

$$\Xi_{f(z)}(\nabla f(z) \cdot z_1, \nabla f(z) \cdot z_2) = \Omega_z(z_1, z_2) \tag{2.30}$$

for all z, z_1, $z_2 \in Z$. Note that $\nabla f \cdot z$ is the push-forward of z by the map f.

Continuous time symplecticity. Under appropriate smoothness assumptions, the solution $q(t)$ of the Euler–Lagrange equations (2.3) depends continuously on the time t and the initial conditions $(q_0, \dot{q}_0)$. For simplicity, we will assume that the configuration space Q is a subset of $\mathbb{R}^d$. The map $F_t : Q \times \mathbb{R}^d \to Q \times \mathbb{R}^d$ such that $F_t(q_0, \dot{q}_0) = (q(t), \dot{q}(t))$ is called the *flow of the Euler–Lagrange equations*. A fundamental fact of Lagrangian mechanics is that the flow F_t is a symplectic map for any time t for which the solution is well–defined.

To see this, consider a two–parameter set of initial conditions $(q_0^{\epsilon,\nu}, v_0^{\epsilon\nu})$ so that $(q^{\epsilon,\nu}(t), v^{\epsilon,\nu}(t)) = F_t(q_0^{\epsilon,\nu}, v_0^{\epsilon\nu})$ is the resulting trajectory of the system. The corresponding variations are denoted

$$\delta q_1^\epsilon(t) = \frac{\partial}{\partial \nu} q^{\epsilon,\nu}(t)\bigg|_{\nu=0} \qquad \delta q_2^\nu(t) = \frac{\partial}{\partial \epsilon} q^{\epsilon,\nu}(t)\bigg|_{\epsilon=0} \qquad \delta^2 q(t) = \frac{\partial}{\partial \epsilon}\frac{\partial}{\partial \nu} q^{\epsilon,\nu}(t)\bigg|_{\epsilon,\nu=0},$$

and we write $\delta q_1(t) = \delta q_1^0(t)$, $\delta q_2(t) = \delta q_2^0(t)$ and $q^\epsilon(t) = q^{\epsilon,0}(t)$. We now compute the second derivative of the action integral to be

$$\begin{aligned}
\frac{\partial}{\partial \epsilon}\bigg|_{\epsilon=0}\frac{\partial}{\partial \nu}\bigg|_{\nu=0} S(q^{\epsilon,\nu}) &= \frac{\partial}{\partial \epsilon}\bigg|_{\epsilon=0} (DS(q^\epsilon)\cdot \delta q_1^\epsilon) \\
&= \frac{\partial}{\partial \epsilon}\bigg|_{\epsilon=0} \left(\frac{\partial L}{\partial v^i}\bigg|_{(q^\epsilon(T), v^\epsilon(T))} (\delta q_1^\varepsilon)^i(T) - \frac{\partial L}{\partial v^i}\bigg|_{(q_0^\epsilon, v_0^\epsilon)} (\delta q_1^\varepsilon)^i(0) \right) \\
&= \frac{\partial^2 L}{\partial q^j \partial v^i}\bigg|_{F_T} \delta q_1^i(T)\delta q_2^j(T) + \frac{\partial^2 L}{\partial v^j \partial v^i}\bigg|_{F_T} \delta q_1^i(T)\delta \dot{q}_2^j(T) + \frac{\partial L}{\partial v^i}\bigg|_{F_T} \delta^2 q^i(T) \\
&\quad - \frac{\partial^2 L}{\partial q^j \partial v^i}\bigg|_{F_0} \delta q_1^i(0)\delta q_2^j(0) - \frac{\partial^2 L}{\partial v^j \partial v^i}\bigg|_{F_0} \delta q_1^i(0)\delta \dot{q}_2^j(0) - \frac{\partial L}{\partial v^i}\bigg|_{F_0} \delta^2 q^i(0),
\end{aligned}$$

where we used equation (2.2) to obtain the second equality. We write F_t for $F_t(q_0^{0,0}, v_0^{0,0})$ when no argument for F_t is given. Here and subsequently, repeated indices in a product indicate sum over the index range, while Df indicates the derivative of the function f. If we reverse the order of differentiation with respect to ϵ and ν, then by symmetry of mixed partial derivatives we will obtain

[2]Here we are explicitly using the fact that a finite–dimensional vector space is isomorphic to its tangent and cotangent spaces.

an equivalent expression. Subtracting this from the above equation then gives

$$\frac{\partial^2 L}{\partial q^j \partial v^i}\bigg|_{F_T}\Big[\delta q_1^i(T)\delta q_2^j(T) - \delta q_2^i(T)\delta q_1^j(T)\Big] + \frac{\partial^2 L}{\partial v^j \partial v^i}\bigg|_{F_T}\Big[\delta q_1^i(T)\delta \dot{q}_2^j(T) - \delta q_2^i(T)\delta \dot{q}_1^j(T)\Big]$$
$$= \frac{\partial^2 L}{\partial q^j \partial v^i}\bigg|_{F_0}\Big[\delta q_1^i(0)\delta q_2^j(0) - \delta q_2^i(0)\delta q_1^j(0)\Big] + \frac{\partial^2 L}{\partial v^j \partial v^i}\bigg|_{F_0}\Big[\delta q_1^i(0)\delta \dot{q}_2^j(0) - \delta q_2^i(0)\delta \dot{q}_1^j(0)\Big]. \quad (2.31)$$

Each side of this expression is an antisymmetric bilinear form, Ω_{F_t}, evaluated on the variations $(\delta q_1, \delta \dot{q}_1)$ and $(\delta q_2, \delta \dot{q}_2)$. Also, a simple application of the chain rule verifies that the variations at time T are the push-forward of the variations at time 0 by F_T. Therefore, equation (2.31) shows that the flow of the Euler–Lagrange equations F_T is a symplectic map under Ω_{F_t}.

The conservation of the symplectic form has a number of important consequences. Examples of this include Liouville's theorem, which states that phase space volume is preserved by the time evolution of the system, and four–fold symmetry of the eigenvalues of linearizations of the system, so that if λ is an eigenvalue, so too are $-\lambda$, $\bar{\lambda}$ and $-\bar{\lambda}$. There are many other important examples, see Marsden and Ratiu [1994].

Geometric aside. The above derivation can be written using differential geometric notation as follows. The boundary terms in the action variation equation (2.2) are intrinsically given by $\Theta_L = (\mathbb{F}L)^*\Theta$, the pullback under the Legendre transform of the canonical one–form $\Theta = p_i dq^i$ on T^*Q. We thus have $dS = (F_t)^*\Theta_L - \Theta_L$ and so using $d^2 = 0$ (which is the intrinsic statement of symmetry of mixed partial derivatives) we obtain $0 = d^2S = (F_t)^*(d\Theta_L) - d\Theta_L$. The symplectic two–form above is thus $\Omega_L = -d\Theta_L$, and we recover the usual statement of symplecticity of the flow F_t for Lagrangian systems.

Discrete time symplecticity. As we have seen above, symplecticity of continuous time Lagrangian systems is a consequence of the variational structure. There is thus an analogous property for discrete Lagrangian systems. The symplectic map in the discrete picture is $F_d^k : Q \times Q \to Q \times Q$ such that $F_d^k(q_0, q_1) = (q_k, q_{k+1})$, with $k = 0, \ldots, N-1$. The map F_d^k is called the *flow of the discrete Euler–Lagrange equations.*

Consider a two–parameter set of initial conditions $(q_0^{\varepsilon,\nu}, q_1^{\varepsilon,\nu})$ and let $\{q_k^{\varepsilon,\nu}\}_{k=0}^N$ be the resulting discrete trajectory. We denote the corresponding variations by

$$\delta q_k^\varepsilon = \frac{\partial}{\partial \nu} q_k^{\varepsilon,\nu}\bigg|_{\nu=0} \qquad \delta \bar{q}_k^\nu = \frac{\partial}{\partial \varepsilon} q_k^{\varepsilon,\nu}\bigg|_{\varepsilon=0} \qquad \delta^2 q_k = \frac{\partial}{\partial \varepsilon}\frac{\partial}{\partial \nu} q_k^{\varepsilon,\nu}\bigg|_{\varepsilon,\nu=0},$$

and we write $\delta q_k = \delta q_k^0$, $\delta \bar{q}_k = \delta \bar{q}_k^0$, $q_k^\varepsilon = q^{\varepsilon,0}$ and $q_k = q_k^{0,0}$ for $k = 0, \ldots, N$. The second derivative

of the action sum is thus given by

$$\begin{aligned}
\frac{\partial}{\partial\varepsilon}\bigg|_{\varepsilon=0}\frac{\partial}{\partial\nu}\bigg|_{\nu=0}S_d(\{q_k^{\varepsilon,\nu}\}) &= \frac{\partial}{\partial\varepsilon}\bigg|_{\varepsilon=0}\Big(DS_d(\{q_k^{\varepsilon}\})\cdot\delta q^{\varepsilon}\Big)\\
&= \frac{\partial}{\partial\varepsilon}\bigg|_{\varepsilon=0}\Big(D_{1i}L_d(q_0^{\varepsilon},q_1^{\varepsilon})\,(\delta q_0^{\varepsilon})^i + D_{2i}L_d(q_{N-1}^{\varepsilon},q_N^{\varepsilon})\,(\delta q_N^{\varepsilon})^i\Big)\\
&= D_{1j}D_{1i}L_d(q_0,q_1)\delta q_0^i\delta\bar{q}_0^j + D_{2j}D_{1i}L_d(q_0,q_1)\delta q_0^i\delta\bar{q}_1^j\\
&\quad + D_{1j}D_{2i}L_d(q_{N-1},q_N)\delta q_N^i\delta\bar{q}_{N-1}^j + D_{2j}D_{2i}L_d(q_{N-1},q_N)\delta q_N^i\delta\bar{q}_N^j\\
&\quad + D_{1i}L_d(q_0,q_1)\,\delta^2q_0^i + D_{2i}L_d(q_{N-1},q_N)\,\delta^2q_N^i,
\end{aligned}\tag{2.32}$$

where to obtain the second equality in the last equation we have used (2.6) and the fact that we are considering sets of discrete trajectories, i.e., they satisfy the discrete Euler–Lagrange equations (2.7). In equation (2.32) we indicated with D_{ai} the slot derivative with respect to the i-th component of the a-th variable. By symmetry of mixed partial derivatives, reversing the order of differentiation above gives an equivalent expression. After subtracting one from the other and rearranging the resulting equation we obtain

$$D_{1j}D_{2i}L_d(q_{N-1},q_N)\left[\delta q_N^i\delta\bar{q}_{N-1}^j - \delta\bar{q}_N^i\delta q_{N-1}^j\right] = D_{2j}D_{1i}L_d(q_0,q_1)\left[\delta\bar{q}_0^i\delta q_1^j - \delta q_0^i\delta\bar{q}_1^j\right],\tag{2.33}$$

which by equality of mixed partial derivatives gives

$$D_{1j}D_{2i}L_d(q_{N-1},q_N)\left[\delta q_N^i\delta\bar{q}_{N-1}^j - \delta\bar{q}_N^i\delta q_{N-1}^j\right] = D_{1j}D_{2i}L_d(q_0,q_1)\left[\delta q_1^i\delta\bar{q}_0^j - \delta\bar{q}_1^i\delta q_0^j\right].\tag{2.34}$$

We can now see that each side of this equation is an antisymmetric bilinear form, which we call the *discrete symplectic form*, evaluated on the variations δq_k and $\delta\bar{q}_k$. The two sides give this expression at the first time step and the final time step, so we have that the discrete symplectic form is preserved by the time evolution of the discrete system. Equivalently, the flow of the discrete Euler–Lagrange equations is a symplectic map.

The symplectic nature of the algorithm has important consequences, such as good long term energy behavior. The ability of variational integrators to get statistical quantities right can also probably be traced to the fact that it is symplectic.

Geometric aside. Intrinsically we can identify two one–forms $\Theta^+_{L_d} = D_2L_d dq_1$ and $\Theta^-_{L_d} = D_1L_d dq_0$, so that $dS_d = (F^N_{L_d})^*\Theta^+_{L_d} + \Theta^-_{L_d}$. Using $d^2 = 0$ (symmetry of mixed partial derivatives) gives $0 = d^2S_d = (F^N_{L_d})^*(d\Theta^+_{L_d}) + d\Theta^-_{L_d}$ and so defining the discrete symplectic two–forms $\Omega^\pm_{L_d} = -d\Theta^\pm_{L_d}$ gives $(F^N_{L_d})^*\Omega^+_{L_d} = -\Omega^-_{L_d}$, which is the intrinsic form of (2.33). However, we observe that $0 = d^2L_d = d(\Theta^+_{L_d} + \Theta^-_{L_d}) = -\Omega^+_{L_d} - \Omega^-_{L_d}$ and hence $\Omega^+_{L_d} = -\Omega^-_{L_d}$. Combining this with our previous expression then gives $(F^N_{L_d})^*\Omega^+_{L_d} = \Omega^+_{L_d}$ as the intrinsic form of (2.34), discrete

symplecticity of the evolution.

Observe that using the discrete Legendre transforms we have $\Theta^{\pm}_{L_d} = (\mathbb{F}L^{\pm}_d)^*\Theta$, where $\Theta = p_i dq^i$ is the canonical one–form on T^*Q. The expression (2.34) thus shows that the map $\mathbb{F}L^+_d \circ F_{L_d} \circ (\mathbb{F}L^+_d)^{-1}$ preserves the canonical symplectic two–form Ω on T^*Q. Variational integrators are thus symplectic methods in the standard sense.

2.6 Convergence

The convergence of variational integrators can be proved, under smoothness assumptions, by using traditional methods such as Lax's equivalence theorem (see, e.g., Richtmyer and Morton [1967]), in a similar way to any integration algorithm.

In addition, one can also take advantage of the variational structure of the algorithm to prove convergence, as first done in the pioneering work by Müller and Ortiz [2003]. In there they proved the Γ-convergence (see, e.g., Dal Maso [1993]) of the sequence of discrete action functionals to the continuous action in the limit of vanishing time step. They obtained the weak-$*$ convergence of solutions in $W^{1,\infty}(\mathbb{R})$ and the uniform convergence in compact subsets. Most remarkably, they proved the convergence of the sequence of Fourier transforms of discrete trajectories as measures in the flat norm. This type of analysis could only be performed because of the variational structure of the theory.

Perhaps the most insightful analysis of the algorithms is obtained through *backward error analysis*. A simple outline of the procedure can be found in Lew et al. [2003b], while we refer to Hairer et al. [2002] or Reich [1999] for the details. The most remarkable result is that the discrete trajectories of a symplectic integrator exactly sample or are exponentially close to the trajectories of a nearby Hamiltonian system, which explains the near energy conservation properties variational integrators have.

In many problems, one is not just interested in the accuracy of individual trajectories; in fact, for complex dynamical processes integrated over intermediate to long timescales, accuracy of individual trajectories may not be an appropriate thing to require. Rather, the interests shifts to accurately capturing some statistical quantities, such as the average kinetic energy or temperature in a molecular dynamics simulation. For this type of task, variational integrators have proved to be remarkably superior. See Lew et al. [2003b] for a neat example and some additional references.

2.7 Implementation of variational integrators

The outlined framework lends itself to a standardized and very simple computational implementation. The key to this implementation is to note that one of the terms in the discrete Euler–Lagrange

equations is known from the previous time step, i.e.,

$$D_1 L_d(q_k, q_{k+1}, t_k, t_{k+1}) + \underbrace{D_2 L_d(q_{k-1}, q_k, t_{k-1}, t_k)}_{p_k, \text{ known at } t_k} = 0, \tag{2.35}$$

where p_k is the discrete momentum at time t_k. Notice that this definition of momentum is not arbitrary, but it stems from the corresponding conserved quantity obtained from the discrete Noether's theorem.

Given (q_k, p_k), we find (q_{k+1}, p_{k+1}) by solving the discrete Euler–Lagrange equations written in the so called position-momentum form

$$D_1 L_d(q_k, q_{k+1}, t_k, t_{k+1}) = p_k \tag{2.36a}$$

$$D_2 L_d(q_k, q_{k+1}, t_k, t_{k+1}) = -p_{k+1}. \tag{2.36b}$$

It is then possible to solve first for q_{k+1} from equation (2.36a), and then compute p_{k+1} from equation (2.36b). This implementation has the appealing feature of being always a one–step update $(q_k, p_k) \to (q_{k+1}, p_{k+1})$, even for higher-order discrete Lagrangians such as (2.14). The definition the momentum has to be properly modified in the presence of external forcing and dissipation, but the structure of the algorithm still remains the same.

In general, equation (2.36a) will involve the unknown q_{k+1} in a nonlinear way. Upon linearization the tangent matrix $D_2 D_1 L_d(q_k, q_{k+1}, t_k, t_{k+1})$ needs not be symmetric, unlike elliptic boundary value problems. This is a consequence of the fact that we are solving forward in time. Fortunately, for some widely used discrete Lagrangians the tangent matrix is symmetric.

Variational integrators with constraints. The implementation of variational integrators with constraints, as given by equations (2.28), necessitates some extra care, but it can still be regarded as an extension of the implementation described above. It is given by the following position-momentum form

$$g[f(q_k, q_{k+1})] = 0 \tag{2.37a}$$

$$D_1 L_d(q_k, q_{k+1}, t_k, t_{k+1}) + \lambda_{k+1} \cdot \nabla g[f(q_k, q_{k+1})] \cdot D_1 f(q_k, q_{k+1}) = \tilde{p}_k + \lambda_k \cdot \pi_k \tag{2.37b}$$

$$D_2 L_d(q_k, q_{k+1}, t_k, t_{k+1}) = -\tilde{p}_{k+1} \tag{2.37c}$$

$$\nabla g[f(q_k, q_{k+1})] \cdot D_2 f(q_k, q_{k+1}) = -\pi_{k+1}. \tag{2.37d}$$

In this case we are given $(q_k, \tilde{p}_k, \lambda_k, \pi_k)$ and we solve for q_{k+1} and λ_{k+1} using equations (2.37a)-(2.37b), and then compute $\tilde{p}_{k+1}$ and π_{k+1} from equations (2.37c)-(2.37d).

When $D_1 f(q_k, q_{k+1}) \equiv 0$ for all (q_k, q_{k+1}), we recover the one–point constraint case given by

equations (2.26)[3]. However, it is not longer possible to solve for λ_{k+1} from equation (2.37b). Instead, we obtain a degenerate case, in which we have to solve for λ_k in place of λ_{k+1}. To account for this case minor modifications to the solution procedure might be required[4]. Nevertheless, the system of equations (2.37) provides a unifying framework, well–suited for object oriented implementations. For instance, both the discrete Lagrangian as well as the constraint $g \circ f$ can be derived from the same class, since both are required to provide and store the same type of information.

As a final remark, we have used $\tilde{p}$ for $D_2 L_d$ to distinguish it from the conserved quantity obtained from the discrete Noether's theorem when the action sum is invariant under rigid translations, namely, $p_k = \tilde{p}_k + \lambda_k \cdot \pi_k$.

2.8 Is it possible to derive the algorithms from a minimum principle?

Algorithms based on minimum principles have proved to be very useful on numerous occasions (see, e.g., Radovitzky and Ortiz [1999] and Ortiz and Stainier [1999]). It is of interest therefore to explore the possibility of obtaining the same variational time integrators we have introduced so far from an incremental minimum principle. More precisely, let

$$r(q_{k+1}; \Psi_{k+1}) = D_1 L_d(q_k, q_{k+1}, t_k, t_{k+1}) + D_2 L_d(q_{k-1}, q_k, t_{k-1}, t_k)$$

be the residue of the discrete Euler–Lagrange equations describing the algorithm, where $\Psi_{k+1} \equiv (q_k, q_{k-1}, t_{k+1}, t_k, t_{k-1})$. The question is: Is there a function $I(q_{k+1}; \Psi_{k+1})$ such that $r(q_{k+1}; \Psi_{k+1}) = \partial I(q_{k+1}; \Psi_{k+1})/\partial q_{k+1}$?

The answer in the general case is *no*. Assume the opposite, then

$$\left.\frac{\partial^2 I}{\partial q^i_{k+1} \partial q^j_{k+1}}\right|_{(q_{k+1};\Psi_{k+1})} = \left.\frac{\partial r_i}{\partial q^j_{k+1}}\right|_{(q_{k+1};\Psi_{k+1})} = D_{2j} D_{1i} L_d(q_k, q_{k+1}, t_k, t_{k+1}).$$

However, $D_2 D_1 L_d$ does not need to be symmetric, which proves the statement. For those special cases in which $D_2 D_1 L_d$ is in fact symmetric, it is possible to find such a function I. In addition, if $D_2 D_1 L_d$ is positive definite we obtain an incremental minimum principle.

2.9 When is an integrator variational?

Given a one–step time-integration algorithm, we would like to know whether it is generated by the discrete Euler–Lagrange equations of some discrete Lagrangian. We provide a partial answer to this

[3]The case $D_2 f(q_k, q_{k+1}) \equiv 0$ for all (q_k, q_{k+1}) is equivalent to the one discussed in this paragraph.
[4]In particular, the linearization of the system of equations (2.37a)- (2.37b) is different in the two cases

question in the proposition that follows, and subsequently discuss some examples. We assume for this section that $t_k - t_{k-1} = \Delta t = const.$ for all k, and we will not indicate the dependence of L_d on the discrete times.

Proposition 2.9.1 *Consider a one–step time integration algorithm in $Q \subset \mathbb{R}^m$ that maps $(q_{k-1}, q_k) \to (q_k, q_{k+1})$ and is implicitly defined by the relation*

$$f(q_{k+1}, q_k, q_{k-1}) = 0, \tag{2.38}$$

where $f : Q \times Q \times Q \to \mathbb{R}^m$ is a smooth function. Then, there exists $L_d : Q \times Q \to \mathbb{R}$ such that

$$D_1 L_d(x, y) + D_2 L_d(z, x) = f(y, x, z) \tag{2.39}$$

for all $x, y, z \in Q$ if and only if

$$D_{1i} f_j(y, x, v) = D_{3j} f_i(w, y, x) \qquad i, j = 1, \ldots, m \tag{2.40a}$$

$$D_{2i} f_j(y_0, x, z_0) = D_{2j} f_i(y_0, x, z_0) \qquad i, j = 1, \ldots, m \tag{2.40b}$$

for all $x, y, v, w \in Q$ and for some $y_0, z_0 \in Q$, where i, j are coordinate indices in Q.

Proof. The proof follows from simple and elementary observations. First, we show that conditions (2.40) are necessary. Condition (2.40b) follows from differentiating equation (2.39) with respect to x on both sides, and using the equality of mixed partial derivatives. To prove the necessity of condition (2.40a), we differentiate equation (2.39) with respect to y and z to obtain

$$D_{2j} D_{1i} L_d(x, y) = D_{1j} f_i(y, x, v) \tag{2.41a}$$

$$D_{1j} D_{2i} L_d(z, x) = D_{3j} f_i(w, x, z) \tag{2.41b}$$

for all $x, y, z, v, w \in Q$, from where condition (2.40a) follows.

Next, we prove that these conditions are sufficient by constructing a discrete Lagrangian L_d that satisfies (2.39). To this end, we note first that condition (2.40b) guarantees that there exists a function $M : Q \to \mathbb{R}$ such that

$$D_i M(x) = f_i(y_0, x, z_0) \tag{2.42}$$

for all $x \in Q$. In addition, condition (2.40a) implies that we can define a function $G : Q \times Q \to \mathbb{R}^{m \times m}$ that satisfies

$$G_{ij}(x, y) = D_{1j} f_i(y, x, v) = D_{3i} f_j(w, y, x) \tag{2.43}$$

for all $x, y, v, w \in Q$. A second noteworthy observation then is that

$$f_i(w, x, z) - f_i(w, x, z_0) = \int_{z_0}^{z} D_{3j} f_i(w, x, \xi)\ d\xi_j = \int_{z_0}^{z} G_{ji}(\xi, x)\ d\xi_j \tag{2.44}$$

for all $w, x, z, z_0 \in Q$, and therefore, the value of left–hand side of equation (2.44) is *independent* of w.

Consider the discrete Lagrangian

$$L_d(x, y) = M_1(x) + M_2(y) + \int_{y_0}^{y} d\eta_j \int_{x_0}^{x} G_{ij}(\xi, \eta)\ d\xi_i, \tag{2.45}$$

where M_1 and M_2 are real valued functions that satisfy $M(x) = M_1(x) + M_2(x)$. The corresponding discrete Euler–Lagrange equations read

$$\begin{aligned}
D_{1i}L_d(x, y) + D_{2i}L_d(z, x) &= D_i M(x) + \int_{y_0}^{y} G_{ij}(x, \eta)\ d\eta_j + \int_{z_0}^{z} G_{ji}(\xi, x)\ d\xi_j && (2.46)\\
&= f_i(y_0, x, z_0) + \int_{y_0}^{y} D_{1j} f_i(\eta, x, z)\ d\eta_j + \int_{z_0}^{z} D_{3j} f_i(y, x, \xi)\ d\xi_j && (2.47)\\
&= f_i(y_0, x, z_0) + f_i(y, x, z) - f_i(y_0, x, z) + f_i(y, x, z) - f_i(y, x, z_0) && (2.48)\\
&= f_i(y, x, z) + \underbrace{f_i(y, x, z) - f_i(y, x, z_0)}_{\text{Indep. of } y} + \underbrace{f_i(y_0, x, z_0) - f_i(y_0, x, z)}_{\text{Indep. of } y_0} && (2.49)\\
&= f_i(y, x, z), && (2.50)
\end{aligned}$$

where we have used equations (2.42) and (2.43) in (2.47), and equation (2.44) in (2.49). ■

We can now check that conditions (2.40) are satisfied for some of the examples given in this section.

Example I: Generalized midpoint rule. In this case, from equation (2.10), we have

$$f(y, x, z) = M\left(\frac{y - 2x + z}{\Delta t}\right) + \Delta t\Big[(1-\alpha)\nabla V\Big((1-\alpha)x + \alpha y\Big) + \alpha \nabla V\Big((1-\alpha)z + \alpha x\Big)\Big],$$

from where it is a simple exercise to check that conditions (2.40) are satisfied.

Example II: Generalized trapezoidal rule. From equation (2.12) we have

$$f(y, x, z) = M\left(\frac{y - 2x + z}{\Delta t}\right) + \Delta t \nabla V(x),$$

from where it is simple to check that conditions (2.40) are satisfied.

Proposition 2.9.1 gives necessary and sufficient conditions to identify when the function $f(y, x, z)$ that describes the algorithm can be derived from a discrete Lagrangian. Nevertheless, as we said,

we only have a partial answer to the question of when an algorithm is variational.

Notice first that any function of f, of the form $h \circ f$, describes the algorithm as well, as long as $h : \mathbb{R}^m \to \mathbb{R}^m$ satisfies that $h(x) = 0$ if and only if $x = 0$. Even if f satisfies conditions (2.40), it is easy to check that $h \circ f$ may not.

A different perspective is obtained by noticing the implications of a coordinate change on Q on the algorithm. Let $\eta : Q \to Q$ be a one-to-one and onto smooth map, which defines a change of coordinates in Q. The discrete Euler–Lagrange equations corresponding to the discrete Lagrangian $L_d^\eta = L_d(\eta(x), \eta(y))$ are

$$D_1 L_d^\eta(x, y) + D_2 L_d^\eta(z, x) = f^\eta(y, x, z) = f\Big(\eta(y), \eta(x), \eta(z)\Big) \cdot D_1\eta(x) = 0, \tag{2.51}$$

which, since η is invertible, define the same algorithm as

$$f\Big(\eta(y), \eta(x), \eta(z)\Big) = 0. \tag{2.52}$$

Now, if f satisfies conditions (2.40) then f^η will also do, while $f(\eta(y), \eta(x), \eta(z))$ as in equation (2.52) will not.

Occasionally, the right coordinate change can be found, and the variational nature of some algorithms can be unveiled. This is the case for some algorithms in the Newmark family (Newmark [1959]), as was first recognized in Kane et al. [2000], and is discussed below. However, in general this might not be an easy task.

Example III: Variational nature of Newmark. The Newmark family of algorithms for classical mechanical systems is

$$q_{k+1} = q_k + \Delta t v_k + \frac{\Delta t^2}{2}[(1 - 2\beta)a_k + 2\beta a_{k+1}] \tag{2.53}$$

$$a_{k+1} = -M^{-1}\nabla V(q_{k+1}) \tag{2.54}$$

$$v_{k+1} = v_k + \Delta t[(1 - \gamma)a_k + \gamma a_{k+1}], \tag{2.55}$$

where $0 \le \beta \le 1/2$, $0 \le \gamma \le 1$ and q_k, v_k, a_k are the values of positions, velocities and accelerations at time t_k, respectively. In terms of positions only, the family of algorithms with $\gamma = 1/2$ is given by

$$\frac{1}{\Delta t}\Big[(q_{k+1} - \beta\Delta t^2 M^{-1}\nabla V(q_{k+1})) - 2(q_k - \beta\Delta t^2 M^{-1}\nabla V(q_k)) + (q_{k-1} - \beta\Delta t^2 M^{-1}\nabla V(q_{k-1}))\Big] + \Delta t M^{-1}\nabla V(q_k) = 0. \tag{2.56}$$

In Kane et al. [2000] it is shown that the family of algorithms in (2.56) is variational. Nevertheless, it is easy to check that (2.56) does not satisfy conditions (2.40). The variational structure is revealed only after a change of variables

$$x_k = \eta^\beta(q_k) = q_k - \beta\Delta t^2 M^{-1}\nabla V(q_k), \tag{2.57}$$

and the corresponding discrete Lagrangian is

$$L_d(q_k, q_{k+1}) = \frac{\Delta t}{2}\Big(\frac{\eta^\beta(q_{k+1}) - \eta^\beta(q_k)}{\Delta t}\Big)^{\mathsf{T}} M\Big(\frac{\eta^\beta(q_{k+1}) - \eta^\beta(q_k)}{\Delta t}\Big) - \Delta t\tilde{V}(\eta^\beta(q_k)), \tag{2.58}$$

where the new potential $\tilde{V}(x)$ is such that $\nabla V(x) = \nabla\tilde{V}(x)$. The relation between the corresponding discrete Euler–Lagrange equations and (2.56) is equivalent to that between equations (2.51) and (2.52).

As a last remark, notice that when f effectively represents the discrete Euler–Lagrange equations for some discrete Lagrangian, the coefficients of the discrete symplectic form can be written in terms of f by using (2.41). Consequently, identifying when an algorithm is variational is equivalent to knowing what the discrete symplectic form preserved by the algorithm is. Even in the continuous case, it is only possible to test if, given a symplectic structure, a set of equations is Euler–Lagrange, but it is not generally known how to answer the converse question.

Chapter 3

Asynchronous variational integrators

Dynamical systems that exhibit well-separated multiple timescales arise in many areas of application, including molecular dynamics, microstructural evolution in materials, and structural mechanics. In a numerical treatment of these problems, it is natural to consider time stepping algorithms with multiple time steps chosen to resolve the various timescales in the problem. In this chapter we introduce one class of such time integrators, termed *asynchronous variational integrators* (AVI), characterized by the following distinguishing attributes:

1. When applied to dynamical systems defined by the finite element method, AVIs permit the selection of different time steps for each element. The local time steps need not bear an integral relation to each other, and the integration of the elements may, therefore, be carried out *asynchronously*.

2. The time-integration algorithm is obtained within the theory of Discrete Mechanics, and therefore the algorithms have remarkable momentum and energy conservation properties and are *variational*.

We begin the chapter by reviewing the Lagrangian formulation of continuum mechanics and the variational principles that give rise to the motion. We mimic this development in the discrete setting to obtain one example of AVIs, and simultaneously, its conservation properties. We discuss its implementation, cost and complexity, and show several numerical examples. In particular, we include examples on the dynamic response of thermoelastic materials to shock loading, where the time steps are dynamically adapted to accurately track the evolution of the sharp front. To this end we also briefly explain an artificial viscosity scheme that enables the stable numerical propagation of shocks in largely deforming solids.

3.1 Formulation of the continuum problem

We begin this chapter by reviewing the Lagrangian description of continuum elastic bodies undergoing finite deformations and the derivation of the governing equations from Hamilton's principle. Later, in Chapter 4, we review the abstract formulation of space–time Lagrangian mechanics, which include the traditional framework that follows within a more general setting.

3.1.1 Lagrangian description of motion

In describing the dynamic response of elastic bodies under loading, we select a reference configuration $\mathcal{B} \subset \mathbb{R}^3$ of the body at time t_0. The coordinates of points $X \in \mathcal{B}$ are used to identify material particles throughout the motion. The motion of the body is described by the deformation mapping

$$x(t) = \varphi(X, t), \qquad X \in \mathcal{B}. \tag{3.1}$$

Thus, x is the location of material particle X at time t. The material velocity and acceleration fields follow from (3.1) as $\dot{\varphi}(X, t)$ and $\ddot{\varphi}(X, t)$, $X \in \mathcal{B}$, respectively, where a superposed dot denotes partial differentiation with respect to time at fixed material point X. The deformation mapping is subject to essential boundary conditions on the displacement boundary $\partial_d\mathcal{B} \subset \partial\mathcal{B}$.

The local deformation of infinitesimal material neighborhoods is described by the deformation gradient

$$F^i{}_I = \frac{\partial \varphi^i}{\partial X^I}(X, t), \qquad X \in \mathcal{B}. \tag{3.2}$$

The scalar function

$$J = \det\big(F(X, t)\big) \tag{3.3}$$

is the Jacobian of the deformation.

In order to allow for general mixed boundary conditions, we partition the boundary $\partial\mathcal{B}$ of $\mathcal{B}$ into a Dirichlet or displacement boundary $\partial_d\mathcal{B}$, and a Neumann or traction boundary $\partial_\tau\mathcal{B}$. The displacement boundary conditions then take the form:

$$\varphi = \varphi_0 \qquad \text{on } \partial_d\mathcal{B}, \tag{3.4}$$

where $\varphi_0(X, t)$ is the prescribed deformation mapping on $\partial_d\mathcal{B}$. The tractions applied on $\partial_\tau\mathcal{B}$ are denoted by $\tau(X, t)$.

3.1.2 Hyperelastic materials

Hyperelastic materials are characterized by stress-deformation relations of the form:

$$P_i{}^I = \frac{\partial}{\partial F^i{}_I} W(F, X), \tag{3.5}$$

where P is the first Piola–Kirchhoff stress tensor (see, for example, Marsden and Hughes [1994]), and W is the strain-energy density per unit undeformed volume. The strain-energy density is a function of $X \in \mathcal{B}$ and $F \in \mathbb{R}^{3\times 3}$, such that $\det F > 0$, and is subject to the requirement of material frame indifference, i.e.,

$$W(Q \cdot F, X) = W(F, X)$$

for all rotations $Q \in SO(3)$. The Cauchy stress tensor follows from P through the relation

$$\sigma_{ij} = J^{-1} P_i{}^I F_{jI}. \tag{3.6}$$

In particular, when the Cauchy stress tensor has no deviatoric component we have that

$$P_i{}^I = J\ p\ (F^{-1})^I{}_i, \tag{3.7}$$

where $p = \sigma_{kk}/3$ is the pressure, which we assumed to be positive under compression as traditionally done in fluid mechanics.

Neohookean material. A convenient choice of strain-energy density adopted in the numerical tests presented subsequently is

$$W(F, X) = \frac{\lambda_0(X)}{2} (\log J)^2 - \mu_0(X) \log J + \frac{\mu_0(X)}{2} \mathrm{tr}\left(F^{\mathsf{T}} F\right), \tag{3.8}$$

which describes a Neohookean solid extended to the compressible range. In this expression, $\lambda_0(X)$ and $\mu_0(X)$ are — possibly inhomogeneous — Lamé constants. The corresponding stress — deformation relation follows from (3.5) in the form:

$$P = \lambda_0 \log J\, F^{-\mathsf{T}} + \mu_0 \left(F - F^{-\mathsf{T}}\right). \tag{3.9}$$

3.1.3 Viscous materials

Materials exhibiting viscous effects have contributions to the stress tensor stemming from the viscous response in addition to any elastic behavior. For these materials the stress tensor follows as

$$P = P^e + P^v, \tag{3.10}$$

where P^e is the elastic response computed from (3.5) and $P^v(\dot{F}; F)$ is the viscous stress. We shall assume Newtonian viscosity, whence the viscous stresses take the form

$$P^v(\dot{F}, F) = J\sigma^v F^{-T}, \tag{3.11}$$

with

$$\sigma^v = 2\eta(\mathrm{sym}\dot{F}F^{-1})^{\mathrm{dev}}. \tag{3.12}$$

Here η is the Newtonian viscosity coefficient, and sym and dev denote the symmetric and deviatoric components of a tensor, respectively.

Henceforth, unless otherwise stated, we will assume materials to be hyperelastic, and therefore $P = P^e$. We will consider viscous materials when stating the Lagrange-D'alembert principle for a continuum in section 3.1.5, its discrete asynchronous extension in section 3.2.4, and in some of the numerical examples in section 3.5.4.

3.1.4 Hamilton's principle

For definiteness, the potential energy of the body is assumed to be of the form

$$\Phi[\varphi(\cdot, t), t] = \int_{\mathcal{B}} W(\nabla_X \varphi, X)\, dX + \int_{\mathcal{B}} \rho_0 V(X, \varphi, t)\, dX - \int_{\partial_\tau \mathcal{B}} \tau \cdot \varphi\, dS, \tag{3.13}$$

where ρ_0 is the mass density per unit of undeformed volume, $\nabla_X \varphi$ is the deformation gradient and $V(X, \varphi, t)$ is the external potential energy per unit mass, such as gravity. In addition, the kinetic energy of the body is assumed to be of the form

$$T[\dot{\varphi}(\cdot, t)] = \int_{\mathcal{B}} \frac{\rho_0}{2} |\dot{\varphi}|^2\, dX. \tag{3.14}$$

The corresponding Lagrangian of the body is

$$L(\varphi(\cdot, t), \dot{\varphi}(\cdot, t), t) = T[\dot{\varphi}] - \Phi[\varphi, t]. \tag{3.15}$$

Consider now a motion of the body during the time interval $[t_0, t_f]$. The action attendant to the motion is

$$S[\varphi(\cdot, \cdot)] = \int_{t_0}^{t_f} L(\varphi, \dot{\varphi}, t) dt. \tag{3.16}$$

We note that, upon insertion of (3.15) in (3.16), the evaluation of the action functional entails a *space–time* integral. This viewpoint will be further developed in Chapter 4.

Within the framework just outlined, Hamilton's principle postulates that the motion $\varphi(X, t)$ of the body which joins prescribed initial and final conditions renders the action functional S stationary

with respect to all admissible variations, i.e., variations of $\varphi(X,t)$ vanishing at t_0 and t_f and that satisfy the essential boundary conditions on $\partial_d\mathcal{B}$. A standard calculation shows that under appropriate smoothness hypotheses, the Euler–Lagrange equations corresponding to Hamilton's principle are

$$D_1L(\varphi,\dot\varphi,t)-\frac{d}{dt}D_2L(\varphi,\dot\varphi,t)=0 \tag{3.17}$$

for all $t\in[t_0,t_f]$, in an analogous way to (2.3). For the Lagrangian (3.15), (3.17) gives

$$\frac{\partial P_i{}^I}{\partial X^I}-\frac{\partial V}{\partial\varphi^i}(X,\varphi,t)-\rho_0\ddot\varphi=0 \tag{3.18}$$

for all $X\in\mathcal{B}$ and $t\in[t_0,t_f]$, as well as the traction boundary conditions

$$P\cdot N=\tau \tag{3.19}$$

on $\partial_\tau\mathcal{B}$ and for all $t\in[t_0,t_f]$. In (3.19) N denotes the unit outward normal over $\partial_\tau\mathcal{B}$.

3.1.5 Lagrange-D'alembert principle

The Lagrange-D'alembert principle (see section 2.3) for continuum mechanics acquires the form

$$\delta\int_{t_0}^{t_f}L(\varphi,\dot\varphi,t)\,dt+\int_{t_0}^{t_f}\Big[\int_{\mathcal{B}}B(\varphi,\dot\varphi,t)\,\cdot\delta\varphi+\int_{\partial_\tau\mathcal{B}}\tau_B(\varphi,\dot\varphi,t)\,\cdot\delta\varphi\Big]\,dt=0 \tag{3.20}$$

for all admissible variations $\delta\varphi$, where B is a force per unit undeformed volume and τ_B is a undeformed surface traction forcing term. The corresponding equations of motion are

$$B_i+\frac{\partial}{\partial X^I}\frac{\partial W}{\partial F^i_{\ I}}-\frac{\partial V}{\partial\varphi^i}(X,\varphi,t)-\rho_0\ddot\varphi=0\qquad\text{in }\mathcal{B} \tag{3.21}$$

$$P\cdot N-\tau-\tau_B=0\qquad\text{on }\partial_\tau\mathcal{B}. \tag{3.22}$$

We will use the Lagrange-D'alembert principle, in lieu of Hamilton's principle, when considering materials with viscosity. In this case

$$B_i=\frac{\partial(P^v)_i{}^I}{\partial X^I} \tag{3.23}$$

$$(\tau_B)_i=-(P^v)_i{}^IN_I. \tag{3.24}$$

3.2 Formulation of the discrete problem

3.2.1 Spatial discretization

Let $\mathcal{T}$ be a triangulation of $\mathcal{B}$. The corresponding finite–dimensional space of finite-element solutions consists of deformation mappings of the form

$$\varphi_h(X) = \sum_{a \in \mathcal{T}} x_a \, N_a(X), \tag{3.25}$$

where N_a is the shape function corresponding to node a, x_a represents the position of the node in the deformed configuration. A key observation underlying the formulation of AVIs is that, owing to the extensive character of the Lagrangian (3.15), the following element-by-element additive decomposition holds:

$$L = \sum_{K \in \mathcal{T}} L_K, \tag{3.26}$$

where L_K is the contribution of element $K \in \mathcal{T}$ to the total Lagrangian, which follows by restricting (3.15) to K. Each elemental or local Lagrangian L_K can in turn be written as a function of the nodal positions and velocities of the element, i.e.,

$$L_K(\varphi_h(\cdot,t), \dot{\varphi}_h(\cdot,t), t) \equiv L_K(x_K(t), \dot{x}_K(t), t), \tag{3.27}$$

where x_K is the vector of positions of all the nodes in element K. In particular, for the Lagrangian (3.15) the local Lagrangians have the form

$$L_K(x_K, \dot{x}_K, t) = T_K(\dot{x}_K) - \Phi_K(x_K, t), \tag{3.28}$$

where $\Phi_K(x_K, t)$ is the elemental potential energy

$$\Phi_K(x_K, t) = \int_K \left[W(\nabla_X \varphi_h, X) + \rho_0 V(X, \varphi_h, t) \right] \, dX - \int_{\partial K \cup \partial_\tau \mathcal{B}} \tau \cdot \varphi_h \, dS, \tag{3.29}$$

and

$$T_K(\dot{x}_K) = \sum_{a \in K} \frac{1}{2} m_{K,a} \, \dot{x}_K^{\mathsf{T}} \cdot \dot{x}_K \tag{3.30}$$

is the elemental kinetic energy. We assumed above that the elemental mass matrix is expressible in diagonal or lumped form, and $m_{K,a}$ is the mass of node a as contributed by element K. In other words, $m_{K,a}$ is the diagonal coefficient of node a in the lumped elemental mass matrix.

Mass-lumping schemes. For the sake of completeness, we detail in Figure 3.1 the elemental mass-lumping schemes that have been utilized in the examples shown in the present work. Additional

mass-lumping procedures can be found elsewhere (see, e.g., Hughes [1987]).

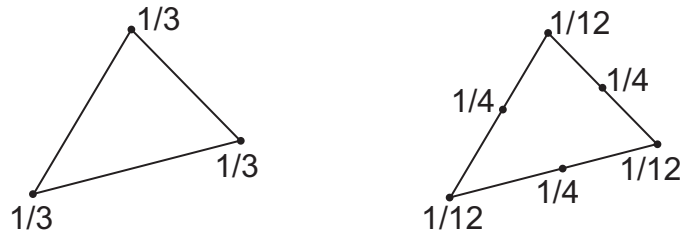

(a) Linear (b) Quadratic

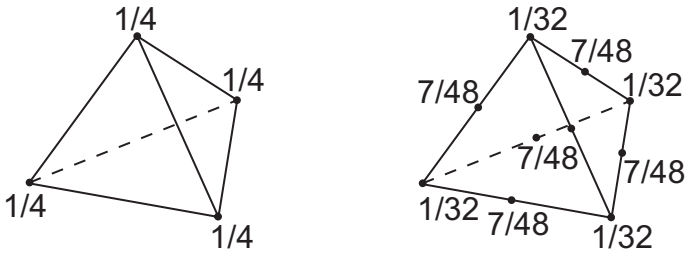

(c) Linear (d) Quadratic

Figure 3.1: Mass lumping schemes for linear and quadratic triangles and tetrahedra. The number beside a node indicates the fraction of the total mass of the element that is assigned to it.

3.2.2 Asynchronous time discretization

By adding the elemental Lagrangians (3.28) over all elements of the mesh, an action describing the motion of a finite–dimensional semidiscrete[1] system is obtained. Variational time integrators for this system are constructed by following the theory outlined in Chapter 2. One such algorithm is, for example, the widely used explicit second-order Newmark. Algorithms of this type utilize a single time step to evolve in time all degrees of freedom.

In the following we introduce a more general and powerful class of variational algorithms well-suited to deal with problems involving multiple timescales. In this case, elements and nodes defining the triangulation of the body are updated *asynchronously* in time. To this end, we endow each element $K \in \mathcal{T}$ with a discrete time set

$$\Theta_K = \{t_0 = t_K^1 < \ldots < t_K^{N_K - 1} < t_K^{N_K}\}, \tag{3.31}$$

with $t_K^{N_K-1} < t_f \leq t_K^{N_K}$. In addition, we write $\mathbf{x}_K^j \equiv \mathbf{x}_K(t_K^j)$, $t_K^j \in \Theta_K$, for the discrete element

[1] Continuous in the time variable, discrete in the spatial variables

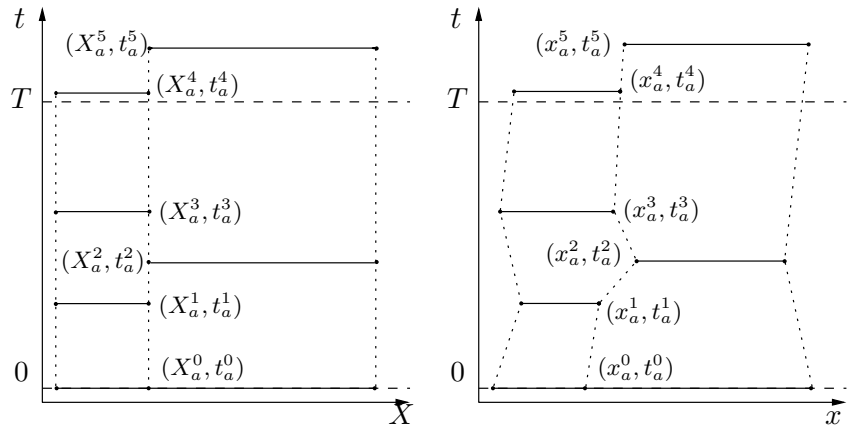

(a) Reference configuration (b) Deformed configuration

Figure 3.2: Space–time diagram of the motion of a two–element, one–dimensional mesh. The set of coordinates and times for a single node is shown in the reference and deformed configuration. Note that the nodal coordinates and times are labeled according to the interaction of the node with all elements to which it belongs. The horizontal segments above each element K define the set Θ_K.

coordinates, and

$$\Theta = \bigsqcup_{K \in \mathcal{T}} \Theta_K \tag{3.32}$$

for the entire time set. We shall also need to keep proper time at all nodes in the mesh. To this end, we let

$$\Theta_a = \bigsqcup_{\{K \in \mathcal{T} | a \in K\}} \Theta_K = \{t_0 = t_a^1 \leq \ldots \leq t_a^{N_a - 1} \leq t_a^{N_a}\} \tag{3.33}$$

denote the ordered nodal time set for node a. In these definitions, the symbol $\bigsqcup$ denotes disjoint union[2]. For notational simplicity, we assume that $t_K^j \neq t_{K'}^{j'}$ for any pair of elements K and K'. The case of time coincidences between elements can be treated simply by taking the appropriate limits and does not change any of our results. We additionally write $x_a^i = x_a(t_a^i)$, $t_a^i \in \Theta_a$, for the discrete nodal coordinates, and let

$$\Xi = \{x_a^i,\ a \in \mathcal{T},\ i = 1, \ldots N_a\} \tag{3.34}$$

denote the set of nodal coordinates defining the discrete trajectory.

The particular class of AVIs under consideration here is obtained by allowing each node $a \in \mathcal{T}$ to follow a linear trajectory within each time interval $[t_a^i, t_a^{i+1}]$. The corresponding nodal velocities are piecewise constant in time. The nodal trajectories thus constructed are defined in the time intervals $[t_0, t_a^{N_a}]$. An $x - t$ diagram of the motion of a two–element one–dimensional mesh is shown in Figure

[2]The disjoint union of the sets A_i is equal to the union of all A_i's but retaining as many copies of each element as there originally were in all the sets. For example, $\{a, b\} \bigsqcup \{a, c\} = \{a, a, b, c\}$

3.2 by way of illustration. More general AVI methods could also be devised by considering piecewise polynomial nodal trajectories.

We note that the pair of sets (Ξ, Θ) completely defines the trajectories of the discrete system. A class of discrete dynamical systems is obtained by considering discrete action sums of the form

$$S_d(\Xi, \Theta) = \sum_{K \in \mathcal{T}} \sum_{1 \le j < N_K} L_K^j, \tag{3.35}$$

where the discrete Lagrangian L_K^j approximates the incremental action of element K over the interval $[t_K^j, t_K^{j+1}]$, i.e.,

$$L_K^j \approx \int_{t_K^j}^{t_K^{j+1}} L_K \, dt. \tag{3.36}$$

In general, L_K^j depends on some subset of Ξ of nodal coordinates, and some subset of Θ of elemental times. Specifically, L_K^j depends on the time set

$$\Theta_K^j = \bigcup_{\substack{K' \in \mathcal{T} \\ K' \cap K \neq \emptyset}} \left\{ \Theta_{K'} \cap [t_K^j, t_K^{j+1}] \right\}. \tag{3.37}$$

Likewise, L_K^j depends on the nodal coordinate set

$$\Xi_K^j = \left\{ x_a^i, \ a \in K, \ t_a^i \in \Theta_K^j \right\}. \tag{3.38}$$

A particular choice of discrete Lagrangian, resulting in explicit integrators of the central-difference type, is given by

$$L_K^j = \int_{t_K^j}^{t_K^{j+1}} T_K(\dot{x}_K(t)) \, dt - (t_K^{j+1} - t_K^j) \, \Phi_K(x_K^{j+1}, t_K^{j+1}). \tag{3.39}$$

The corresponding discrete action sum is

$$S_d = \sum_a \sum_{i=0}^{N_a - 1} \frac{1}{2} m_a (t_a^{i+1} - t_a^i) \left\| \frac{x_a^{i+1} - x_a^i}{t_a^{i+1} - t_a^i} \right\|^2 - \sum_K \sum_{j=0}^{N_K - 1} (t_K^{j+1} - t_K^j) \, \Phi_K(x_K^{j+1}, t_K^{j+1}), \tag{3.40}$$

where m_a is the value of the total mass for node a, i.e., $m_a = \sum_K m_{K,a}$.

Molecular Dynamics. Discrete Lagrangians of the type (3.39) are very useful and convenient for dynamic continuum mechanics problems. However, they are not fundamental to construct variational asynchronous discretizations of other mechanical systems, such as those corresponding to molecular dynamics. Consider a system of N_a particles with dynamics described by a Lagrangian of the form

$$L(x, \dot{x}) = \sum_a \frac{1}{2} m_a \|\dot{x}_a\|^2 - \sum_K \Phi_K(x), \tag{3.41}$$

where m_a is the mass of particle a at position $x_a \in \mathbb{R}^3$. Here the potentials Φ_K represent the interaction between pairs (or triples) of particles, so that we have $\Phi_{ab} = \Phi(\|x_b - x_a\|)$ for all $a < b$ and some given $\Phi(r)$. Each subsystem K can be regarded as equivalent to an element in a finite element mesh, and each particle to a node. It is the decomposition of the total potential energy into subsystems which permits the asynchrony of the time discretization. However, it is not natural in this case to partition the masses as in equation (3.30) to construct discrete Lagrangians associated to each subsystem, but rather to construct a discrete action sum as (3.40) directly.

Configurations of the discrete system. Since the various elements in the system evolve asynchronously, the definition of a configuration of the system requires some care. To this end, regard Θ as an ordered set. The order of the discrete times t_K^j in Θ determines the order in which the various elements in the triangulation become active. Let $N_{\mathcal{T}}$ be the number of elements in the triangulation. For every integer $N_{\mathcal{T}} \leq m \leq N_\Theta$, let Θ_m be set containing the first m times in Θ. In addition, we introduce the partial element and nodal time sets $\Theta_{K,m} = \Theta_K \cap \Theta_m$ and $\Theta_{a,m} = \Theta_a \cap \Theta_m$, and let $N_{K,m}$ and $N_{a,m}$ be their cardinals, respectively. Then, the mth configuration of the system is defined as the collection of all the element configurations corresponding to times $t_K^{N_{K,m}}$. For each configuration m, define also the final time $t_f^m = \min_K t_K^{N_{K,m}}$. A simple example illustrative of this definition is shown in Figure 3.3. The initial configuration of the system is the $N_{\mathcal{T}}$-th configuration, while the final configuration is the N_Θth configuration.

For each configuration m, we will denote with $S_{d,m}$ the partial action sum over the time set Θ_m corresponding to the mth configuration of the system.

3.2.3 Discrete Euler–Lagrange equations

The discrete version of Hamilton's principle states that the discrete trajectory having prescribed initial and final end points renders the discrete action sum stationary with respect to admissible variations of the coordinate set Ξ. Note that since each element carries its own set of time steps, the final configurations of the elements, corresponding to $t_K^{N_K} \geq t_f$, $K \in \mathcal{T}$, are not synchronized in general. Thus, x_a^i is not to be varied if $t_a^i \geq t_f$, as the node belongs to the final configuration of some element in the mesh. Similarly, the initial nodal positions at $t = t_0$ are not to be varied. The discrete Hamilton's principle leads to the discrete Euler–Lagrange equations:

$$D_a^i S_d = 0 \tag{3.42}$$

for all $a \in \mathcal{T} \setminus \partial_d \mathcal{B}$ such that $t_a^i \in (t_0, t_f)$. Here and subsequently, D_a^i denotes differentiation with respect to x_a^i. If the discrete time set Θ is given *a priori*, then the discrete equations of motion (3.42) determine the coordinate sets Ξ which define the discrete trajectories of the system.

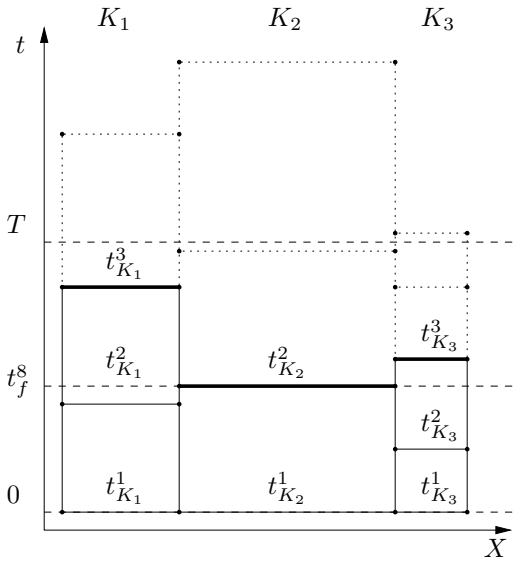

Figure 3.3: Configuration number 8 (in thick lines) for the space–time diagram shown, corresponding to a one–dimensional three-element mesh. $\Theta = \{t^1_{K_1}, t^1_{K_2}, t^1_{K_3}, t^2_{K_3}, t^2_{K_1}, t^2_{K_2}, t^3_{K_3}, t^3_{K_1}, \ldots\}$, $N_{\mathcal{T}} = 3$ and $N_\Theta = 13$.

After introducing the definition of the discrete Lagrangian (3.39) under consideration into (3.42), a straightforward calculation gives the discrete Euler–Lagrange equations explicitly in the form

$$p_a^{i+1/2} - p_a^{i-1/2} = I_a^i, \tag{3.43}$$

where

$$p_a^{i+1/2} \equiv m_a \, \frac{x_a^{i+1} - x_a^i}{t_a^{i+1} - t_a^i} \equiv m_a \, v_a^{i+1/2} \tag{3.44}$$

are discrete linear momenta. In addition, we define

$$I_K^j \equiv -(t_K^j - t_K^{j-1}) \, \frac{\partial}{\partial x_K^j} \Phi_K(x_K^j), \tag{3.45}$$

which may be regarded as the impulses exerted by element K on its nodes at time t_K^j. In equation (3.43) I_a^i represents the component of I_K^j corresponding to node a, with $t_a^i = t_K^j$. Equation (3.43) may be interpreted as describing a sequence of percussions imparted by the elements on their nodes at discrete instants of time. Thus, the element K accumulates and stores impulses I_K^j over the time interval (t_K^{j-1}, t_K^j). At the end of the interval, the element releases its stored impulses by imparting percussions on its nodes, causing the linear momentum of the nodes to be altered. The resulting nodal trajectories can be regarded as piecewise linear in time. We note that adjacent elements interact by transferring linear momentum through their common nodes. Note that the resulting algorithm is explicit of the central-difference type.

3.2.4 Discrete Lagrange-D'alembert principle for asynchronous discretizations

When considering systems with forcing, an appropriate notion of a discrete Lagrange-D'alembert principle for AVI discretizations is needed. One natural extension of the principle discussed in section 2.3 is constructed by seeking discrete trajectories that satisfy

$$D_a^i S_d + \sum_{\{K | a \in K\}} \mathcal{F}_{K,a}^{j,i} = 0 \tag{3.46}$$

for all $a \in \mathcal{T} \setminus \partial_d \mathcal{B}$ such that $t_a^i \in (t_0, t_f)$, where $\mathcal{F}_{K,a}^{j,i}(\Xi_K^j, \Theta_K^j)$ is the discrete force exerted by element K on node a at time $t_a^i \in [t_K^j, t_K^{j+1}]$. These forces should satisfy

$$\sum_{x_a^i \in \Xi_K^j} \mathcal{F}_{K,a}^{j,i} \delta x_a^i \approx \int_{t_K^j}^{t_K^{j+1}} \left[\int_K B \cdot \delta\varphi + \int_{\partial K \cap \partial_\tau \mathcal{B}} \tau_B \cdot \delta\varphi \right]. \tag{3.47}$$

A particular choice of discrete forces for materials exhibiting viscous response that allows for asynchronous explicit updates is given by

$$\mathcal{F}_{K,a}^{j,i} = \begin{cases} (t_K^{j+1} - t_K^j) \displaystyle\int_K P^v \left(\frac{F_K^{j+1} - F_K^j}{t_K^{j+1} - t_K^j}, F_K^j \right) : \nabla_X N_a \, dX & \text{if } t_a^i = t_K^{j+1} \\ 0 & \text{otherwise} \end{cases}, \tag{3.48}$$

where F_K^j indicates the deformation gradient over K at time t_K^j, a function of x_K^j. Following Radovitzky and Ortiz [1999] and Lew et al. [2001], we computed the viscous stress P^v by using a difference approximation for $\dot{F}$. Notice that, as formulated, the discrete forces follow the same spirit as the discrete Lagrangian (3.39), in that each element imparts impulses to the nodes only at the end of each interval. This makes the implementation of these forces particularly simple within the same algorithm outlined in section 3.3.

3.3 Implementation of AVIs

In this section we turn our attention to discussing the implementation of the AVI corresponding to the discrete Lagrangian (3.39).

Because of the algorithm's asynchronous nature, a suitable scheduling procedure which determines the order of operations while ensuring causality must be carefully designed. One particularly efficient implementation consists of maintaining a priority queue (see, e.g., Knuth [1998]) containing the elements of the triangulation.[3] The elements in the priority queue are ordered according to the

[3] We stress that this is only one possibility for ordering the computation, and is not imposed by the discrete

next time at which they are to become active. Thus, the top element in the queue, and consequently the next element to be processed, is the element whose next activation time is closest to the present time.

The general flow of the calculations is as follows. The priority queue is popped in order to determine the next element to be processed. The new configuration of this active element is computed from the current velocities of the nodes. Subsequently, these velocities are modified by impulses computed based on the new element configuration. Finally, the next activation time for the element is computed and the element is pushed into the queue. A flow chart of the numerical procedure is given in Figure 3.4. Note that the algorithm allows the time step of each element to change in time.

Explicit AVI Algorithm

Input data: $T, \mathcal{T}, \left\{ x_a^0, \dot{x}_a^{1/2} \mid a \in \mathcal{T} \right\}$

- ▷ Initialization
  - ▷ $q_a \leftarrow x_a^0$, $v_a \leftarrow \dot{x}_a^{1/2}$, $\theta_a \leftarrow 0$ for all $a \in \mathcal{T}$
  - ▷ Do for all $K \in \mathcal{T}$
    - ▷ $\theta_K \leftarrow 0$
    - ▷ Compute t_K^1
    - ▷ Push (t_K^1, K) into priority queue
  - ▷ End Do
- ▷ Iterate over the elements in time
  - ▷ Do until priority queue is empty
    - ▷ Extract next element: Pop (t, K) from priority queue
    - ▷ Update positions: $q_a \leftarrow q_a + v_a\,(t - \theta_a)$, for all $a \in K$
    - ▷ Update node's time: $\theta_a \leftarrow t$, for all $a \in K$
    - ▷ If $t < T$
      - ▷ Update velocities: $v_a \leftarrow v_a - (t - \theta_K)\,\frac{\partial V_K}{\partial x_a}\,(q_K)\,/m_a$, for all $a \in K$
      - ▷ Update element's time: $\theta_K \leftarrow t$
      - ▷ Compute t_K^{next}
      - ▷ Schedule K for next update: Push (t_K^{next}, K) into priority queue
  - ▷ End Do
- ▷ End

Figure 3.4: Algorithm implementing the discrete Euler–Lagrange equations of the action sum given by equation (3.39).

The use of the priority queues is particularly simple in C++, since these are provided by several

Euler–Lagrange equations. We will discuss some other possibilities in §3.7.

freely available libraries. Also, routines implementing priority queues in C are freely available to download. Priority queues are frequently implemented through balanced binary trees [Knuth, 1998, pp.458].

The adaption of existing FE codes to implement the explicit AVI integrator is fairly simple. The computations at the element level remain untouched, while the driver that assembles the global internal force vector should be removed, since there is no assembly required. Instead, a driver that implements the operations in Figure 3.4 should be coded. Notice that apart from the priority queue and two arrays to store elemental and nodal times, respectively, no extra storage nor new arrays are required over traditional explicit Newmark schemes. To plot the configuration of the continuum, a short routine computing the positions of the nodes at the time of the most advanced element is needed. In this case, each node is advanced by following a linear trajectory parallel to its velocity. It is noteworthy that explicit AVIs allows for the reuse of most of the existing FE structural dynamics codes.

3.4 Momentum conservation properties

We will obtain next the statement of linear angular and momentum balance between the initial and the mth configuration of the system for asynchronous algorithms. We proceed by following similar steps as those used in Chapter 2 to derive Noether's theorem. However, the invariance of the action will not be assumed *a priori*, and consequently we will obtain global balances, instead of conservation of linear and angular momentum between the two configurations. To this end, we consider a one–parameter group of trajectories with nodal positions given by $(x_a^i)^\varepsilon = \exp(\varepsilon\Omega)x_a^i + \varepsilon v$, for any vector $v \in \mathbb{R}^3$ and skew–symmetric matrix Ω. We write $\Xi^\varepsilon = \{(x_a^i)^\varepsilon \mid x_a^i \in \Xi\}$, and introduce the one–parameter family of perturbed actions:

$$S_{d,m}(\varepsilon) = S_{d,m}\left(\Xi^\varepsilon, \Theta\right). \tag{3.49}$$

Assuming differentiability, the following identities hold:

$$S'_{d,m}(0) \;=\; \left[\sum_{a\in\mathcal{T}}\sum_{t_a^i\in\Theta_{a,m}} D_a^i S_{d,m}\right]\cdot v + \sum_{a\in\mathcal{T}}\sum_{t_a^i\in\Theta_{a,m}} D_a^i S_{d,m}\cdot(\Omega x_a^i) \;=\; R\cdot v + M\cdot\omega, \tag{3.50}$$

where $\omega \in \mathbb{R}^3$ is the axial vector of Ω, or, in terms of Hodge's star operator $(*)$, $\omega = *\Omega$, and

$$R = \sum_{a \in \mathcal{T}} \sum_{t_a^i \in \Theta_{a,m}} D_a^i S_{d,m} \tag{3.51}$$

$$M = \sum_{a \in \mathcal{T}} \sum_{t_a^i \in \Theta_{a,m}} x_a^i \times D_a^i S_{d,m} \tag{3.52}$$

are the resultant force and moment, respectively. Here and in the remainder of this derivation, a prime denotes differentiation with respect to ε.

Assume, in addition, that the trajectory of the system satisfies the discrete Euler–Lagrange equations (3.42). Then, $D_a^i S_{d,m} = 0$, for all $a \in \mathcal{T}$ such that x_a^i is unconstrained and $t_0 < t_a^i < t_m^f$. For simplicity, assume also that m is such that $t_f^m > t_0$. Under these conditions, equation (3.51) reduces to

$$\sum_{a \in \mathcal{T}} \sum_{\substack{t_a^i \in \Theta_{a,m} \\ t_a^i = t_0}} D_a^i S_{d,m} + \sum_{a \in \mathcal{T}} \sum_{\substack{t_a^i \in \Theta_{a,m} \\ t_a^i \geq t_f^m}} D_a^i S_{d,m} = R - \sum_{a \in \mathcal{T} \cap \partial_d \mathcal{B}} \sum_{\substack{t_a^i \in \Theta_{a,m} \\ t_0 < t_a^i < t_f^m}} D_a^i S_{d,m}, \tag{3.53}$$

which expresses the balance of linear momentum for all intermediate configurations. In particular, if the discrete action sum is invariant under rigid translations, then $R = 0$. If, in addition $\partial_d \mathcal{B} = \emptyset$, then (3.53) reduces to

$$\sum_{a \in \mathcal{T}} \sum_{\substack{t_a^i \in \Theta_{a,m} \\ t_a^i = t_0}} D_a^i S_{d,m} = -\sum_{a \in \mathcal{T}} \sum_{\substack{t_a^i \in \Theta_{a,m} \\ t_a^i \geq t_f^m}} D_a^i S_{d,m}, \tag{3.54}$$

which furnishes a precise statement of linear momentum conservation for the discrete system. Likewise, the angular momentum balance equation takes the form

$$\sum_{a \in \mathcal{T}} \sum_{\substack{t_a^i \in \Theta_{a,m} \\ t_a^i = t_0}} x_a^i \times D_a^i S_{d,m} + \sum_{a \in \mathcal{T}} \sum_{\substack{t_a^i \in \Theta_{a,m} \\ t_a^i \geq t_f^m}} x_a^i \times D_a^i S_{d,m} = M - \sum_{a \in \mathcal{T} \cap \partial_d \mathcal{B}} \sum_{\substack{t_a^i \in \Theta_{a,m} \\ t_0 < t_a^i < t_f^m}} x_a^i \times D_a^i S_{d,m}. \tag{3.55}$$

In the particular case in which the discrete action sum is invariant under rigid rotations and $\partial_d \mathcal{B} = \emptyset$, we have

$$\sum_{a \in \mathcal{T}} \sum_{\substack{t_a^i \in \Theta_{a,m} \\ t_a^i = t_0}} x_a^i \times D_a^i S_{d,m} = -\sum_{a \in \mathcal{T}} \sum_{\substack{t_a^i \in \Theta_{a,m} \\ t_a^i \geq t_f^m}} x_a^i \times D_a^i S_{d,m}, \tag{3.56}$$

which is a statement of angular momentum conservation for the discrete system.

By way of illustration, for the particular Lagrangian (3.39), the linear and angular momentum

balance equations follow, after some trite manipulations, as

$$\sum_{a\in\mathcal{T}\setminus\partial_d\mathcal{B}} p_a^{i_a^m-1/2} - \sum_{a\in\mathcal{T}\setminus\partial_d\mathcal{B}} p_a^{1/2} - \sum_{a\in\mathcal{T}\setminus\partial_d\mathcal{B}} \sum_{t_0<t_a^i<t_f^m} I_a^i = 0 \tag{3.57}$$

and

$$\sum_{a\in\mathcal{T}\setminus\partial_d\mathcal{B}} x_a^{i_a^m} \times p_a^{i_a^m-1/2} - \sum_{a\in\mathcal{T}\setminus\partial_d\mathcal{B}} x_a^1 \times p_a^{1/2} - \sum_{a\in\mathcal{T}\setminus\partial_d\mathcal{B}} \sum_{t_0<t_a^i<t_f^m} x_a^i \times I_a^i = 0, \tag{3.58}$$

respectively, where i_a^m is such that $t_a^{i_a^m} = \min\{t \in \Theta_{a,m} \mid t \geq t_f^m\}$. Evidently, these equations conform with the familiar intuition that change in linear and angular momentum should equal the total impulse and moment of impulse imparted to the system.

In section 4.4 we consider the formulation of Noether's theorem for asynchronous discretizations and general symmetries.

3.5 Numerical examples

In this section we illustrate the performance of an explicit AVI through several selected examples in structural dynamics, namely, the free oscillatory motion of a two–dimensional block and a three–dimensional L–shaped beam, and the simulation of the motion in vacuum of a simplified model of the blades of an Apache AH-64 helicopter. Moreover, to exhibit the definite suitableness of AVIs for the computation of complex multiphysics problems involving multiple timescales, we present examples of strong shock waves and high-explosive detonation waves propagating in thermoelastic materials.

In all examples, unless otherwise stated, the elemental time steps are determined from the Courant condition, which provides an estimate of the stability limit for explicit integration (cf, e.g., Hughes [1987]). Specifically, the value of the time step for each element is set to a fraction of the Courant limit and is computed as

$$\Delta t = f\ \frac{h}{c}, \tag{3.59}$$

where $f = 1/10$, h is the radius of the largest ball contained in the element, and

$$c = \sqrt{\frac{\lambda_0 + 2\mu_0}{\rho_0}}, \tag{3.60}$$

which is the speed of propagation of volumetric waves in the undeformed state of the material. The time step is kept constant in each element throughout the computation. We note that the elemental time steps are not required to be integer-related, and the element trajectories are not synchronized in general.

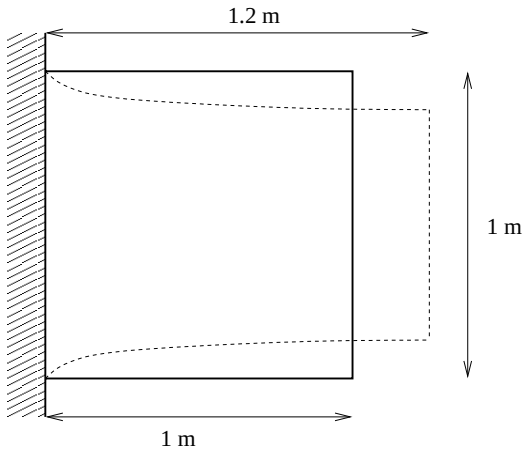

Figure 3.5: Geometry of the two–dimensional Neohookean block example.

3.5.1 Two–dimensional Neohookean block

Our first example concerns a square block 1 m in size, fixed on one side and traction-free on the remaining three sides, released from rest from a stretched configuration, Figure 3.5.1. The block is free of body forces. The material is a compressible Neohookean solid characterized by a strain-energy density of the form (3.8). The values of the material constants used in calculations are $\lambda_0 = 93$ GPa, $\mu_0 = 10$ GPa, and $\rho_0 = 7800$ kg/m^3. The initial stretch applied to the block is 1.2. The finite-element mesh contains a distribution of element sizes in order to have a corresponding distribution of elemental time steps. The mesh is composed of 380 quadratic six-noded triangular elements and 821 nodes.

Table 3.1: Neohookean block example. Number of elemental updates after 10 ms of simulation.

	AVI	Newmark
Maximum	1,374,413	1,380,000
Minimum	42,759	1,380,000
Total in the mesh	302,000,000	524,400,000

A sequence of snapshots of the AVI solution is shown in Figure 3.6. In addition, Figure 3.7 shows a comparison of the AVI solution and a baseline solution obtained using Newmark's second-order explicit algorithm (cf, e.g., Hughes [1987]). A first noteworthy feature of the AVI solution is that, despite its asynchronous character, it advances smoothly in time without ostensible jerkiness or vacillation. The AVI and Newmark solutions appear to remain in lockstep over long runs and to be of comparable quality, Figure 3.7.

The main advantage of the AVI is illustrated in Figure 3.8, which depicts the number of updates

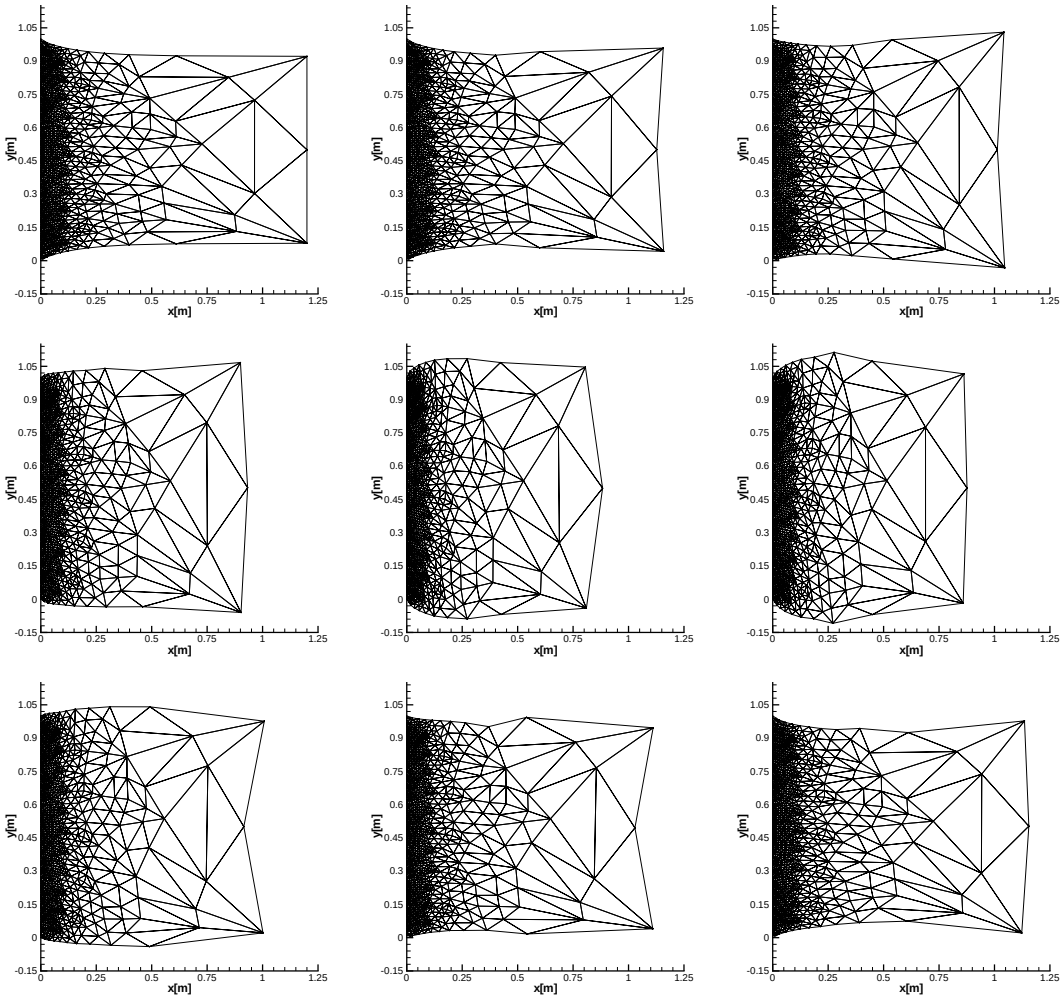

Figure 3.6: Neohookean block example. Snapshots of the deformed shape of the block at intervals of 2×10^{-4}s. Time increases from left to right and from top to bottom of the figure.

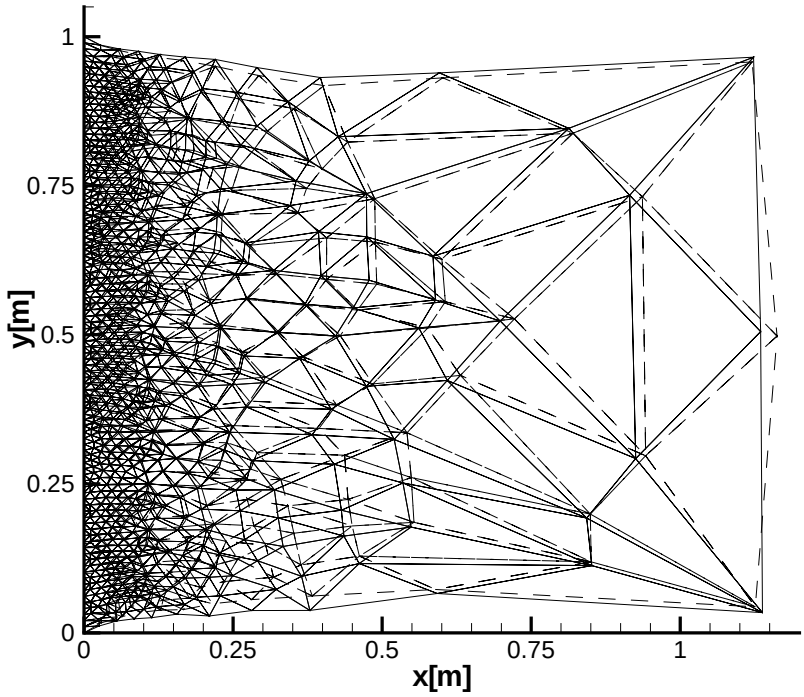

Figure 3.7: Neohookean block example. Comparison of the deformed configurations at $t = 16$ ms computed using Newmark's second-order explicit algorithm (dashed lines) and the AVI (solid lines). The time corresponds to 2,208,000 Newmark steps, or 8 complete oscillation cycles.

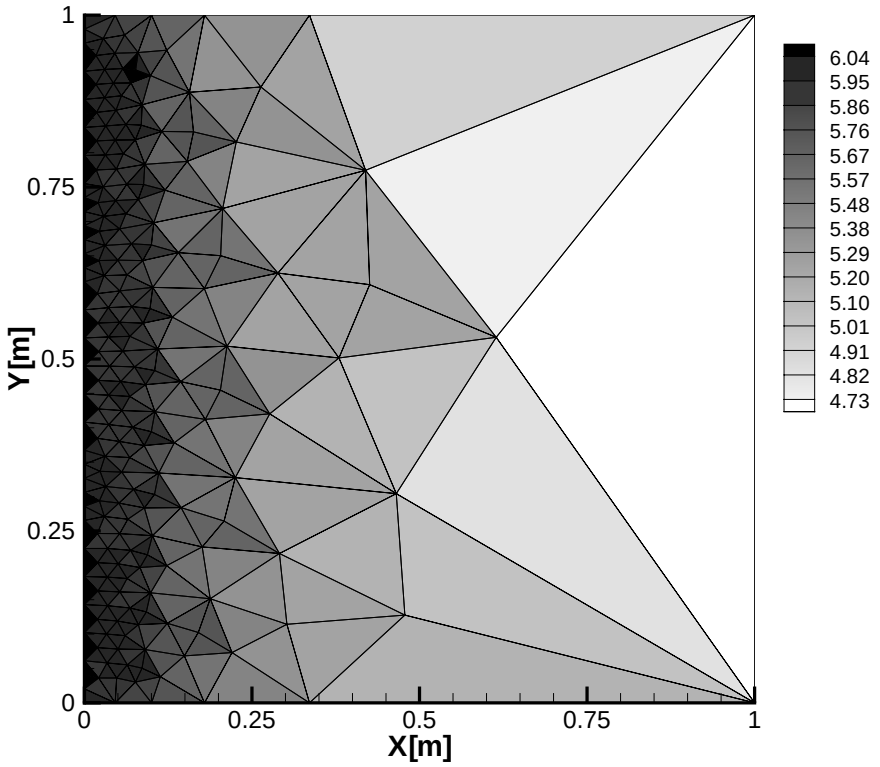

Figure 3.8: Neohookean block example. Contour plot of the $\log_{10}$ of the number of times each element is updated by the AVI after 10 ms of simulation.

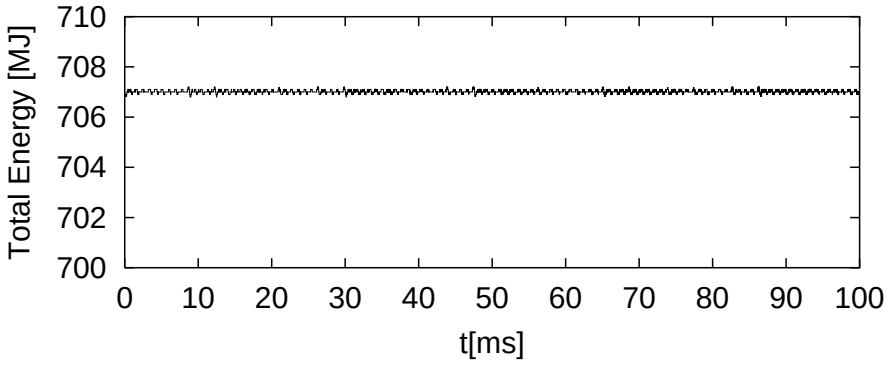

Figure 3.9: Neohookean block example. Total energy as a function of time as computed by the AVI.

in each of the elements of the mesh. As is evident from the figure, the large elements in the mesh are updated much less frequently than the fine elements. Some relevant statistics are collected in Table 3.1. Overall, in the present example the number of AVI updates is roughly 60% of the number of Newmark updates.

The excellent energy-conservation properties of Newmark's second-order explicit algorithm have been extensively documented in the engineering literature. In calculations, this good behavior manifests itself in the way in which the energy oscillates near the exact value, without displaying ostensible overall growth or decay. These empirical observations have some basis in theory, in as much as Newmark's second-order explicit algorithm can be shown to be symplectic (Kane et al. [2000]). This in turn renders results on the long–time energy behavior of symplectic methods applicable to Newmark's algorithm (see, e.g., Hairer and Lubich [1997] and Reich [1999]). In particular, the theory of backward error analysis establishes that, for sufficiently small time steps Δt, symplectic methods have errors of order $(\Delta t)^r$ for times up to $(\Delta t)e^{-C/(\Delta t)}$, where r is the order of the method and C is a constant.

Our numerical tests suggest that the AVI algorithm possesses excellent energy-conservation properties as well. Thus, for instance, Figure 3.9 shows the time evolution of the total energy of the block. It is remarkable that, the energy of the solid remains nearly constant throughout the calculations, up to 12,500,000 updates of the smallest element in the mesh, or 50 periods of oscillation of the block.

3.5.2 Three–dimensional L–shaped beam

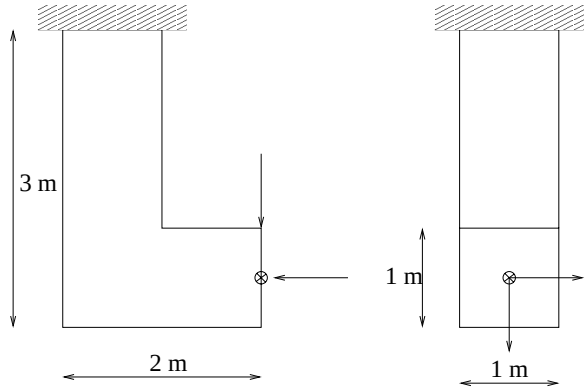

Figure 3.10: Geometry and initial loading of the L-shaped beam.

A second example concerns a three–dimensional free–standing L–shaped beam released from rest from a distorted configuration, Figure 3.10. The material is identical to that in the preceding example. The mesh comprises 621 ten-node tetrahedral elements and 1262 nodes. The local time step is again computed as a fixed fraction of the Courant time step of the element.

A sequence of snapshots of the AVI solution is shown in Figure 3.11. After 100 ms, the maximum and minimum number of elemental updates are 432,877 and 49,792, respectively, while the total number of elemental updates is 9×10^7. By way of comparison, the number of updates required by Newmark's algorithm is 27×10^7, or a factor of three larger than the AVI update count. The energy behavior of the AVI algorithm is again remarkable, as shown in Figure 3.12.

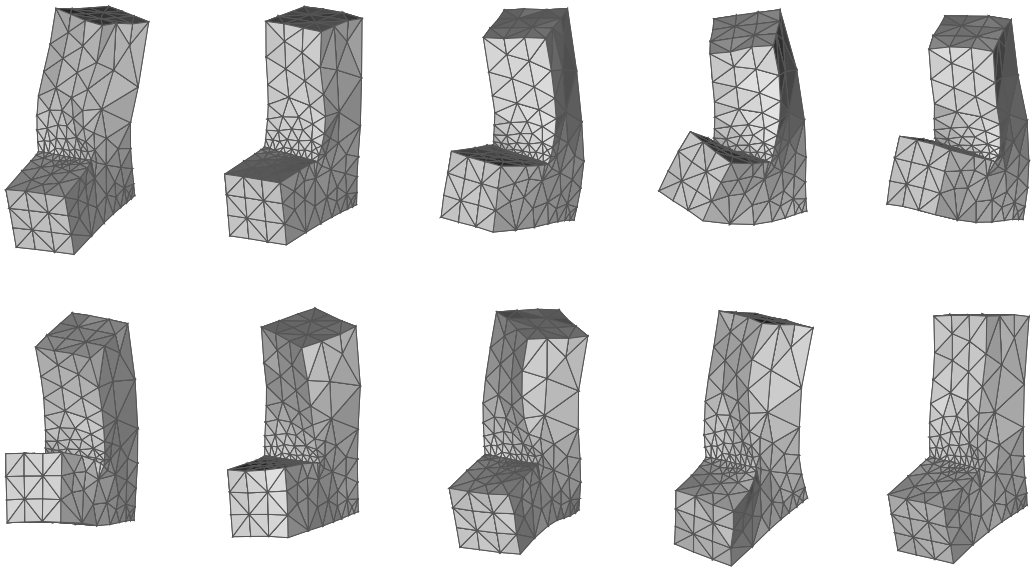

Figure 3.11: L-shaped beam example. Deformed configuration snapshots at intervals of 1 ms.

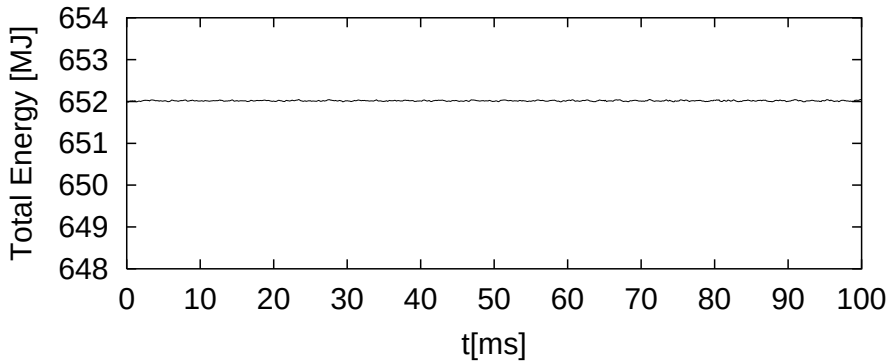

Figure 3.12: L-shaped beam example. Total energy as a function of time as computed by the AVI.

3.5.3 Dynamics of the rotor blades of an Apache AH-64 helicopter

The simulation of the dynamics of rotor blades and similar systems has long been a challenge and a test-bed for time-integration algorithms for structural dynamics (Borri [1986]; Friedmann [1990]; Sheng et al. [1998]; Armero and Romero [2001a,b]; Bottasso and Bauchau [2001]). The

slender geometry of the blades renders the system prone to dynamic instability, and the need to compute accurate solutions for long periods of time, to conserve linear and angular momentum, and to accurately distribute the energy across the frequency spectrum place stringent tests on time-integration methods.

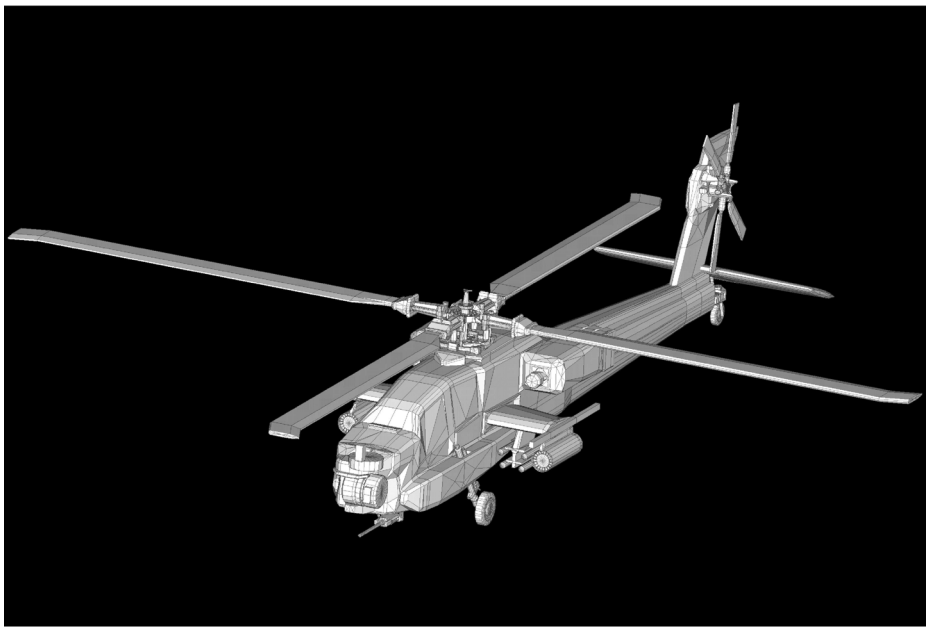

Figure 3.13: Apache AH-64 helicopter

The blade has a span of 7.2 m, a chord of 533 mm and a maximum thickness of 40 mm. The three–dimensional mesh of the blade is shown in Figure 3.15, and a photograph of a true sample of the cross-section of the blade is displayed in Figure 3.14. To test the behavior of the algorithm we replaced the complex composite structure of the blade by a homogeneous solid one. The mesh consists of 2089 ten-noded tetrahedral elements and 4420 nodes. The original geometry of the hub of the rotor, as shown in Figure 3.13, was replaced by a simple straight joint. The blades comprise 5 steel spars reinforced with glass fiber. However, for this example we simply replace the hollow structure by an effective homogeneous material. The strain-energy density is given by equation (3.8), which describes a Neohookean solid extended to the compressible range. The corresponding Piola stress–deformation relation is given by equation (3.9).

As the initial condition at time $t = 0$, we consider the blade in its undeformed configuration with a velocity field corresponding to an angular velocity $\omega = 40$ rad/s. Due to the absence of external forces or dissipation the energy is conserved and the center of mass does not move from its original position for all times. We classify cases according to the dimensionless angular velocity

$$\hat{\omega} = \frac{\omega L^2}{cw},$$

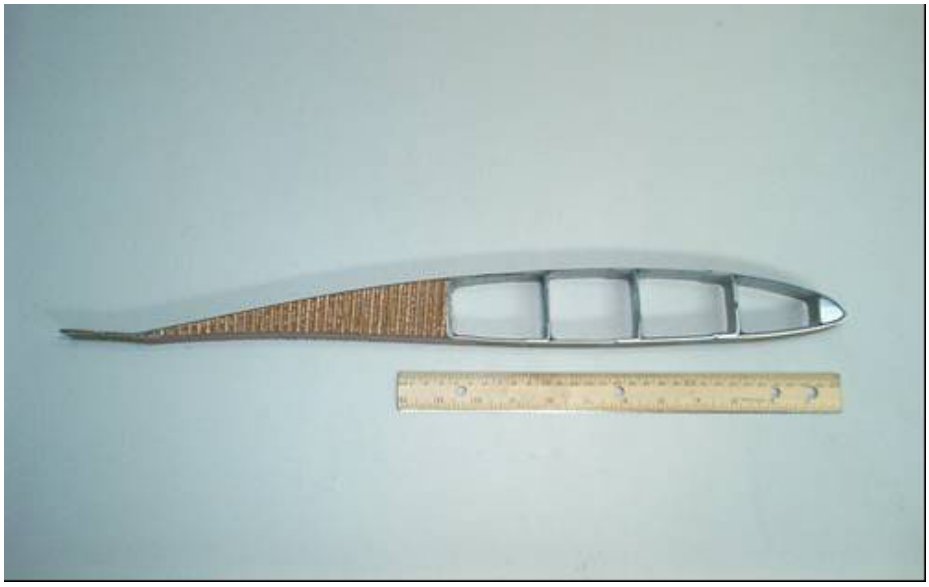

Figure 3.14: Cross section of the blade. For the example, the complex composite structure has been replaced by a homogeneous solid one.

where ω is the nominal angular velocity of the blade, L its span, w is the chord of the blade, and c is a nominal dilatational wave speed of the material computed with (3.60).

We proceed to report three test cases which illustrate the performance and properties of the AVIs. The first case consists of a homogeneous blade with material constants $\rho_0 = 250$ kg/m^3, $\lambda_0 = 0.98$ GPa and $\mu_0 = 0.98$ GPa, and, correspondingly, $\hat{\omega} = 1.13$. For this choice of parameters the computed trajectory is close to a rigid rotation, Figure 3.16, and remains stable both for short (Figure 3.16(a)) and long (Figure 3.16(b)) times.

The second case consists of a homogeneous blade with material constants $\rho_0 = 2500$ kg/m^3, $\lambda_0 = 4$ GPa and $\mu_0 = 4$ GPa, and, correspondingly, $\hat{\omega} = 1.78$. Moderately large amplitude oscillations, including spanwise torsional modes, develop during the initial transient, Figure 3.17(a). Remarkably, after this transient the blade settles down to a fairly stable shape and rotates almost rigidly.

Finally we consider a two–material blade. The central joint consists of a stiff material with constants $\rho_0 = 4500$ kg/m^3, $\lambda_0 = 3$ GPa and $\mu_0 = 0.75$ GPa, while the remainder of the blade is composed of a softer material with constants $\rho_0 = 250$ kg/m^3, $\lambda_0 = 0.1$ GPa and $\mu_0 = 0.025$ GPa. The contrast between the dilatational wave speeds of the two materials, and therefore between the stable time steps for elements of the same size in the two different regions, is 1.3. The value of the dimensionless angular velocity relative to the softer material is $\hat{\omega} = 5.02$. The initial transient is characterized by very large-amplitude oscillations in the blade, Figure 3.18(a), while the central joint remains essentially rigid. As in the previous case, after this transient the blade settles down to a stable nearly-rigid orbit.

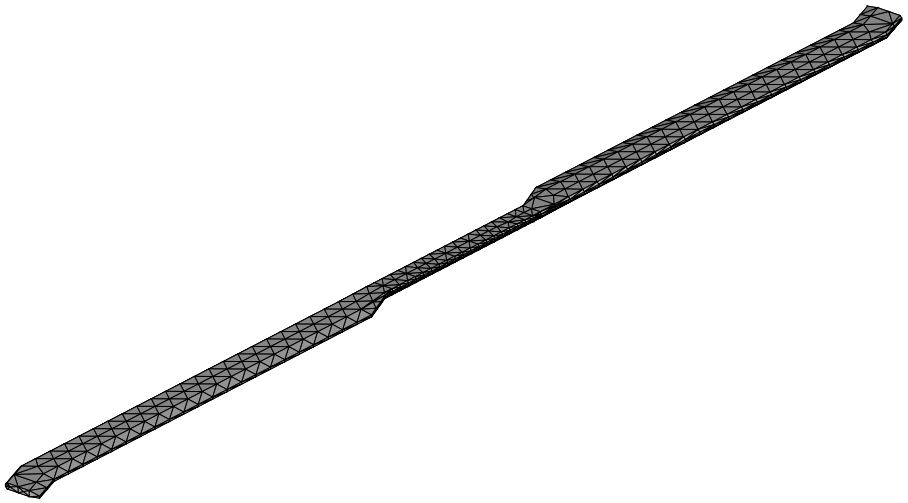

Figure 3.15: Mesh of the blade. It consists of 2089 ten-noded tetrahedral elements and 4420 nodes.

A noteworthy attribute of the solutions is that the center of mass of the blade does not move, which is a consequence of the conservation of linear momentum by the algorithm. The period of rotation for long times is of particular interest. A perfectly rigid blade would rotate once every 0.157 s. However, a flexible blade increases its span under the action of the inertia forces induced by the rotatory motion, and its angular velocity slows down in order to conserve the total angular momentum. This effect is indeed observed in the simulations, as shown in Table 3.2, and is a consequence of angular momentum conservation.

Case	$\hat{\omega}$	Period [s]
1	1.13	0.1575 ± 0.0005
2	1.78	0.1595 ± 0.0005
3	5.02	0.1845 ± 0.0005

Table 3.2: Period of rotation of the blade for long times. As the value of $\hat{\omega}$ grows, the blade deforms more increasing its span, and therefore its moment of inertia, to accommodate the centrifugal forces. Since the discrete angular momentum is conserved, the period of rotation should grow accordingly.

A measure of performance of the AVIs is shown in Figure 3.19, which depicts the number of updates in each of the elements of the mesh for the third numerical example described above. As is evident from the figure, the larger elements in the mesh are updated much less frequently than the finer elements. In particular, a small number of slivers are updated very frequently, as required by their small Courant limit. Also, the elements in the central joint, made of a stiffer material, are updated more often than the more flexible elements in the blade.

Case	$\hat{\omega}$	Final time [s]	Maximum	Minimum	Total	Speed-Up
1	1.13	7.849	266×10^6	14×10^6	8.7×10^{10}	6.37
2	1.78	15.015	325×10^6	17×10^6	42.6×10^{10}	6.37
3	5.02	27.439	235×10^6	12×10^6	8.4×10^{10}	5.80

Table 3.3: Maximum and minimum number of elemental updates for a single element at the final time. The total column shows the sum of the number of elemental updates in the whole mesh at the final time. In contrast, traditional time stepping algorithms would have advanced with the same number of updates on each element, which is equal to the value in the Maximum column. The ratio between the total number of updates in the whole mesh in these two cases is shown in the Speed-up column, a direct measure of the cost saving features of AVI.

The relevant statistics for this case are collected in Table 3.3. Overall, in the present example the number of AVI updates is roughly 15% of the number of updates required by explicit Newmark at constant time step. It should be carefully noted, however, that in the example under consideration as well as in the previous ones, the vast majority of the elements have similar sizes and aspect ratios, differing only by at most one or two orders of magnitude. It is easy to set up examples in which the update count of the constant time step algorithm bears an arbitrarily large ratio to the update count of the AVI. A case which arises in practice with some frequency concerns a roughly uniform triangulation of the domain which contains a small number of high aspect-ratio elements. The presence of a single bad element suffices to drive down the critical time step for explicit integration to an arbitrarily small value. This problem often besets explicit dynamics, especially in three dimensions where bad elements, or *slivers*, are difficult to eliminate entirely. The AVI algorithm effectively sidesteps this difficulty, as bad elements drive down their own times steps only, and not the time steps of the remaining elements in the mesh. In this manner, the overall calculation is shielded from the tyranny of the errant few.

The remarkable energy behavior is also observed in these simulations. Figure 3.20 shows the time evolution of the total energy of the blade in the third case. Again, the energy remains nearly constant throughout the calculations, which entail 234×10^6 updates of the smallest element in the mesh, or approximately 150 revolutions of the blade, despite of the dynamically unstable initial transient. The energy behavior is equally good in the remaining numerical examples.

3.5.4 Shock-loaded thermoelastic materials and high-explosive detonation waves

Perhaps the class of problems for which AVIs are most ideally suited are those involving a highly graded spatial distribution of timescales, which may arise not only from the spatial discretization but also from different physical processes being considered. The propagation of a high-explosive

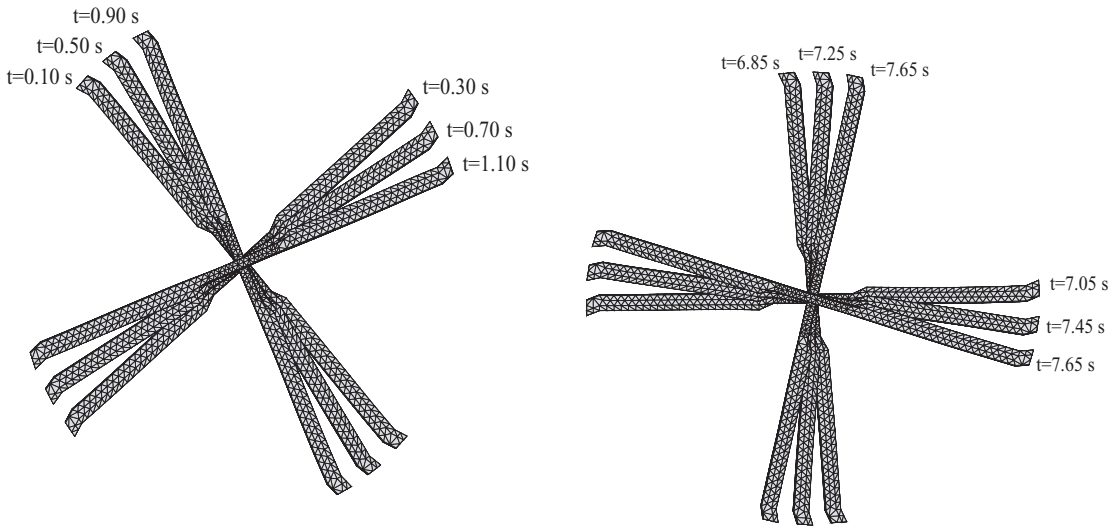

(a) Initial steps

(b) Final steps

Figure 3.16: Evolution of the blade for the first and most rigid case. The motion of the blade is essentially that of a rigid body. The center of mass does not move, a consequence of the discrete linear momentum conservation, and the period of the blade is very close to the one of a completely rigid blade, since the spanwise elongation is negligible. The final snapshots correspond to approximately 266 million updates of the smallest element in the mesh.

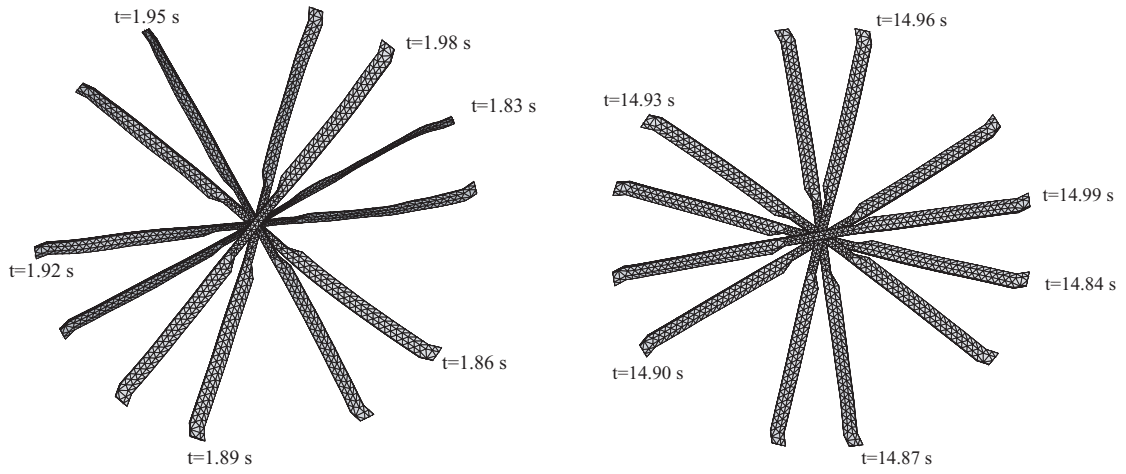

(a) Initial Steps (b) Final Steps

Figure 3.17: Evolution of the blade for the second case. During the initial phases of the motion, some fairly large deflections, including torsion along the spanwise direction, occur. However, after a relatively long time the blade rotates with an almost fixed shape. The period of rotation has changed slightly with respect to a rigid blade, since there is a non-negligible spanwise elongation inducing a change in the corresponding moment of inertia. The final snapshots correspond to approximately 325 million updates of the smallest element in the mesh.

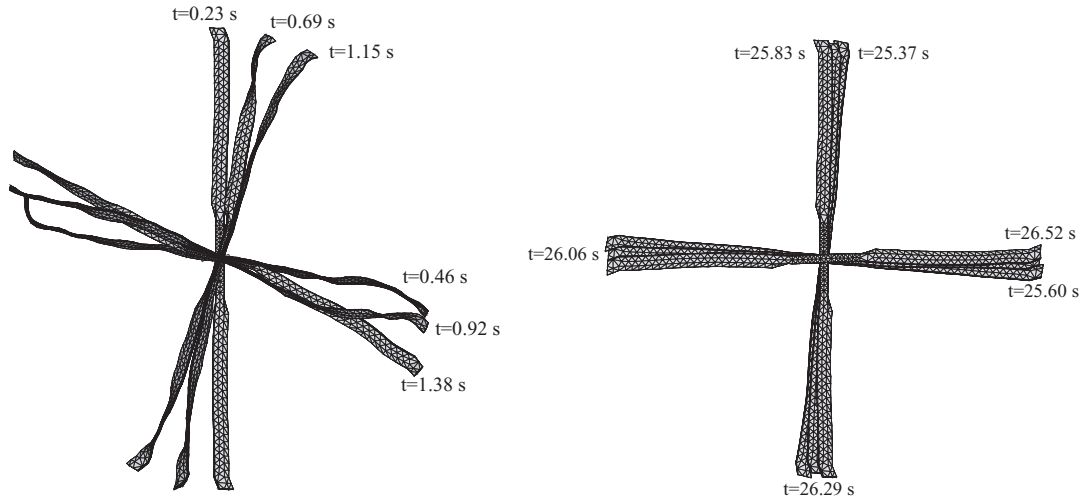

(a) Initial steps (b) Final steps

Figure 3.18: Evolution of the blade for the third and softest case. During the initial phases of the motion, the blade behaves as a very flexible strip. Surprisingly, after a relatively long time the blade settles to rotate with small amplitude oscillation close to an almost fixed shape. The period of rotation with respect to a rigid blade has changed considerably, since the spanwise elongation is large. The final snapshots correspond to approximately 234 million updates of the smallest element in the mesh.

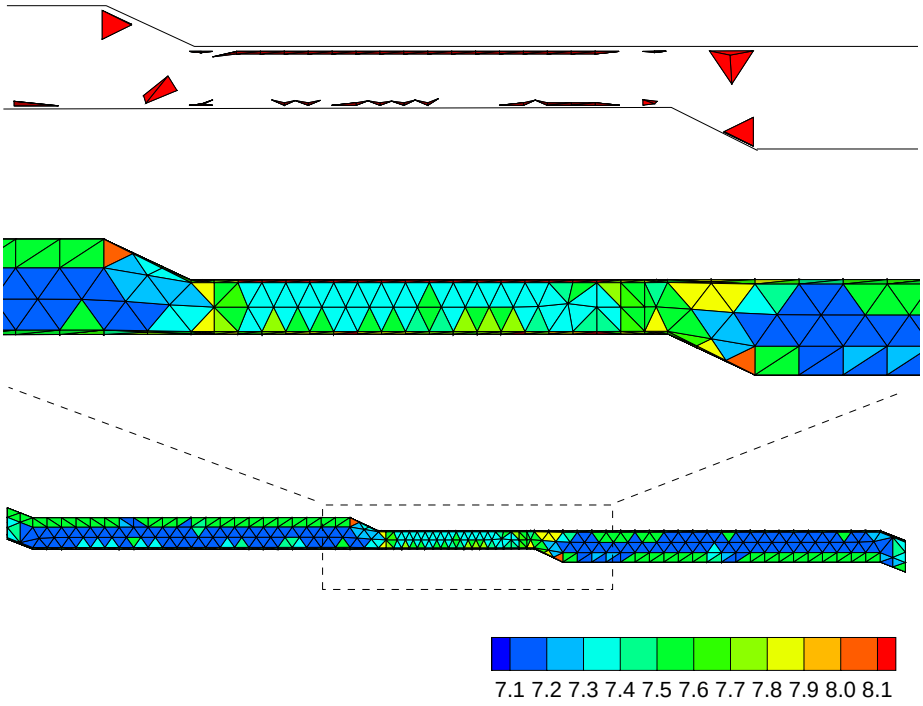

Figure 3.19: Contour plot of the $\log_{10}$ of the number of times each element was updated by the AVI after 27.439 s of simulation of case 3, in which inertial forces prevail. The picture on the middle shows an enlargement of the central part of the blade, which is made out of a stiffer material than the rest. The abrupt change in the number of elemental updates between the two regions is noteworthy. Additionally, the picture on the top shows only those few elements updated more than 10^8 times. These elements or slivers would drive the whole computation down for a constant time step algorithm, while AVI circumvents this difficulty gracefully.

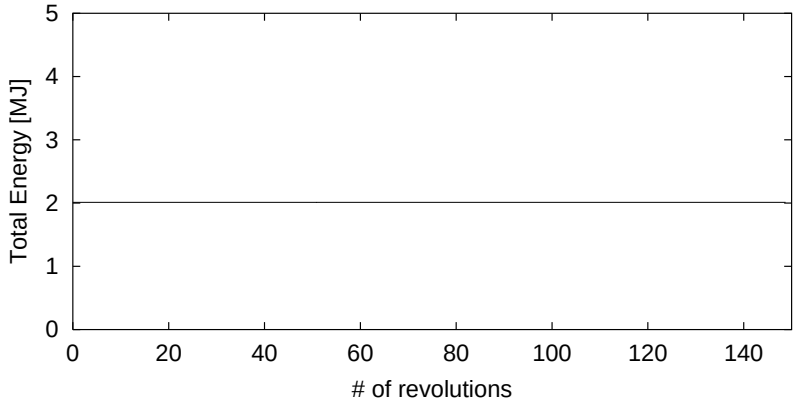

Figure 3.20: Evolution of the total energy in the blade as a function of the number of revolutions of the blade, for the third and softest case. Remarkably, the energy remains nearly constant even after the smallest element in the mesh has been updated more than 200 million times, at the end of the horizontal axis.

detonation wave is one such example. In this case there are competing timescales, a faster one associated with the chemical reaction driving the detonation, and a generally slower one associated with the propagation of elastic waves. The detonation front is usually highly localized in space, giving rise to the aforementioned spatial distribution of timescales. Also, the detonation front propagates at supersonic speeds through the material, shocking it as it advances. The strong shock preceding the detonation introduces its own time and length scale, determined largely by the viscosity of the material. Consequently, the simulation of shock-loaded thermoelastic materials, not necessarily high-explosive ones, can also take full advantage of AVIs. These two problems are considered next, after the statement of the energy balance equation and a brief discussion on shock-capturing algorithms.

3.5.4.1 Internal energy balance equation

In addition to the momentum balance equation, thermoelastic or high-explosive materials must also satisfy the internal energy balance. The local form of energy balance is

$$\rho_0 \frac{\partial U}{\partial t} + \frac{\partial H_I}{\partial X_I} = P_i{}^I \frac{\partial \dot{\varphi}^i}{\partial X^I} + \rho_0 R, \tag{3.61}$$

where U is the internal energy per unit mass, H is the heat flux per unit of undeformed area, and R is the heat source rate per unit mass. For simplicity, in the calculations presented subsequently we assume adiabatic conditions and, consequently, the heat flux and the heat sources are presumed negligible and drop out of the energy equation (3.61). Under these conditions, the evolution of the internal energy of the material is numerically tracked through a staggered procedure with the mechanical equations (see, e.g., Lew et al. [2001]). For element K at time t_K^{j+1} the update of the internal energy is performed just after the mechanical update as

$$\rho_0 U_K^{j+1} = \rho_0 U_K^j + P_K^{j+1} \cdot \left(F_K^{j+1} - F_K^j \right), \tag{3.62}$$

where the scalar product between two tensors is defined as $A \cdot B = A_i{}^I B^i{}_I$. The description of the staggered procedure is completed in the next section.

3.5.4.2 Thermoelastic materials

For a thermoelastic material it holds that (see, e.g., Marsden and Hughes [1994])

$$\left(P^e\right)_i{}^I = \frac{\partial A(F,T)}{\partial F^i_{\ I}}, \tag{3.63}$$

where T is the temperature and A is the Helmholtz free-energy per unit undeformed volume. The internal energy and the Helmholtz free-energy satisfy

$$\rho_0 U = A + \rho_0 T S, \tag{3.64}$$

where S is the entropy per unit mass. Equation (3.63) generalizes to thermoelastic materials the constitutive equation (3.5).

We must mention at this point that Hamilton's principle cannot be applied for thermoelastic materials. In this case, both the elastic and viscous stresses are included as forcing terms in the Lagrange-D'alembert principle.

Numerically, we compute the elastic stresses for element K at time t_K^{j+1} as

$$(P^e)_K^{j+1} = \frac{\partial A(A,T)}{\partial F}\Big|_{(F_K^{j+1}, T_K^j)}. \tag{3.65}$$

This completes the description of the staggered procedure to track the internal energy evolution, initiated in section 3.5.4.1.

3.5.4.3 Artificial viscosity

The numerical simulation of problems involving the propagation of shock-discontinuities in inviscid fluids or solids would require the application of proper boundary conditions on each side of the discontinuity surface, where the solution is smooth, to overcome the singularity. The correct boundary conditions are provided by the Rankine-Hugoniot jump conditions (see, e.g., Thopmson [1984]), but given that the shock position is changing in time, it is rather difficult to use this approach as part of a numerical method. On the other hand it is known that the presence of dissipative effects in the material, such as viscosity, smears the shock from a perfect discontinuity to acquire a smooth shape, and it is very often of interest to simulate flows where viscous effects are relevant.

The principal aim of artificial viscosity schemes is to enable the simulation of strong shocks of thickness so small that cannot possibly be resolved by the grid. The addition of an artificial viscosity, as first proposed in Neumann and Richtmyer [1950], has the intended effect of spreading the shock front over several grid points without affecting key aspects of the shock dynamics such as the shock speed, and without the introduction of artifacts such as spurious oscillations in the shock profile. The ancillary viscosity introduced into the calculations is strictly a numerical device which depends on the grid size and must vanish in the limit of a vanishing grid size.

In Lew et al. [2001] we presented a Lagrangian artificial viscosity scheme whose salient attributes are as follows: it is formulated within a general finite-deformation framework; it satisfies material-frame indifference exactly; and it is applicable to high-order tetrahedral elements and unstructured

meshes. The scheme shares a number of features in common with–but also differs in significant respects from–existing schemes. For instance, the artificial viscosity proposed in Lew et al. [2001] is deviatoric, in contrast with Wilkin's artificial viscosity (see Wilkins [1980]), which is volumetric. We refer to Lew et al. [2001] for further details and selected examples.

The aforementioned artificial viscosity scheme which we shall use in the forthcoming examples is formulated as follows. We assume that the viscosity coefficient comprises two terms,

$$\eta_h = \eta + \Delta\eta, \tag{3.66}$$

where η is the physical viscosity coefficient of the material and $\Delta\eta$ is the added artificial viscosity. The artificial viscosity coefficient $\Delta\eta$ at a given Gauss quadrature point of the mesh in assumed to be of the form

$$\Delta\eta = \begin{cases} \max\left(0, -\frac{3}{4}\ell\rho(c_1\Delta u - c_L a) - \eta\right) & \Delta u < 0 \\ 0 & \Delta u \geq 0 \end{cases}, \tag{3.67}$$

where ℓ is a measure of the element size and Δu is a measure of the velocity jump across the element; c_1 and c_L are coefficients; a is a characteristic sound speed of the material; and $\rho = \rho_0/J$ is the mass density per unit deformed volume. A widely used procedure for calibrating c_1 and c_L attributed to Christensen is discussed by Benson [1992].

In a one–dimensional problem the values of Δu and ℓ simply correspond to the jump in velocity across an element and the element size in the deformed configuration. In a multidimensional simulation Δu and ℓ must be defined in a way that renders the artificial viscosity formulation material frame indifferent. A simple way to satisfy this requirement is to express the value of Δu as a function of the Jacobian of the deformation, or its time derivatives. This suggests writing

$$\Delta u = \ell \frac{\partial \log J}{\partial t}, \tag{3.68}$$

where

$$\ell = (J\, d!|K|)^{1/d}, \tag{3.69}$$

where d is the dimension of space and $|K|$ is the volume of element K in its reference configuration. Equations (3.68) and (3.69) are evaluated at every Gauss quadrature point in the mesh. We further approximate the velocity jump as

$$\Delta u_{n+1} = \ell_{n+1} \frac{\log J_{n+1} - \log J_n}{\Delta t}. \tag{3.70}$$

More general forms of the artificial viscosity can be formulated in terms of the invariants of the right Cauchy-Green tensor and their time derivatives.

The proposed artificial viscosity shares features with a number of existing formulations. Thus, in Wilkins [1980] the two–dimensional artificial viscosity is volumetric and generalizes the original one–dimensional model proposed in Neumann and Richtmyer [1950]. Lapidus formulated a third-order artificial deviatoric viscosity (see Lapidus [1967]), which, however, fails to be tensorial and material-frame indifferent. The present model follows Wilkins [1980] as regards the form of the viscosity coefficient, but the present artificial viscosity is deviatoric. In one dimension, the present model exactly coincides with the formulation in Wilkins [1980].

As already mentioned, Benson [1992] discussed a procedure for determining the c_1 and c_L. Briefly, the method in Benson [1992] is based on the fact that the Rankine-Hugoniot jump conditions define an implicit relation $D(\Delta u)$ between the shock speed and the jump in velocity, which is usually well approximated by a linear fit of the form

$$D = c_0 + s_1 \Delta u \tag{3.71}$$

for a wide variety of materials for each set of initial conditions, where c_0 and s_1 are adjustable parameters. By replacing this relation into the Rankine-Hugoniot linear momentum jump condition for a steady shock, namely,

$$\Delta p = \rho D \Delta u \tag{3.72}$$

a quadratic relation in Δu is obtained. In this relation, ρ represents the unshocked density. By regarding the artificial viscosity scheme as an approximate Riemann solver, the following relations for c_1 and c_L are obtained:

$$\begin{aligned} c_1 &\approx s_1 \\ c_L &\approx c_0/a. \end{aligned} \tag{3.73}$$

Our experience suggests that these values tend to be overdiffusive, and tend to perform better for strong shocks than for weak shocks. For the latter shocks the coefficients (3.73) usually smear the shock over more elements than strictly necessary and exacerbate overheating effects. The value of c_1 may be expected to remain close to 1, since for strong shocks it follows directly from the Rankine-Hugoniot jump conditions that $\Delta p \sim \rho(\Delta u)^2$. The value of c_L is typically in the range of 0.1 to 1.

3.5.4.4 Plate impact experiment on tantalum

We consider the problem of the propagation of a plane wave through the thickness of an infinite plate as the result of the impact by a striker plate. The impact results in a velocity $V_0 = 2000$ m/s prescribed on one of the surfaces of the plate. In view of the symmetry of the problem, we restrict

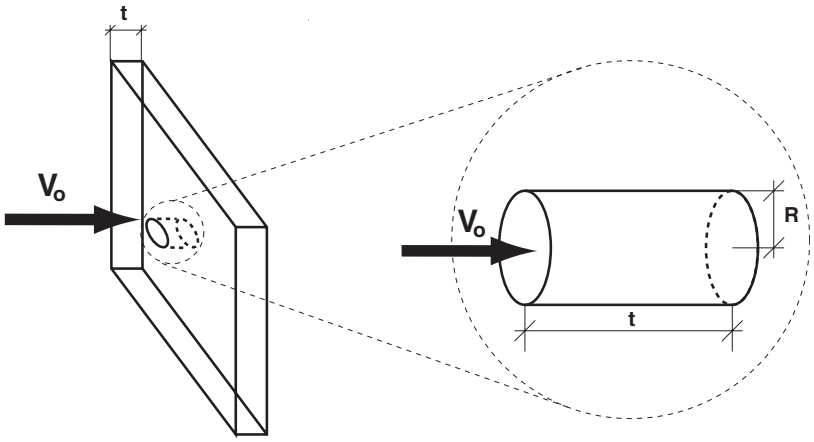

Figure 3.21: Schematic of plate impact problem

the analysis to a cylindrical core of material spanning the thickness of the plate, Figure 3.21. The cylinder has a radius $R = 0.02\,m$ and a length equal to the thickness of the plate, $t = 0.1\,m$. In order to replicate the prevailing uniaxial strain mode of deformation, the external cylindrical surface is allowed to move in the cylinder's axial direction only. The material is assumed to obey Vinet's equation of state as fitted to first principle calculations for tantalum by Cohen at high pressures Cohen and Gülseren [2000]. The resulting internal energy per unit mass is (SI units)

$$\begin{aligned} U(T,v) = & \\ & -2.218\times10^{11} + e^{-4.68(v/v_0)^{1/3}}\left(1.813\times10^{9} - 2.306\times10^{9}\,(v/v_0)^{1/3}\right) + \\ & +3RT - \sum_{i=2}^{3}\sum_{j=1}^{4}(i-1)A_{ij}T^{i}\,(v/v_0)^{j-1}\,, \end{aligned} \tag{3.74}$$

where T is the absolute temperature, v the specific volume per unit mass, $v_0 = 5.959\,m^3Kg^{-1}$ is the specific volume at zero pressure and temperature and A_{ij} is a matrix of constants. The entropy $S(T,v)$ per unit mass is given by (SI units)

$$S(T,v) = 3R + 3R\log(T) - \sum_{i=1}^{3}\sum_{j=1}^{4} iA_{ij}T^{i-1}\,(v/v_0)^{j-1}\,, \tag{3.75}$$

where $R = 1.5045\,J/(Kg\,K)$ is the gas constant for tantalum. The matrix A_{ij} is identified as (SI units)

$$A = \begin{bmatrix} 9.212\times10^{2} & -2.007\times10^{2} & 7.640 & -3.574\times10 \\ 1.243\times10^{-2} & -3.896\times10^{-2} & 2.519\times10^{-2} & -9.233\times10^{-4} \\ -6.506\times10^{-7} & 1.505\times10^{-7} & -7.261\times10^{-7} & -2.320\times10^{-7} \end{bmatrix}.$$

Equations (3.74) and (3.75) completely define the thermodynamic behavior of the material. In this problem, the deviatoric response of the material is neglected, and the material is assumed to be devoid of strength.

The material is also assumed to have negligible viscosity. The viscous response is provided only by the artificial viscosity, with constants $c_1 = 1.2$ and $c_L = 0.99$. The density in the reference configuration is $\rho_0 = 16550$ Kg/m^3, while the cylinder's initial temperature is 293 K.

The evolution of the system is characterized by a shock-wave traveling through the material at constant speed, with homogeneous regions both in front and behind the shock. The speed of the shock can be known beforehand by solving the corresponding Rankine-Hugoniot jump conditions. We use this *a priori* knowledge to dynamically adapt the time steps in the system to finely resolve the region surrounding the shock. After each elemental update we determine a new time step for the element under consideration by using equation (3.59). However, in this case we make f to be a function of time and the distance of the center of mass of the element to the impacted face d_{cm}, i.e.,

$$f(t, d_{cm}) = f_0 - \Delta f \exp\left[-\Big(\frac{d_{cm} - Dt}{w}\Big)^2\right], \tag{3.76}$$

where $f_0 > 0$ is some far-field value, Δf is the amplitude, D is the speed of the shock and w parametrizes the width of the region over which the time step varies. In (3.76) we have assumed that the shock at $t = 0$ is exactly at the impacted face.

In more general situations, we will not count with the valuable information provided by the Rankine-Hugoniot jump conditions, and the spatial distribution of time steps will have to be determined differently. In particular, coupling AVIs together with some Adaptive Mesh Refinement (AMR) strategy promises to be highly rewarding, providing *space–time AMR*. In particular, the refinement strategy chosen to refine the spatial mesh will automatically add time resolution as well, as indicated by equation (3.59).

For the numerical example in this section we used a mesh composed of 37801 ten-noded tetrahedral elements and 53708 nodes. In addition, we chose $f_0 = 1$, $\Delta f = 0.9$ and $w = 0.03$ m. The computed value for the shock speed is $D = 5852$ m/s. Notice that for elements away from the shock the value of the time step approaches the one given by the local Courant condition, according to equation (3.59) and the fact the $f \approx 1$ there. Even though this is a rather exceptional situation, it surely illustrates the gained flexibility provided by AVIs.

Figure 3.22 shows several snapshots of the compressed cylinder. The profiles of the axial velocity and the Jacobian on one plane containing the axis of the cylinder are shown in Figure 3.23. The shock is spread over 6 elements, which is slightly overdiffusive, but well in agreement with other artificial viscosity methods (see Lew et al. [2001]). Some degree of spurious overheating, as described in Noh [1987], can be seen near the impact surface in the plot of the Jacobian. This pathology is known

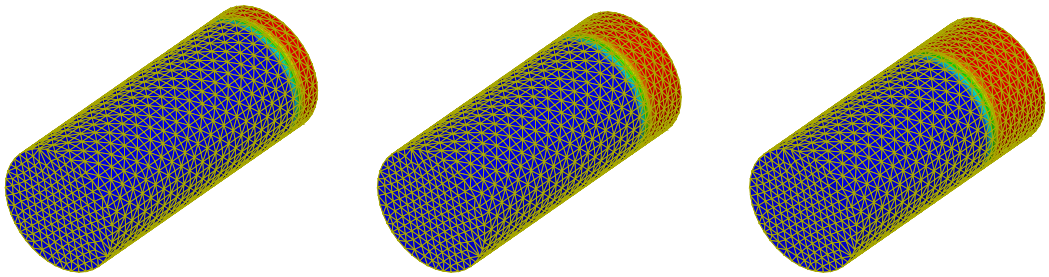

(a) t=2.1 μs (b) t=4.1 μs (c) t=6.1 μs

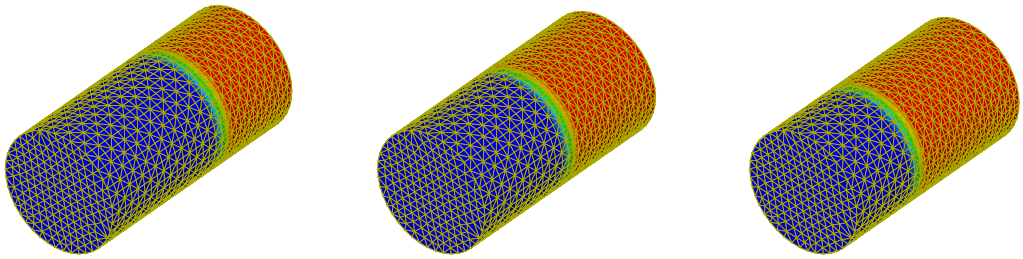

(d) t=8.1 μs (e) t=10.1 μs (f) t=12.1 μs

Figure 3.22: Snapshots of the evolution of the shock wave advancing through the cylinder. In addition to the mesh, each snapshot depicts contour plots for the axial velocity.

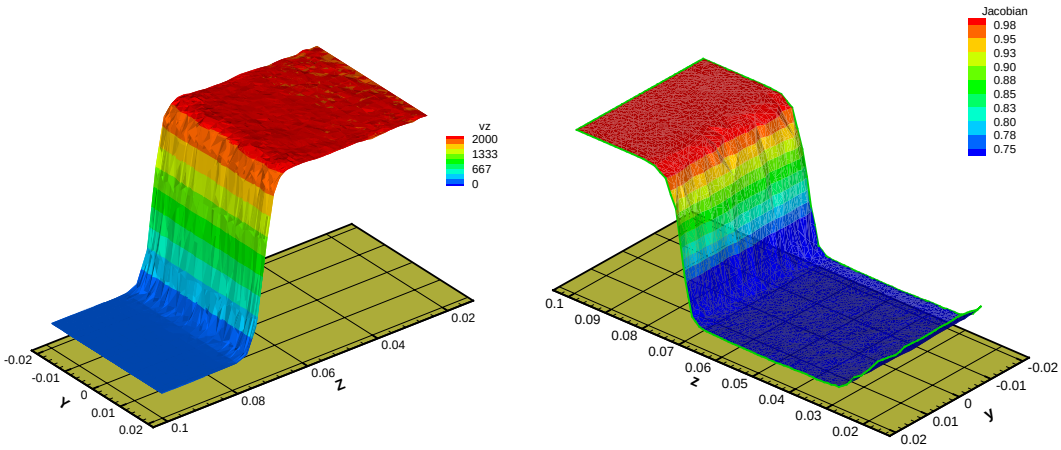

(a) Axial velocity

(b) Jacobian

Figure 3.23: Profile and contours of the axial velocity and the Jacobian of the deformation mapping, drawn at time t=12.1 μs on one of the planes that contains the cylinder axis. The shock is well captured by the artificial viscosity and spread along approximately 6 elements. The wall overheating effect is noticeable near the impact surface in the plot of the Jacobian, as is commonly observed in other artificial viscosity schemes. Even though the time step far from the shock approaches the one given by the local Courant condition, the solutions do not appear to possess any apparent instability.

to plague artificial viscosity methods generally, and can be ameliorated by the introduction of an artificial heat flux. Table 3.4 shows a comparison between the values of the pressure, specific volume and temperature behind the shock as obtained directly from the jump conditions for a steady shock and from the numerical solution. It is evident from this table that the jump conditions are well captured by the numerical solution. The evolution of the pressure in time is illustrated through a sequence of snapshots in Figure 3.24. In the same figure, the number of updates each element performed during a preset time interval is plotted. In both cases, only the values over one plane that contains the cylinder axis are drawn. The enhanced resolution provided by AVIs near the shock is reflected in the smooth pressure profiles, as well as in the values of the state variables behind the shock.

	Theoretical	Numerical
p_2 [GPa]	194.86	196 $\pm$ 2
v_2 [10^{-5} m^3/Kg]	3.953	3.94 $\pm$ 0.01
T_2 [K]	5263	5100 $\pm$200
D [m/s]	5852	5850 $\pm$50

Table 3.4: Comparison between theoretical and numerical values of pressure, specific volume, and temperature after the shock. D is the shock velocity.

Perhaps the most outstanding feature of this example is the fact that the time resolution used

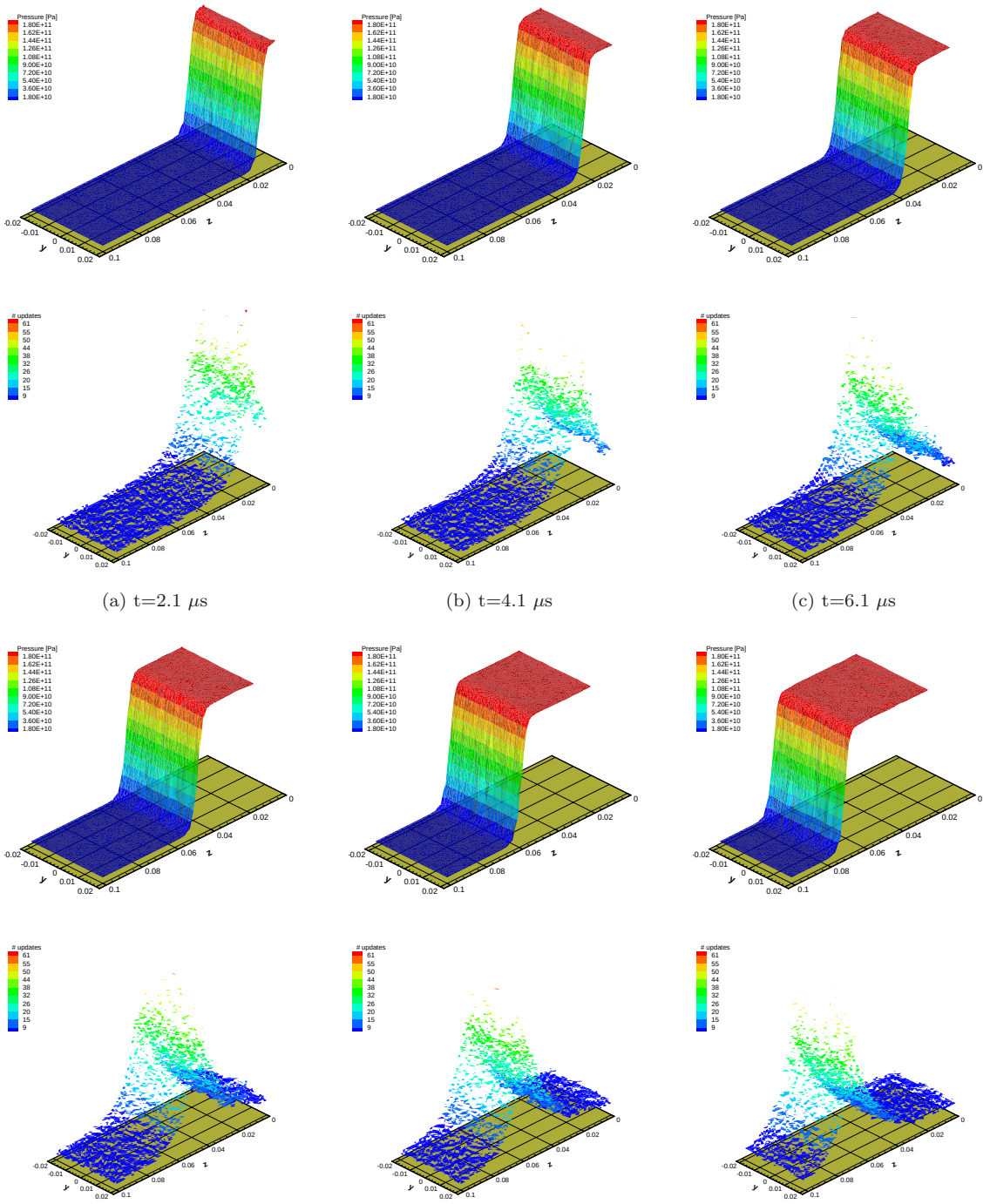

(a) t=2.1 μs (b) t=4.1 μs (c) t=6.1 μs

(d) t=8.1 μs (e) t=10.1 μs (f) t=12.1 μs

Figure 3.24: Sequence of snapshots showing the evolution of the pressure (top) and the number of time steps each element performs during a preset time interval (bottom). Both fields are drawn on a plane that contains the cylinder axis. Outside the shock region, the elemental time step is very close to that given by the Courant condition. The ratio maximum/minimum number of updates is always of the order 10, i.e., the ratio minimum/maximum elemental time step is of the order 10^{-1}.

over the shock is similar to the one that should be used in a synchronous time stepping algorithm, such as second-order explicit Newmark. Notwithstanding, AVIs enables the use of larger time steps in the regions far from the shock without seriously harming the accuracy of the solution. Most remarkably, the value of these time steps are very close to the ones given by the Courant condition. The ability of AVIs to accurately integrate the evolution of the system with minimum computational effort is notably illustrated by this example.

3.5.4.5 Plate impact experiment on a high-explosive material

Next, we consider an impact experiment on a high-explosive material, instead of tantalum. High-explosive materials are characterized by a high power or high energy release rate, without necessarily releasing a large total amount of energy. A typical timescale for the chain of chemical reactions involved in a detonation is of the order of nanoseconds, i.e., 10^{-9} s. If an average finite element in the mesh has a size of the order of milimiters, and the characteristic sound speed of the material is of the order of 10^3 m/s, the characteristic time step necessary to accurately propagate elastic waves in the simulation, according to equation (3.59), is of the order of microseconds, i.e., 10^{-6} s. On the other hand, resolving the detonation front profile requires a spatial resolution of the order of tens of nanometers, which drives the order of the time step for elastic wave propagation to the tens nanoseconds in a highly localized spatial region. Evidently, the propagation of a detonation front is a prototype multiscale problem for which AVIs are ideally suited.

The engineering material model for high-explosive considered next was proposed in Morano and Shepherd [1999]. Despite its simplicity, it contains all the essential features needed to test AVIs in coupling chemistry and mechanics, or more generally, problems involving multiphysics. For details and background material in high-explosive detonations and their numerical modeling we refer the reader to Ficket and Davis [1979] or Mader [1979].

A detonation process consists of a chemical reaction in which a number of reactants are transformed into products through a chain of chemical reactions. In its simplest form, this chain can be idealized to consist of just one–step in which the reactant transforms directly into the product. Assuming a one–step reaction mechanism, the depletion law is proposed to be

$$\frac{\partial \Lambda}{\partial t} = \begin{cases} K \left(\dfrac{p}{p_{VN}} \right)^m (1-\Lambda)^{1/2} & p > \dfrac{p_{VN}}{3} \\ \\ 0 & p \leq \dfrac{p_{VN}}{3} \end{cases}, \tag{3.77}$$

where $\Lambda \in [0,1]$ is the fraction of reactants transformed into products in a representative volume, K is the reaction rate constant, $0 \leq m \in \mathbb{R}$, p is the pressure and p_{VN} is the Von Neumann pressure Thopmson [1984]. Notice that the detonation is assumed to start once the pressure exceeds one-third

of the shock peak pressure p_{VN}.

The material is further assumed to obey a Mie-Grüneisen equation of state constructed to reproduce well the experimentally measured detonation front propagation velocity

$$p(J,U,\Lambda) = \frac{\mathcal{G}\rho_0}{J}\left[U - \Lambda Q\right] + \bar{p}(J,\Lambda), \tag{3.78}$$

where U is the internal energy per unit mass for the reactants, Q is the total energy released when a unit mass of reactants fully transforms into products, $\mathcal{G}$ is the Mie-Grüneisen coefficient, ρ_0 is a reference density and ρ_0/J is the density of the material. The function $\bar{p}(J,\Lambda)$ is defined as

$$\bar{p}(J,\Lambda) = \mathcal{G}\Lambda Q\frac{\rho_0}{J} + \begin{cases} \rho_0 c_0^2 \dfrac{(1-J)}{\left[1-s_1(1-J)\right]^2}\left[1 - \dfrac{\mathcal{G}}{2J}(1-J)\right] & J \leq 1 \\ \\ \rho_0 c_0^2\left(\dfrac{1}{J} - 1\right) & J > 1, \end{cases} \tag{3.79}$$

where c_0 and s_1 are experimentally measured material parameters. This equation of state guarantees that the relation between the jump in particle velocity across the detonation front Δu and the detonation front propagation speed D follows the experimentally measured relation (3.71). For HMX, a high-explosive, $\mathcal{G} = 0.7$, $s_1 = 1.79$, $c_0 = 3070$ m/s, $\rho_0 = 1891$ Kg/m^3 and $Q = 14.7 \times 10^6$ J/Kg (Morano and Shepherd [1999]).

As in the previous example, the material is assumed to have negligible viscosity and be devoid of strength. Notwithstanding, one of the main advantages of a Lagrangian formulation of high-explosive materials is that it is relatively easy to model its shear response, as opposed to more traditional purely hydrodynamic Eulerian descriptions.

In the following numerical example the artificial viscosity coefficients are chosen to be $c_1 = 1.79$ and $c_L = 1.0$. The reaction rate constant K is set to the value 3.5×10^9 s^{-1}, while m is chosen to be 1. The same finite element mesh of the previous example was used, composed of ten-noded tetrahedral elements with a mesh size everywhere of the order of 10^{-3} m. The material is initially at rest, with $U = 0$ J/Kg, $\Lambda = 0$ and $\rho = \rho_0$ homogenously in the material. The impact velocity was set to $V_0 = 2176.932$ m/s, which corresponds to a Chapman-Jouguet detonation front (see, e.g., Thopmson [1984]). Once more, we dynamically adapted the time step according to equation (3.76), where we chose $f_0 = 1$, $\Delta f = 0.9999$, $w = 0.03$ m and D was computed to be 9596 m/s.

A sequence of snapshots showing the deformation of the cylinder as the detonation front advances as well as the axial velocity contours is shown in Figure 3.25. In addition, a plot of the axial velocity and the Jacobian of the deformation on one plane containing the cylinder axis are shown in Figure 3.26. Even though artificial viscosity was used in the simulations, the velocity profiles show some spurious oscillations behind the shock. These oscillations stem from the fact that the reaction zone

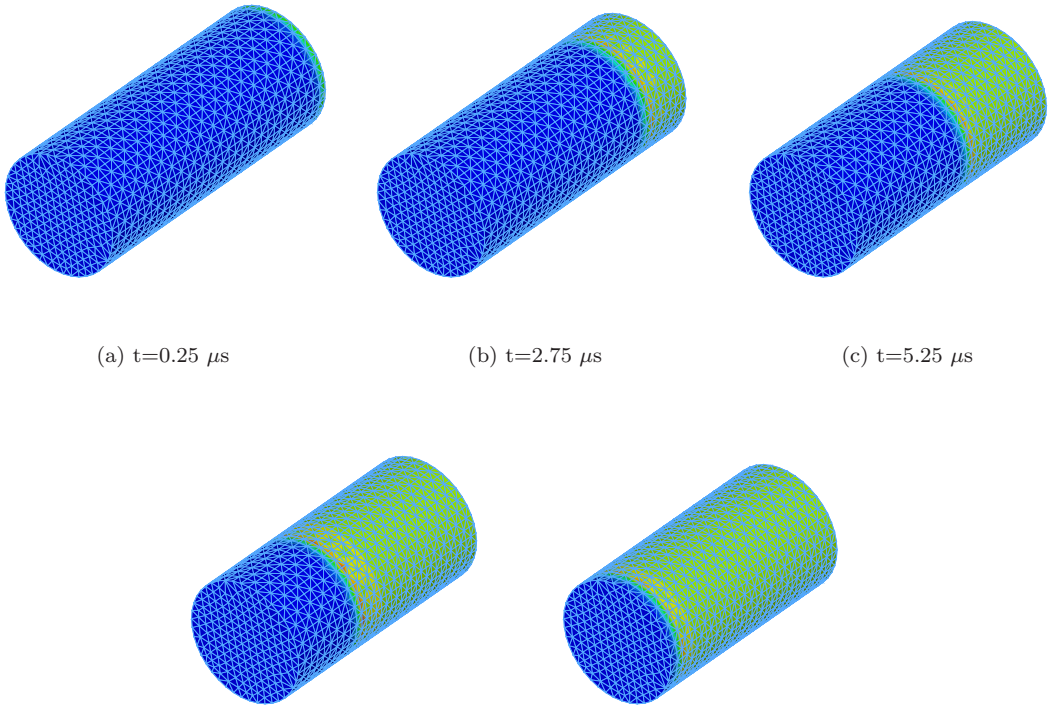

(a) t=0.25 μs (b) t=2.75 μs (c) t=5.25 μs

(d) t=7.75 μs (e) t=10.25 μs

Figure 3.25: Snapshots of the evolution of the detonation front and deformation of the cylinder. In addition to the mesh, each snapshot depicts contour plots for the axial velocity.

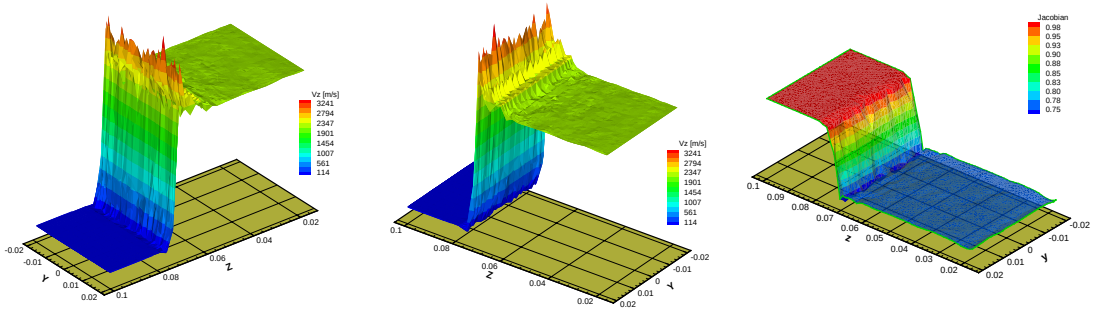

(a) Axial velocity, front view (b) Axial velocity, rear view (c) Jacobian

Figure 3.26: Profile and contours of the axial velocity and the Jacobian of the deformation mapping on one of the planes that contains the cylinder axis, at time t=7.75 μs. The irregular over- and under-shoot in the velocity is due to the fact that the mesh is too coarse to resolve the detonation profile.

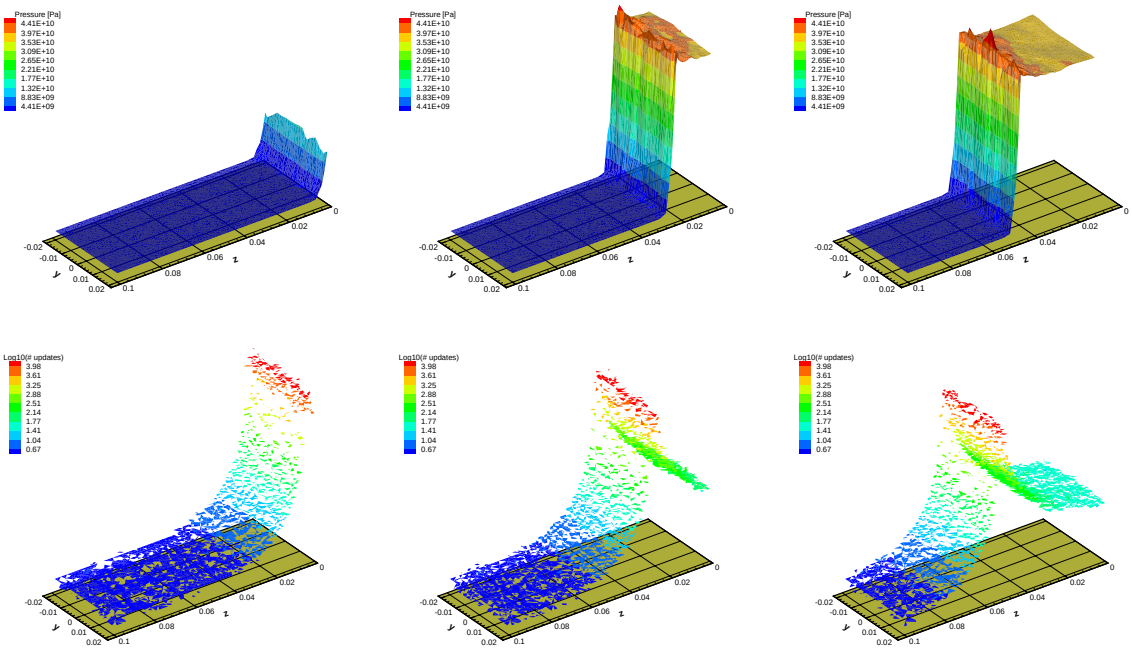

(a) t=0.165 μs (b) t=2.75 μs (c) t=5.25 μs

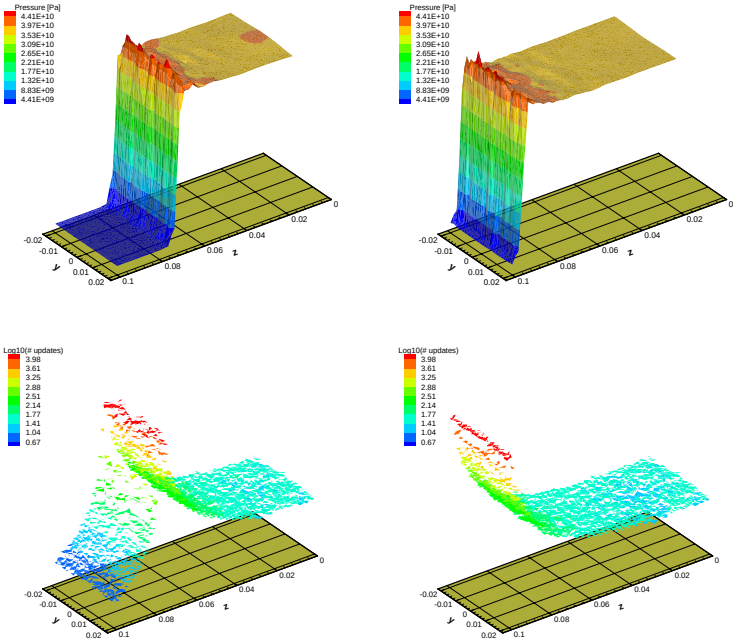

(d) t=7.75 μs (e) t=10.25 μs

Figure 3.27: Sequence of snapshots showing the evolution of the pressure (top) and the number of time steps each element performs during a preset time interval (bottom). All pictures show the values of the corresponding fields on a plane that contains the cylinder axis. Notice the logarithmic scale on the vertical axis of the number of updates each elements performs. It is remarkable that the ratio maximum/minimum number of updates is always of the order 10^4, i.e., the ratio minimum/maximum elemental time step is of the order 10^{-4}.

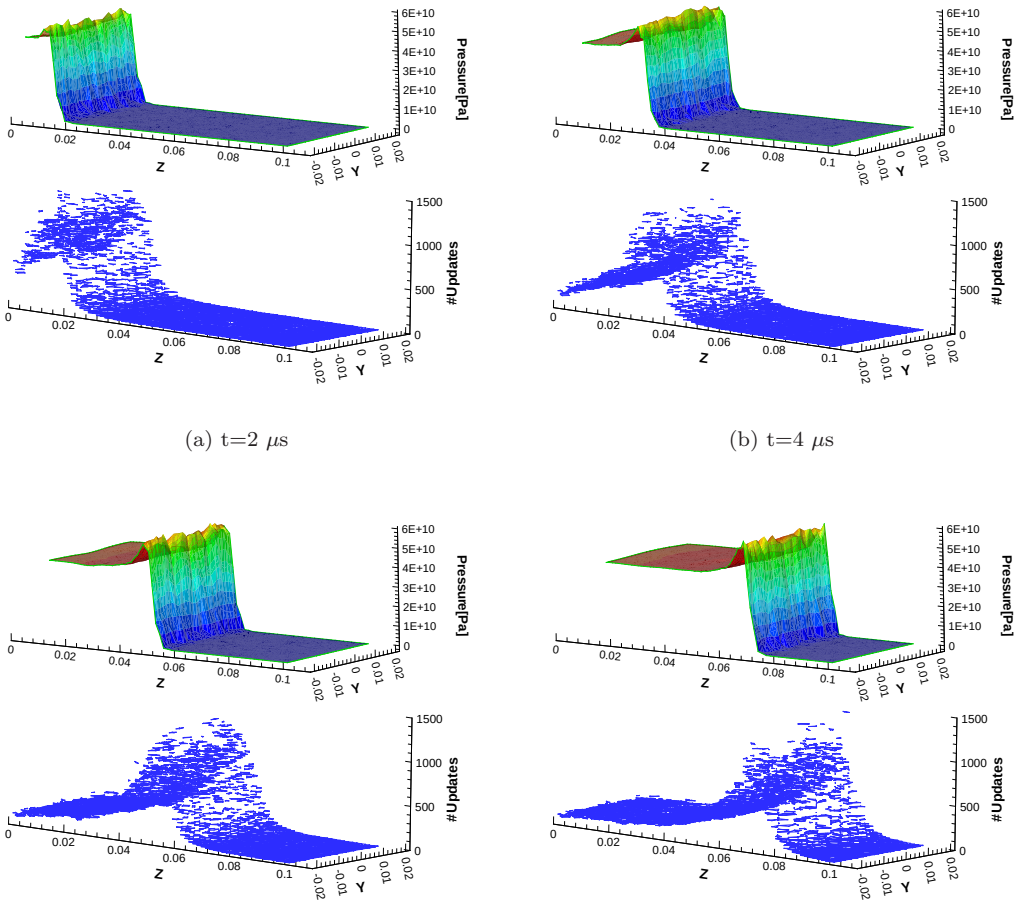

(a) t=2 μs

(b) t=4 μs

(c) t=6 μs

(d) t=8 μs

Figure 3.28: Evolution of the pressure and the number of elemental updates during a given time interval for a slower reaction, with a characteristic reaction time of 2 μs. Notice how the width of the reaction zone becomes comparable to that of the mesh size, and can therefore be resolved.

has a width of the order of a micrometer, and therefore its correct shape cannot be resolved by a mesh with milimiter-sized elements. Table 3.5 shows a comparison between the values of the state variables behind the detonation front as obtained directly from the jump conditions for a Chapman-Jouguet detonation and from the numerical solution. As before, the jump conditions are well captured, despite the fact that the detonation profile is being under-resolved. The evolution of the presssure on one plane containing the cylinder axis is shown in Figure 3.27. Additionally, the number of updates each element undergoes during a preset time interval on the same plane is included in Figure 3.27 as well. Notice how the time steps are dynamically modified to always finely solve in time the reaction zone. For comparison, Figure 3.28 shows analogous results from a simulation in which we had set $K = 2 \times 10^6$ s$^-$1 and for which the reaction zone has been resolved. In this case $m = 0$, $f_0 = 1$, $\Delta f = 0.99$ and $w = 0.03$ m.

	Theoretical	Numerical
p_2 [GPa]	39.51	39.1 ± 0.3
v_2 [10^{-3} m^3/Kg]	0.4089	0.407 ± 0.003
U_2 [MJ/Kg]	17.07	16.90 ± 0.20
D [m/s]	9596	9500±200

Table 3.5: Comparison of the theoretical and numerical predictions for the state of the material after the detonation process has finished, as well as the detonation front propagation speed.

A fair objection to raise regarding the current example is that given that for $K = 3.5 \times 10^9$ s^{-1} the material fully detonates before a sound wave can travel through any element of the mesh, one could safely uncouple the chemistry from the mechanics by hypothesizing that the element does not deform while the chemical reaction is occurring. There are, however, at least two comments to be made about it. First, it is important, especially for curved detonation fronts, to resolve the reaction zone profile. The use of AMR becomes essential to accurately integrate the solution, and, as clearly shown in this example, AVIs can gracefully handle localized regions with faster timescales. Second, realistic problems usually involve a distribution of element sizes throughout the mesh, and it becomes unclear how to automatically tell when the hypothesis of uncoupling of the mechanics and the chemistry holds. In contrast, the procedure presented here to address high-explosive detonation problems is rather general.

3.5.4.6 Contained detonation of a high-explosive material

The numerical examples involving thermoelastic materials hitherto were restricted to simple cases, suitable to assess the performance of the algorithms and establish quantitative comparisons. The next example, however, is aimed at illustrating the benefits of asynchronous integration in more complex, and perhaps more realistic, situations.

We consider a hollow, thick-walled cylinder, or canister, which contains a high-explosive material

in its interior. The length of the canister is 0.1 m, its outer diameter is 0.06 m and its wall-thickness is 0.01 m. The cylinder obeys a Neohookean constitutive relation, equation (3.9), which in the small deformations limit reduces to that of an isotropic linearly elastic material. The values of the elastic constants were chosen to be $\lambda_0 = 153.25$ GPa and $\mu_0 = 78.95$ GPa, while the mass density was set to $\rho_0 = 2700$ Kg/m^3. The high-explosive material model and the values of its parameters have been described in section 3.5.4.5. For this example we consider the slower reaction rate $K = 2 \times 10^6$ s^{-1}, with $m = 0$. The cylinder, meshed with 80602 ten-noded tetrahedra and 112736 nodes, is initially at rest and it is free to deform anywhere on its boundary. At time $t = 0$ the cylinder is impacted on one of its planar surfaces imposing a velocity that compresses the explosive and initiates the detonation, $V_0 = 2176.932$ m/s. The velocity on the impact surface is kept constant throughout the computation. The time step was dynamically adapted according to equation (3.76), with $f_0 = 0.1$, $\Delta f = 0.09$, $w = 0.03$ m and $D = 9596$ m/s. Notice, however, that the speed of propagation of volumetric waves in the canister and explosive are approximately 10735 m/s and 3070 m/s, respectively. Consequently, there is a sharp transition in the size of the time steps from the canister to the explosive, as implied by equation (3.59).

A sequence of snapshots of the solution is shown in Figures 3.29–3.30. Pressure contours are shown on the upper half of each snapshot. Qualitatively, the solution shows that there is a first pressure wave accompanying the detonation front, followed by a decompression behind it. Later, a second pressure wave is initiated near the impact surface due to the continuous forcing exerted by the impactor. The number of updates for each element during a preset time interval is exhibited on the lower half of each snapshot. Only values on a plane that contains the cylinder axis are shown. The full power of asynchronous updates is illustrated in this sequence, namely, the time steps are dynamically refined over the reaction region and the method naturally gauges and takes advantage of an adequate time sampling frequency to integrate the elastic waves in each material.

The ease and simplicity with which Lagrangian formulations of mechanics deal with material interfaces truly deserve a separate remark. No special algorithm is needed in this case to treat the interface between the high-explosive and the solid canister. Of course, more detailed implementations would need fragmentation and contact algorithms, to allow for separation and slip between the two material boundaries.

A glance at the numerical solutions immediately reveals that they possess a very rich structure. Figure 3.31 shows four different views of the same pressure surface and contours over one plane of the set explosive-canister, at time t=9.9 μs. The first noteworthy feature is the presence of the shock in front of the detonation front, with a peak pressure of approximately 40 GPa. The theoretical peak or Von Neumann pressure p_{VN} in this case for a Chapman-Jouguet detonation advancing at constant speed, obtained after solving the Rankine-Hugoniot jump conditions, is perceptible higher and equal to 66.17 GPa. This indicates that, as expected, the detonation front is slowing down,

since the deformation of the canister behind the front relieves part of the pressure pushing the front forward. The fact that the pressure across the material interface is discontinuous might result somewhat counterintuitive, especially to the scientist accustomed to deal with fluid interfaces. This jump discontinuity in pressure is a clear reflection of the strong tri-axiality of the stress state in the solid canister, and the fact that the dynamic equilibrium between the two surfaces only involves the tractions on the surface and not the full stress tensor. Moreover, there are regions exhibiting strong pressure gradients across the thickness of the canister wall, bringing the material from negative to positive pressures in a very short distance. Finally, it should be noted that the pressure wave on the solid canister precedes the detonation front. This is not often seen in real cases, since seldom is the sound speed of the material in the canister faster than the detonation front speed. Based on the material properties chosen for this example, this is in fact true in this case.

3.6 Complexity and convergence

The computational costs involved in the AVI algorithm can be separated into those associated with the element updates, and the overhead involved in the determination of which element to update next. It is readily verified, however, that the latter cost is generally much smaller than the former, as shown next.

Complexity and cost estimates. We proceed to estimate the speedup afforded by AVIs relative to explicit Newmark, or other similar explicit method, with a time step

$$\Delta t_{\min} = \min_K \Delta t_K.$$

For a fixed final time T the cost C_{AVI} of the AVI method is

$$C_{\text{AVI}} = \underbrace{\left(C_{\text{EU}} + C_{\text{PQ}}\right)}_{\text{cost per time step}} \cdot \underbrace{\sum_K \frac{T}{\Delta t_K},}_{\text{\# time steps}}, \tag{3.80}$$

where C_{EU} is the cost per element update and C_{PQ} is the cost of inserting and removing one element from the priority queue. The corresponding cost for explicit Newmark is

$$C_{\text{NM}} = C_{\text{EU}} \cdot \sum_K \frac{T}{\Delta t_{\min}}. \tag{3.81}$$

If we neglect the priority queue cost by setting $C_{\text{PQ}} = 0$ then we can calculate the maximum AVI speedup to be

$$\lambda = \left.\frac{C_{\text{NM}}}{C_{\text{AVI}}}\right|_{C_{\text{PQ}}=0} = \frac{\sum_K \frac{1}{\Delta t_{\min}}}{\sum_K \frac{1}{\Delta t_K}}. \tag{3.82}$$

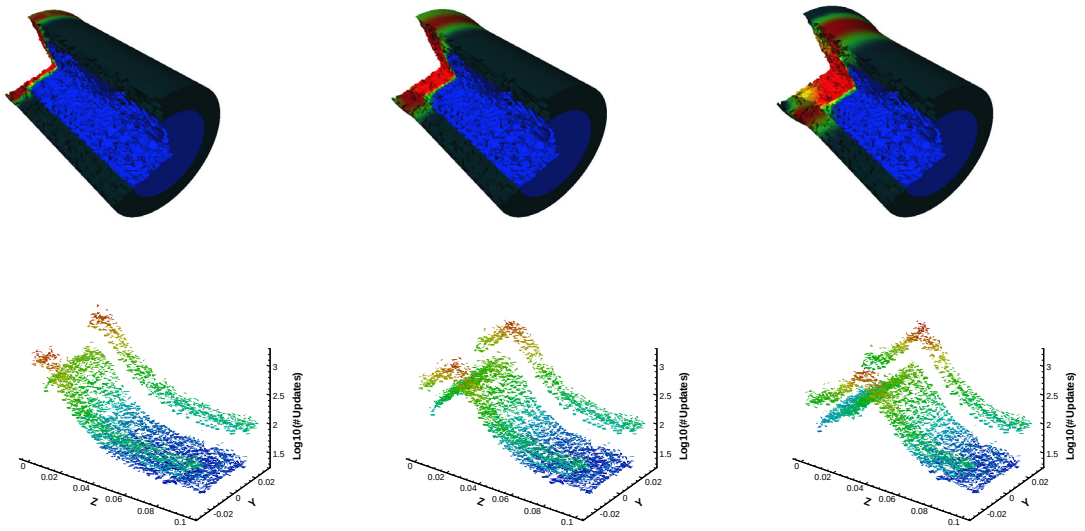

(a) t=0.9 μs (b) t=2.4 μs (c) t=3.9 μs

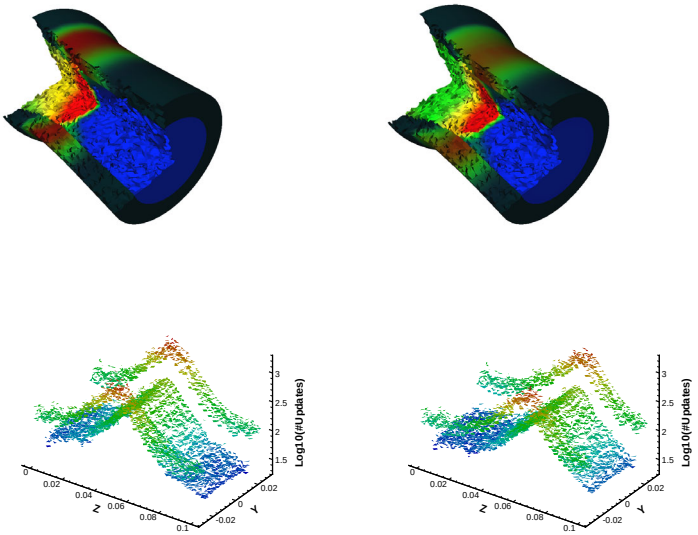

(d) t=5.4 μs (e) t=6.9 μs

Figure 3.29: Evolution of a detonation wave within a solid canister. The detonation is initiated by impacting one of the planar surfaces of the set canister-explosive. The pictures show the evolution of the number of elemental updates during a preset time interval (lower half of each snapshot) and the pressure contours (upper half of each snapshot), both in the explosive and in the sorrounding solid. The plots of the number of elemental updates only show values on a plane of the cylinder that contains its axis, and can be roughly described as composed of three strips. The central strip, which lies in the explosive region, has fewer elemental updates than the two thin lateral strips, which lie in the solid canister region. The sequence continues in Figure 3.30.

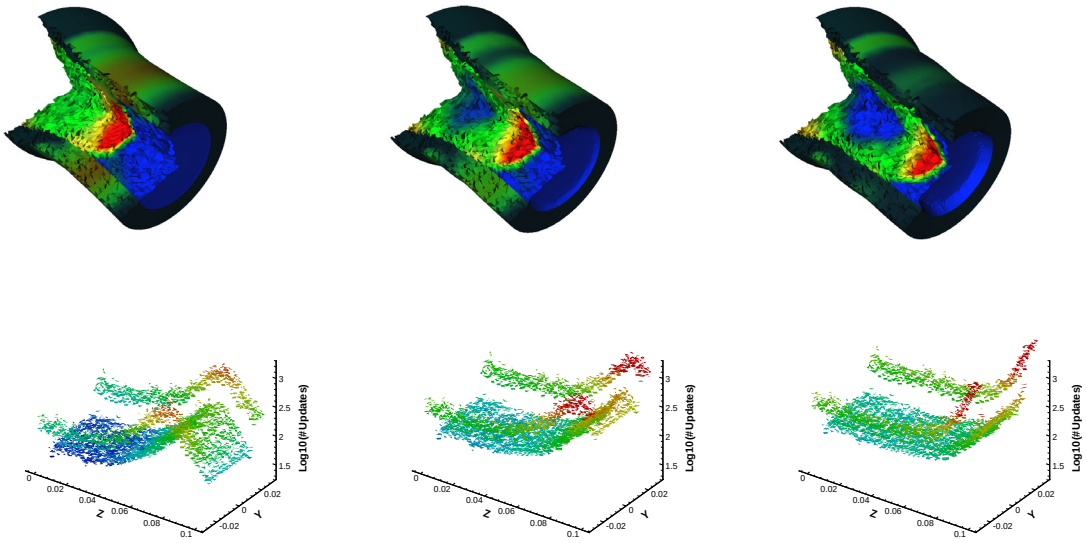

(a) t=8.4 μs (b) t=9.9 μs (c) t=11.4 μs

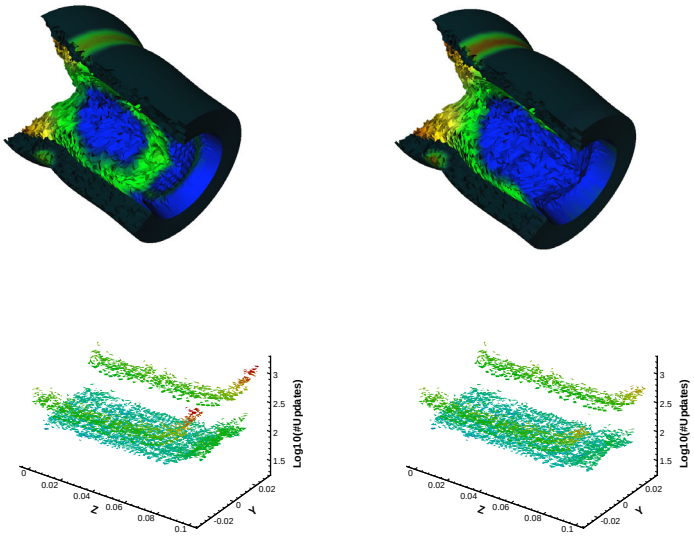

(d) t=12.9 μs (e) t=14.4 μs

Figure 3.30: Evolution of a detonation wave within a solid canister. The sequence of snapshots begins in Figure 3.29. The detonation is initiated by impacting one of the planar surfaces of the set canister-explosive. The pictures show the evolution of the number of elemental updates during a preset time interval (lower half of each snapshot) and the pressure contours (upper half of each snapshot), both in the explosive and in the sorrounding solid. The plots of the number of elemental updates only show values on a plane of the cylinder that contains its axis, and can be roughly described as composed of three strips. The central strip, which lies in the explosive region, has fewer elemental updates than the two thin lateral strips, which lie in the solid canister region.

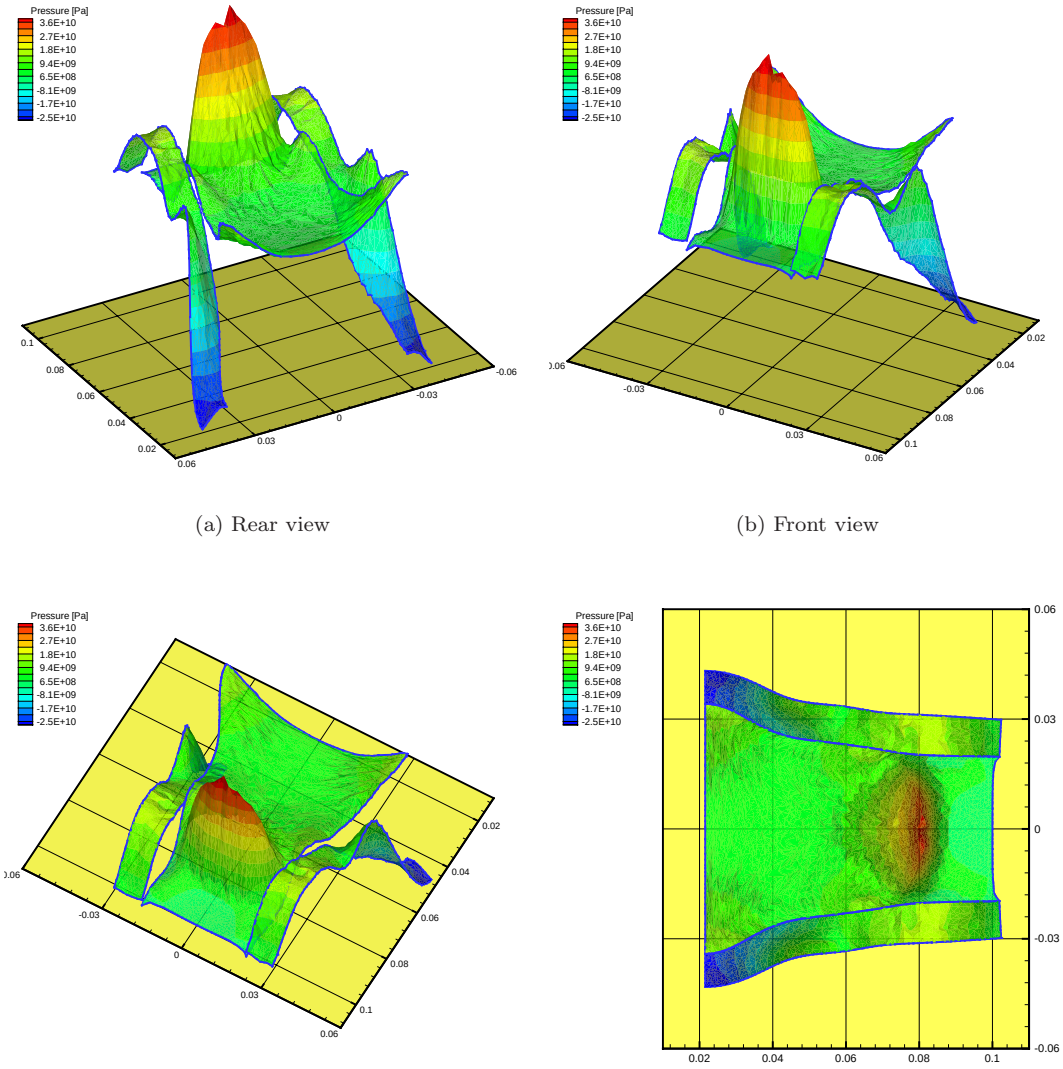

(a) Rear view

(b) Front view

(c) Front-upper view

(d) Top view

Figure 3.31: Four different views of the same pressure surface on one plane of the set canister-explosive at time 9.9 μs.

We now consider the effect on the cost of the priority queue, which we assume to be implemented using a balanced binary tree. Under these conditions, the cost is $C_{\mathrm{PQ}} = \kappa \log_2(E)$, where E is the number of elements in the mesh and κ is the cost per level of the binary tree, which can be taken to be constant. Specifically, our benchmarks give $\kappa \approx 0.2\mu s$. By contrast, the cost C_{EU} of an element update depends sensitively on the type of element and the constitutive model, and can be substantial for complex constitutive models. Even for relatively simple nonlinear elasticity models, however, this cost is still greatly in excess of C_{PQ}. For example, for a Neohookean material and six noded triangles, our numerical benchmarks give $C_{\mathrm{EU}} \approx 10\mu s$. We can now estimate the size of the mesh for which the cost C_{PQ} begins to dominate C_{EU}. The ratio of costs is given by

$$\frac{C_{\mathrm{PQ}}}{C_{\mathrm{EU}}} = \frac{\kappa}{C_{\mathrm{EU}}} \log_2(E) = 0.02 \log_2(E),$$

and for C_{PQ} to be greater than C_{EU} would thus require $\log_2(E) > 50$, i.e., an inordinately large mesh containing in the order of 10^{15} elements. Taking the priority-queue overhead into consideration, true AVI speedup is

$$\frac{C_{\mathrm{NM}}}{C_{\mathrm{AVI}}} = \frac{\lambda}{1 + \frac{\kappa}{C_{\mathrm{EU}}} \log_2(E)}. \tag{3.83}$$

In the helicopter-blade calculations, the number of elements is $E = 2089$, the cost of an elemental update for a ten-node tetrahedral element is $C_{\mathrm{EU}} \approx 25\mu s$. and thus

$$\frac{C_{\mathrm{NM}}}{C_{\mathrm{AVI}}} = \frac{6.4}{1 + \frac{0.2}{25} \log_2(2089)} = 5.9,$$

which is close to the optimal speedup $\lambda = 6.4$. These estimates demonstrate the relatively modest impact of the priority queue on the overall performance of the method.

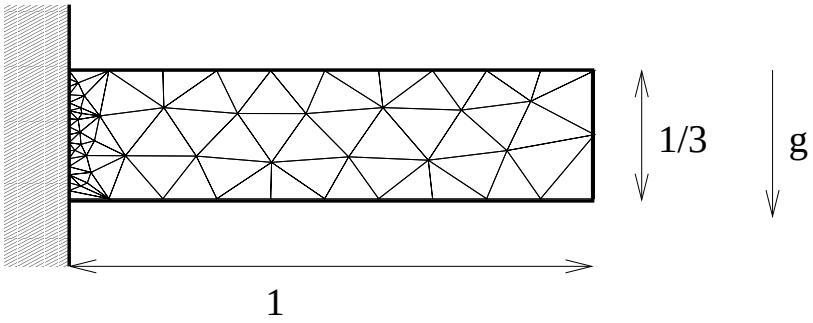

Figure 3.32: Schematic diagram of the geometry of the slab and the coarsest mesh for the cost/accuracy example

Cost/accuracy analysis. We quantitatively demonstrate that asynchronous methods can substantially lower the cost of a computation without degradation in accuracy by means of the following

numerical test. Consider a two–dimensional plane strain, nonlinear elastic slab clamped on one edge and free at the other, deflecting under the action of uniform gravity. The material is Neohookean extended to the compressible range, equation (3.9). The slab is initially undeformed and at rest. We consider an initial nonuniform mesh composed of 88 six-node quadratic triangles. A schematic picture of the geometry and the initial mesh are shown in Figure 3.32.

The initial mesh is refined by uniform quadrisection several times over, resulting in meshes containing 88, 352, 1408, 5632 and 22528 elements. For each mesh, the solution is computed up to a prescribed final time using both with AVIs and explicit Newmark, i.e., take $(\gamma, \beta) = (1/2, 0)$ in (2.56). The explicit Newmark calculations are started as

$$\begin{aligned} x_a^0 &= \varphi_0(X_a) \\ v_a^{1/2} &= \frac{\Delta t}{2} a_a^0 = -\frac{\Delta t}{2m_a} \frac{\partial \Phi}{\partial x_a}(x_a^0). \end{aligned}$$

In the AVI calculations, the appropriate initial conditions at node a are

$$\begin{aligned} x_a^0 &= \varphi_0(X_a) \\ v_a^{1/2} &= \frac{1}{2m_a} \sum_{\{K | a \in K\}} I_{Ka}^0, \end{aligned}$$

where $\varphi_0(X)$ is the initial deformation mapping and

$$I_{Ka}^0 = -\Delta t_K \frac{\partial V_K(x_K^0)}{\partial x_{Ka}^0}.$$

Note that this initialization procedure reduces to Newmark's for a uniform time step. An explicit Newmark solution computed with an exceedingly fine 90112-element mesh is presumed to be ostensibly converged, and used in lieu of the exact solution in order to compute errors.

The L^2-norm displacement and deformation-gradient errors are shown in Figure 3.33 as a function of the computational cost. It is evident from these plots that the computational cost incurred in the computation of solutions of equal accuracy is is substantially less for the AVIs.

Convergence of AVIs. The slope of the plots in Figure 3.33 is also directly related to the rate of convergence in Δt. To verify this, we note that the elemental time steps are proportional to the inner radius of the element, by virtue of the Courant condition. This implies that the rate of convergence in Δt is three-times the slope of the plots Figure 3.33. This gives a displacement rate of convergence of roughly 1.9, and a deformation-gradient rate of convergence of 1.1, for both methods.

The convergence of AVIs may also be established analytically. To this end, define the *maximum*

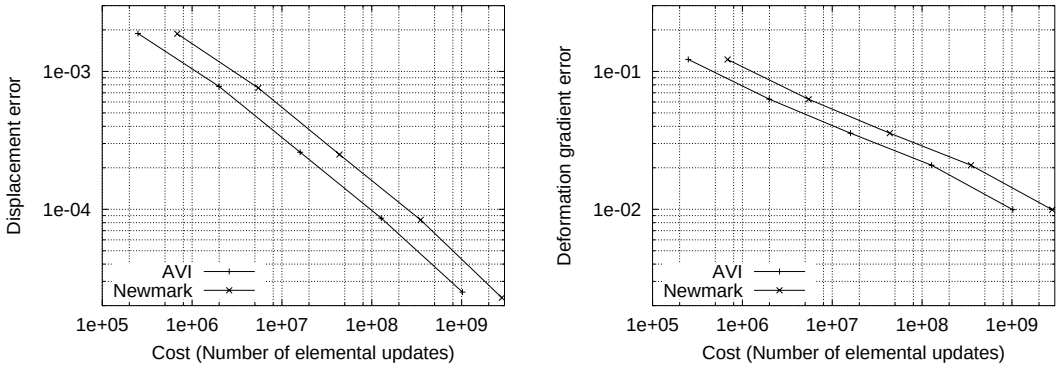

Figure 3.33: L^2 errors for the displacement (on the left) and the deformation gradient (on the right) as a function of the number of elemental updates for the slab problem. As is readily seen from the plots, AVIs are substantially cheaper than Newmark in computational cost for a desired error value.

time step

$$\Delta t_{\max} = \max_K \Delta t_K, \tag{3.84}$$

and the *maximum final time*

$$t_{\max} = \max_K t_K^{N_K}. \tag{3.85}$$

With these definitions we can state the following result, first published in Lew et al. [2003b] and due to Matt West.

Theorem 3.6.1 *Consider a sequence of solutions obtained by the application of asychronous variational integrators to a fixed spatial discretization with maximum time step $\Delta t_{max} \to 0$ and maximum final time $t_{max} \to t_f$. Then the final discrete configuration converges to the exact configuration of the semidiscrete problem at time t_f.*

The proof of theorem 3.6.1 can be consulted in Lew et al. [2003b]. We will not reproduce it in here.

Resonance instabilities in asynchronous methods. It is known that multi-time-step methods ocassionally exhibit resonance instabilities for some combinations of time steps (See, e.g., Izaguirre et al. [1999], Bishop et al. [1997] and Biesiadecki and Skeel [1993] in the case of molecular dynamics, and Daniel [1997a] and Daniel [1997b] in the case of finite element methods in elastodynamics). We have not been able to detect any such instabilities in our simulations; however, a systematic study has yet to be performed.

3.7 Extension of AVIs

In this section we comment on some possible extensions and ideas to be explored. The uninterested reader can skip it and continue directly to the next section.

Implicit AVI. Asynchronous algorithms do not necessarily need to be explicit. A locally implicit AVI method can be constructed by using, for instance, the discrete action sum

$$S_d = \sum_a \sum_{i=0}^{N_a-1} \frac{1}{2} m_a (t_a^{i+1} - t_a^i) \left\| \frac{x_a^{i+1} - x_a^i}{t_a^{i+1} - t_a^i} \right\|^2 - \sum_K \sum_{j=0}^{N_K-1} (t_K^{j+1} - t_K^j)\, \Phi_K(x_K^{(j+1)*}),$$

where

$$(x_K^{(j+1)*})_a = x_a^{i+1}\alpha_a + x_a^i(1-\alpha_a),$$

and such that $t_K^{j+1} = t_a^{i+1}$, with a nodal parameter $\alpha_a \in [0,1]$ for each node a. The corresponding discrete Euler–Lagrange equations possess x_a^{i+1} for every node $a \in K$ involved implicitly as an argument of the potential energy of the element, which needs to be solved for.

The algorithm shown in Figure 3.4 is modified to replace the explicit update of the positions of the nodes. It is substituted for the solution of a nonlinear system of equations for the new positions of all the nodes in the element under consideration.

Parallel AVI algorithms. In 3.3 we considered solving the AVI equations (3.43) by maintaining a priority queue to track which element has the smallest next time in the entire mesh. This is an overly strong requirement for solving the equations, however, as we can update an element whenever all of the adjacent elements have larger next times. This methodology provides the basis for the construction of parallel implementations of AVI methods.

One simple scheme for doing this, albeit not necessarily the best one, is to assign to each processor a group of elements to advance, and maintain two priority queues per processor. One of the priority queues plays the same role as in the serial case. Every time an element is popped from this priority queue we check that all of its neighbors have in fact larger next times, and if this is the case, we update it and push it into this priority queue again. Otherwise, we push this element into the second priority queue. This will often happen for elements lying in the boundaries between different processor domains, and they will in turn make some of its neighbors be included in the second priority queue as well. Periodically, we stop computations in the first priority queue and advance the second priority queue in all processors, in a communication intensive stage. Once we emptied the second queue in every processor, we start over with the first priority queue.

The algorithm above intends to take advatadge of collective communications and larger message sizes, instead of having permanent communications for each piece of data that is necessary to interchange. Nevertheless, better and more optimal algorithms can surely be constructed along similar ideas.

Stochastic sorting for element updates. In Lew et al. [2003b] we described an implementation of AVIs that does not use a priority queue to decide the element updates. In this case, the elements

to be updated are chosen at random, and an element is updated whenever all of its neighbors have larger next times. Otherwise, the adjacent element with the smaller next time is chosen and the same test is performed. The algorithm is guaranteed to terminate, and as described in Lew et al. [2003b], it has the advantage over the priority queue of having an average cost that is constant, i.e., independent of the number of elements in the mesh.

In any case, in section 3.6 we showed that for all practical purposes the cost of the priority queue is in effect negligible, and therefore the decision about the implementation becomes a matter of taste.

3.8 Periodic boundary conditions

We close this chapter by discussing the implementation of periodic boundary conditions for Lagrangian mechanical systems within the variational framework. As we shall see, this is one more example in which the right equilibrium equations are easily obtained from the variational structure in a graceful and elegant way.

We consider then two subsets of the boundary $\partial_1\mathcal{B} \subset \partial\mathcal{B}$ and $\partial_2\mathcal{B} \subset \partial\mathcal{B}$, and a one-to-one and onto mapping between the two $\psi : \partial_1\mathcal{B} \to \partial_2\mathcal{B}$. Prescribing "periodic" boundary conditions means to consider motions $\varphi(X,t)$ that satisfy

$$\varphi(X,t) = \varphi(\psi(X),t)$$

for all $X \in \partial_1\mathcal{B}$ and for all t. Hamilton's principle seeks motions $\varphi(X,t)$ rendering the action stationary with respect to admissible variations, which among possibly other requirements, should satisfy that

$$\delta\varphi(X,t) = \delta\varphi(\psi(X),t).$$

In addition to the equilibrium equations (3.18)- (3.19), we also obtain that

$$P_i{}^I N_I\Big|_{(X,t)} + P_i{}^I N_I\Big|_{(\psi(X),t)} = 0 \tag{3.86}$$

for all $X \in \partial_1\mathcal{B}$ and for all t, which just states that the tractions should be continuous across a periodic boundary.

In the discrete case we adopt a similar approach to derive the discrete Euler–Lagrange equations. We want to identify each node a in $\partial_1\mathcal{B}$ with a node a' in $\partial_2\mathcal{B}$ such that they satisfy $\psi(X_a) = X_{a'}$. This provides conditions to be taken into account when constructing the discretization for $\mathcal{B}$. Next, we derive the discrete Euler–Lagrange equations by either a) considering each pair of nodes (a,a') as a single degree of freedom, or b) by adding a constraint term to the discrete actions sum for

each pair on nodes (a,a') on the periodic boundary. In either case, the discrete variational principle provides the right discrete equations for the algorithm.

In case a) the discrete Euler–Lagrange equation for a (a,a') takes the form

$$D_{a,i}S_d + D_{a',i}S_d = 0, \tag{3.87}$$

which is the analog to equation (3.86). On the other hand, in case b), we obtain

$$0 = D_{a,i}S_d + \lambda \tag{3.88a}$$

$$0 = D_{a',i}S_d - \lambda \tag{3.88b}$$

$$0 = x^i_a - x^i_{a'}, \tag{3.88c}$$

where λ is the Lagrange multiplier of the constraint. Equation (3.87) directly corresponds to considering the discrete equations of motion for a periodic arrangement of domains $\mathcal{B}$, as if the boundaries $\partial_1\mathcal{B}$ and $\partial_2\mathcal{B}$ did not exist. On the other hand, equations (3.88) correspond to imposing continuity of tractions and displacements between $\partial_1\mathcal{B}$ and $\partial_2\mathcal{B}$. Of course, both systems of equations are completely equivalent and lead to the same results. It is notheworthy how easily the variational framework allows us to recover both interpretations and their corresponding discrete equations.

Chapter 4

Time-adaption and discrete path integrals

In this chapter we revisit the formulation of Hamilton's principle and construct a unique framework from which we derive and analyze finite–dimensional mechanical systems and static and dynamic continuum mechanics. We obtain the energy balance and the configurational force equilibrium equations, as well as the associated conservation properties, both in the continuous and the discrete formulations. Of course, many of these concepts have been known for some time, but we feel it is a very elegant presentation that truly elucidates the origin and relation between many of the relevant mechanical concepts in continuum mechanics, particularly in solid mechanics.

We focus specifically in analyzing the solvability of the local energy balance equation for AVIs, obtained as the DEL equation corresponding to the elemental time step in the extended Hamilton principle. Also, we construct discrete versions of the path independent J and L integrals. We conclude by stating the discrete Noether theorem in the fully asynchronous case.

Henceforth we adopt Einstein's summation rule for repeated indices. A comma followed by a coordinate index indicates derivative with respect to that coordinate.

4.1 Space–time Lagrangian mechanics

In this section we review the abstract formulation of space–time Lagrangian mechanics and apply it to dynamic and static continuum mechanics and ordinary differential equations. The salient feature of the forthcoming development is that it considers variations in both the reference space–time and the deformed configurations. As a consequence, we obtain the energy conservation and the equilibrium of configurational forces as Euler–Lagrange equations of the variational principle.

4.1.1 Variational principles and equations of motion

Now we derive the equations of motion for a continuum. For this, let $\mathcal{X} \in \mathbb{R}^m$ be an open space–time reference configuration and Z^μ denote the μ-th coordinate in $\mathcal{X}$. We seek a deformation mapping $\varphi(Z)$ that takes the point Z in the reference configuration to the point $x \in \mathbb{R}^n$, in the deformed configuration, with coordinates x^i, $i = 1, \ldots, n$. The Lagrangian density of the continuum is given by a function $L(\varphi, \nabla_Z \varphi, Z)$, and the action functional follows as

$$S[\varphi] = \int_{\mathcal{X}} L(\varphi, \nabla_Z \varphi, Z)\, dZ.$$

The variational principle states that the deformation mapping should be a critical point of the action functional. The variations of the action functional are

$$\delta S[\varphi] = \int_{\partial \mathcal{X}} \frac{\partial L}{\partial \varphi^i_{,\mu}} N_\mu \delta\varphi^i \, dZ - \int_{\mathcal{X}} \left[\frac{\partial L}{\partial \varphi^i} - \frac{\partial}{\partial Z^\mu} \frac{\partial L}{\partial \varphi^i_{,\mu}} \right] \delta\varphi^i \, dZ, \tag{4.1}$$

where N is the outer unit normal to $\mathcal{X}$. The corresponding Euler–Lagrange equations are obtained

$$\frac{\partial L}{\partial \varphi^i} - \frac{d}{dZ^\mu} \frac{\partial L}{\partial \varphi^i_{,\mu}} = 0 \tag{4.2}$$

for all $Z \in \mathcal{X}$.

Boundary conditions. The deformation mapping is subject to essential boundary conditions on part of the boundary $\partial_d \mathcal{X} \subset \partial \mathcal{X}$. Traction-like boundary conditions are imposed by requesting

$$\frac{\partial L}{\partial \varphi^i_{,\mu}} N_\mu = \tau_i \tag{4.3}$$

on $\partial_\tau \mathcal{X} \subset \partial \mathcal{X}$, where τ is a vector-valued field on $\partial_\tau \mathcal{X}$. We enforce the essential boundary conditions directly. On the other hand, we modify the variational principle asking it to satisfy

$$\delta S[\varphi] = \int_{\partial_\tau \mathcal{X}} \tau_i \delta\varphi^i$$

for all admissible variations in order to impose the traction-like boundary conditions. Of course, conditions on the sets $\partial_\tau \mathcal{X}$ and $\partial_d \mathcal{X}$ are necessary to guarantee the well-posedness of the problem.

Dynamic continuum mechanics. The equations describing the dynamics of a continuum are obtained by choosing $\mathcal{X} = (0, T) \times \mathcal{B}$, where $\mathcal{B}$ is an open connected region of $\mathbb{R}^3$. In keeping with standard practice, we let $Z^0 = t$ to be the time coordinate, and $Z^I = X^I$, $I = 1, 2, 3$, to be the spatial coordinates, so the coordinates of a point Z are given by (t, X^1, X^2, X^3).

The deformation mapping $\varphi(t, X^1, X^2, X^3)$ maps the reference configuration $\mathcal{B}$ at each time t

into the deformed one, which is assumed to be a subset of $\mathbb{R}^3$. The trajectory of the material particle at X is

$$x(t) = \varphi(t, X),$$

while its velocity and acceleration follow as $\dot{\varphi}(t, X)$ and $\ddot{\varphi}(t, X)$.

The Lagrangian density is chosen to be of the form

$$L(\varphi, \dot{\varphi}, \nabla_X \varphi, X, t) = \frac{\rho_0}{2} \|\dot{\varphi}\|^2 - W(\nabla_X \varphi, X) - \rho_0 V(X, \varphi), \tag{4.4}$$

which describes the dynamics of hyperelastic materials. In (4.4) ρ_0 is the density per unit of undeformed volume, and $V(X, \varphi)$ is the external potential energy per unit mass, such as gravity. The strain-energy density per unit of undeformed volume $W(F, X)$, where $F \in \mathbb{R}^{3\times 3}$ such that $\det F > 0$, is subject to the requirement of material frame indifference, i.e.,

$$W(Q \cdot F, X) = W(F, X)$$

for all rotations $Q \in SO(3)$. The first Piola-Kirchhoff stress tensor follows as

$$P_i{}^I = \frac{\partial}{\partial F^i{}_I} W(F, X),$$

while the Cauchy stress tensor is

$$\sigma_{ij} = J^{-1} P_i{}^I F_{jI},$$

where

$$J = \det F$$

is the Jacobian of the deformation mapping.

The Euler–Lagrange equations (4.2) translate into the infinitesimal balance of linear momentum

$$\frac{\partial P_i^I}{\partial X^I} - \frac{\partial V}{\partial \varphi^i}(X, \varphi) - \rho_0 \ddot{\varphi} = 0. \tag{4.5}$$

If present, the traction-like boundary conditions (4.3) reduce to prescribing the tractions over $(0, T) \times \partial_\tau \mathcal{B}$, where $\partial_\tau \mathcal{B} = \partial_\tau \mathcal{X} \cap \partial \mathcal{B}$, or the velocities in $\mathcal{B}$ at time $t = 0$ or $t = T$.

Static continuum mechanics. The static equilibrium equations for a hyperelastic continuum are obtained by choosing $\mathcal{X} = \mathcal{B} \subset \mathbb{R}^3$ and a Lagrangian density of the form

$$L(\varphi, \nabla_X \varphi, X) = W(\nabla_X \varphi, X). \tag{4.6}$$

The Euler–Lagrange equations (4.2) reduce to

$$\frac{\partial P_i{}^I}{\partial X^I} = 0,$$

which just states that the divergence of the stress tensor should be zero everywhere in the body.

Ordinary differential equations. In this case space–time has only one dimension, namely time, and the Euler–Lagrange (4.2) equations reduce to (2.3).

4.1.2 Noether's theorem and momentum conservation

Consider a one–parameter family φ^ε of deformation mappings that are a symmetry of the mechanical system, i.e., $S[\varphi] = S[\varphi^\varepsilon]$ where $\varphi^0 = \varphi$. Denote by

$$\xi = \frac{\partial \varphi^\varepsilon}{\partial \varepsilon}\Big|_{\varepsilon=0}$$

the infinitesimal generator of the symmetry. Therefore we have that

$$0 = \left.\frac{\partial S[\varphi^\varepsilon]}{\partial \varepsilon}\right|_{\varepsilon=0} = \int_{\partial \mathcal{X}} \frac{\partial L}{\partial \varphi^i_{,\mu}} N_\mu \xi^i \, dZ, \tag{4.7}$$

where we have used the definition of the symmetry for the left equality and equation (4.1) for the right one, assuming φ satisfies the Euler–Lagrange equations (4.2). This is the integral form of Noether's theorem.

In fact, this holds over any subset $\mathcal{X}' \subseteq \mathcal{X}$, as can be seen by repeating the previous calculation with the action integral restricted to $\mathcal{X}'$.

Dynamic continuum mechanics. Given $\mathcal{X} = (0,T) \times \mathcal{B}$ as before, the boundary is given by $\partial\mathcal{X} = \partial\mathcal{B} \cup \{0\} \times \mathcal{B} \cup \{T\} \times \mathcal{B}$. Expression (4.7) becomes

$$\int_{\mathcal{B}} \frac{\partial L}{\partial \dot\varphi^i} \xi^i \, dX \bigg|_{t=T} - \int_{\mathcal{B}} \frac{\partial L}{\partial \dot\varphi^i} \xi^i \, dX \bigg|_{t=0} = - \int_0^T \int_{\partial\mathcal{B}} \frac{\partial L}{\partial \varphi^i_{,I}} \xi^i N_I \, dX \, dt. \tag{4.8}$$

We obtain the balance of global linear momentum in the direction $v \in \mathbb{R}^3$ if the family of mappings $\varphi^\varepsilon = \varphi + \varepsilon v$ is a symmetry of the mechanical system. In this case, $\xi = v$, and (4.8) becomes

$$v^i \left[\int_{\mathcal{B}} \rho_0 \dot\varphi_i \, dX|_{t=T} - \int_{\mathcal{B}} \rho_0 \dot\varphi_i \, dX|_{t=0} - \int_0^T \int_{\partial\mathcal{B}} P_i^I N_I \, dX \, dt \right] = 0,$$

which implies that the component of the linear momentum balance parallel to v is exactly zero. Analogously, we can consider the case in which the family of mappings $\varphi^\varepsilon = \exp(\varepsilon\Omega)\varphi$ is a symmetry

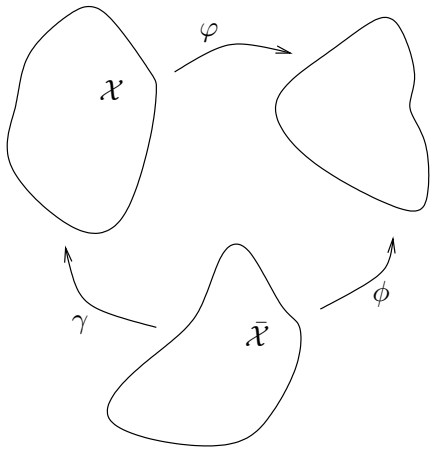

Figure 4.1: Schematic representation of the relation between γ, ϕ and φ. The parametric configuration $\bar{\mathcal{X}}$ and the reference configuration $\mathcal{X}$ are isomorphic.

of the mechanical system, where Ω is a 3×3 skew–symmetric matrix. Define $\omega \in \mathbb{R}^3$ such that $\Omega = *\omega$, i.e., $\Omega^i{}_j = \epsilon_k{}^i{}_j \omega^k$, where ϵ is the skew–symmetric Levi-Civita permutation tensor. Then, $\xi^i = \Omega^i{}_j \varphi^j = \epsilon_k{}^i{}_j \omega^k \varphi^j$ and (4.8) states that

$$\omega^k \left[\int_{\mathcal{B}} \epsilon_{kj}{}^i \varphi^j \rho_0 \dot{\varphi}_i \, dX \big|_{t=T} - \int_{\mathcal{B}} \epsilon_{kj}{}^i \varphi^j \rho_0 \dot{\varphi}_i \, dX \big|_{t=0} - \int_0^T \int_{\partial \mathcal{B}} \epsilon_{kj}{}^i \varphi^j P_i^I N_I \, dX \, dt \right] = 0,$$

which implies that the component of the angular momentum balance parallel to ω is zero.

4.1.3 Restated variational principles and configurational forces

The variational principle in section 4.1.1 can be restated in a more general way to obtain the configurational forces equilibrium equations, of which energy balance and the conservation of the J and L integrals are examples. Consider a smooth one-to-one and onto map γ from an open set $\bar{\mathcal{X}} \subset \mathbb{R}^m$, the parametric configuration, to the reference configuration $\mathcal{X}$. Denote $\phi = \varphi \circ \gamma$ the composition map from the parametric configuration $\bar{\mathcal{X}}$ to the deformed configuration, as illustrated in Figure 4.1. The μ-th coordinate of a point in the parametric configuration is denoted $\bar{Z}^\mu$.

Next, consider the action functional of section 4.1.1 as a function of ϕ and γ

$$S[\phi, \gamma] = \int_{\mathcal{X}} L(\phi \circ \gamma^{-1}, \nabla_Z (\phi \circ \gamma^{-1}), Z) \, dZ = \int_{\bar{\mathcal{X}}} L(\phi, \nabla_{\bar{Z}} \phi \cdot \nabla_{\bar{Z}} \gamma^{-1}, \gamma) \ \det \nabla_{\bar{Z}} \gamma \ d\bar{Z}.$$

Varying the action with respect to ϕ gives the Euler–Lagrange equations (4.2). The variations of the action with respect to γ are

$$\delta S|_\phi = \int_{\mathcal{X}} \left[\frac{\partial L}{\partial Z^\nu} + \frac{d}{dZ^\mu} \left(\frac{\partial L}{\partial \varphi^i_{,\mu}} \varphi^i_{,\nu} - L \delta^\mu_\nu \right) \right] \delta\gamma^\nu \ dZ - \int_{\partial \mathcal{X}} \left(\frac{\partial L}{\partial \varphi^i_{,\mu}} \varphi^i_{,\nu} - L \delta^\mu_\nu \right) N_\mu \delta\gamma^\nu \ dZ. \quad (4.9)$$

By restricting the variations of γ to be zero on the boundary, we obtain the corresponding Euler–Lagrange equation

$$\frac{\partial L}{\partial Z^\nu} + \frac{d}{dZ^\mu}\left(\frac{\partial L}{\partial \varphi^i_{,\mu}}\varphi^i_{,\nu} - L\delta^\mu_\nu\right) = 0. \tag{4.10}$$

Note that by not varying γ on the boundary of $\bar{\mathcal{X}}$, the composition $\phi \circ \gamma^{-1}$ is always a deformation mapping of the class considered in section 4.1.1. Equations (4.10) then should not add any new condition on the dynamics, since the action does not depend on ϕ and γ separately, but through φ. Therefore, a deformation mapping $\varphi = \phi \circ \gamma^{-1}$ that satisfies the Euler–Lagrange equations (4.2) should satisfy equation (4.10) automatically. This can be checked through direct computation, as seen from replacing the identity

$$\frac{dL}{dZ^\mu} = \frac{\partial L}{\partial \varphi^i}\varphi^i_{,\mu} + \frac{\partial L}{\partial \varphi^i_{,\nu}}\varphi^i_{,\nu\mu} + \frac{\partial L}{\partial Z^\mu}$$

in equation (4.10).

The expression between parentheses in equation (4.10) is known as Eshelby's energy-momentum tensor, i.e.,

$$C_\nu{}^\mu = \frac{\partial L}{\partial \varphi^i_{,\mu}}\varphi^i_{,\nu} - L\delta^\mu_\nu, \tag{4.11}$$

and equation (4.10) states the balance of configurational forces.

Horizontal and vertical variations. The restated variational principle has an important geometric interpretation. Notice that (ϕ, γ) is a map from $\bar{\mathcal{X}}$ to $(\mathbb{R}^n, \mathcal{X})$. Any pair (ϕ, γ) can be regarded as a curve in $\mathcal{X} \times \mathbb{R}^n$, such that for each value in $\mathcal{X}$ there is one and only one value in $\mathbb{R}^n$. Figure 4.2 provides a graphical representation, where $\mathcal{X}$ is drawn in the horizontal axis and $\mathbb{R}^n$ in the vertical one. Variations with respect to ϕ and γ can also be readily interpreted from this diagram. A variation $(0, \delta\gamma)$ is equivalent to displacing points in the (ϕ, γ)-curve horizontally by the amount $\delta\gamma$. A variation $(\delta\phi, 0)$ is equivalent to displacing points in the curve vertically by the amount $\delta\phi$. Consequently, variations on γ are also called *horizontal variations*, while variations on ϕ also receive the name of *vertical variations*. Notice that any vertical variation can be interpreted as a horizontal variation as well. This will be of importance in section 4.2.6.

For the dynamic continuum mechanics case, it is often insightful to distinguish between the time axis and the reference configuration $\mathcal{B}$ in $\mathcal{X}$. The corresponding picture is shown in Figure 4.3. Notice that in this case horizontal variations include time variations. We will discuss more about this in section 4.1.5.

Noether's theorem. In addition to the conservation properties obtained from considering symmetries of the action acting on the deformed configuration, there are additional conserved quantities emanating from symmetries on the reference configuration. Consider a one–parameter family of

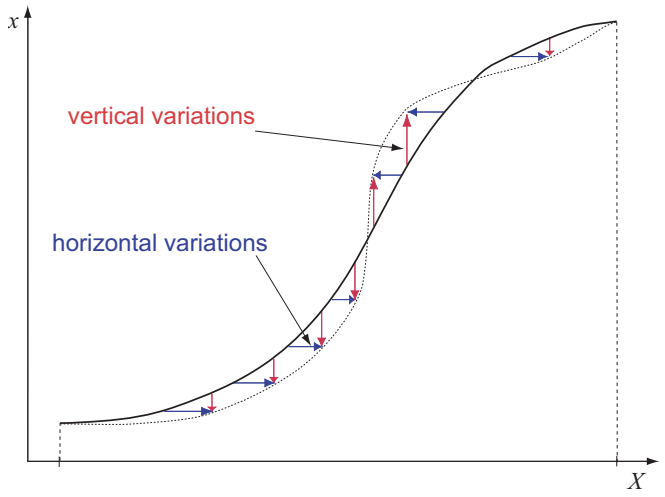

Figure 4.2: Graphical representation of vertical and horizontal variations. The thick line is a deformation mapping, while the dashed line represents the varied curve.

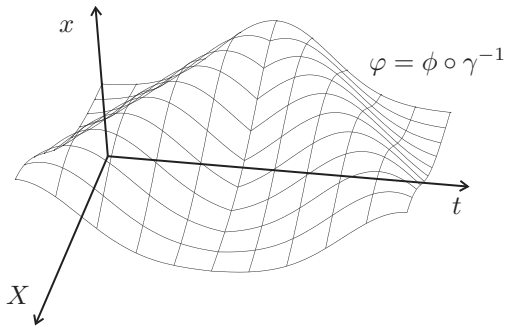

Figure 4.3: A graphical representation of a deformation mapping φ for elastodynamics. The horizontal axes represent space–time and together they form the reference configuration $\mathcal{X} = \mathbb{R} \times \mathcal{B}$. The vertical axis represents $\mathbb{R}^n$ where the deformed configuration lives. Taking a slice of φ with constant X gives the trajectory of the particle with material coordinates X for all time. Alternatively, taking a slice of φ with constant $t \in \mathbb{R}$ gives the configuration of the entire body at a single instant of time. Note that any motion of the continuum is represented as a surface in this diagram.

maps γ^ε that are a symmetry of the mechanical system, i.e., $S[\phi,\gamma^\varepsilon]=S[\phi,\gamma]$ for a fixed deformed configuration given by ϕ, where $\gamma^0=\gamma$. Therefore as in section 4.1.2, we have

$$0=\left.\frac{\partial S}{\partial\varepsilon}\right|_{\varepsilon=0}=-\int_{\partial\mathcal{X}}\left(\frac{\partial L}{\partial\varphi^i_{,\mu}}\varphi^i_{,\nu}-L\delta^\mu_\nu\right)N_\mu\xi^\nu\ dZ=-\int_{\partial\mathcal{X}}C_\nu{}^\mu N_\mu\xi^\nu\ dZ, \tag{4.12}$$

where we have used the definition of the symmetry on the left equality, and equation (4.9) on the right one, assuming that γ satisfies the Euler–Lagrange equations (4.10). As before,

$$\xi^\nu=\left.\frac{\partial\gamma^\varepsilon}{\partial\varepsilon}\right|_{\varepsilon=0}$$

is the infinitesimal generator of the symmetry.

4.1.4 Time symmetry and energy conservation

Energy conservation can be regarded in this context as a consequence of the translational symmetry along the time axis. We will see this in the ordinary differential equations and dynamic continuum mechanics cases separately.

Ordinary differential equations. Eshelby's energy-momentum tensor, in this case a scalar, simplifies to be the energy of the mechanical system. Consider then the family of mappings $\gamma^\varepsilon(t)=t+\varepsilon$, with infinitesimal generator $\xi=1$. If the Lagrangian density does not depend explicitly on time so that the family of mappings is a symmetry of the mechanical system, we have from (4.12) that the energy at the beginning and the end of the time interval should be the same.

Dynamic continuum mechanics. The expression for Eshelby's momentum tensor is

$$C=\begin{bmatrix}\frac{\rho_0}{2}\|\dot\varphi\|^2+W+\rho_0V & -\dot\varphi^{\mathsf T}P\\ \rho_0F^{\mathsf T}\dot\varphi & -F^{\mathsf T}P+(\rho_0V+W-\frac{\rho_0}{2}\|\dot\varphi\|^2)I\end{bmatrix},$$

where I stands for the 3×3 identity matrix, and $F=\nabla_X\varphi$ is the deformation gradient. Consider the family of mappings $\gamma^\varepsilon(t,X)=(t+\varepsilon,X)$, with the infinitesimal generator $\xi=(1,0,0,0)$. If the Lagrangian density is not time dependent so that the family of mappings is a symmetry of the mechanical system, then by replacing in (4.12) we obtain

$$\int_{\mathcal{B}}(\frac{\rho_0}{2}\|\dot\varphi\|^2+W+\rho_0V)\ dX\Big|_0^T-\int_0^T\int_{\partial\mathcal{B}}N_IP_i{}^I\dot\varphi^i\ dX\ dt=0,$$

which is the familiar statement of energy balance between the initial and final times.

4.1.5 Reference symmetries and conserved path integrals

Dynamic continuum mechanics. In addition to the symmetry associated to time axis translations, two path independent integrals are obtained from analyzing the effect of translations and rotations on the reference configuration. To do this, note that equation (4.12) in Noether's theorem holds after replacing $\mathcal{X}$ for any of its subsets.

Firstly, let $\mathcal{C} \subset \mathcal{B}$ and $[t_1, t_2] \subset [0, T]$. Let $v \in \mathbb{R}^3$ be a unit vector and consider the family of mappings $\gamma^\varepsilon(t, X) = (t, X + \varepsilon v)$, with the infinitesimal generator $\xi = (0, v^1, v^2, v^3)$. If the Lagrangian density is not dependent on X, the family of mappings is a symmetry of the mechanical system. Therefore, from (4.12) we obtain

$$v^J \left[\int_{\mathcal{C}} \rho_0 \dot{\varphi}_i F^i{}_J \, dX \Big|_{t_1}^{t_2} - \int_{t_1}^{t_2} \int_{\partial \mathcal{C}} \left[P_i{}^I F^i{}_J + (\frac{\rho_0}{2} \|\dot{\varphi}\|^2 - W - \rho_0 V) \delta^I{}_J \right] N_I \, dX \, dt \right] = 0. \tag{4.13}$$

Since (4.13) is valid for all v, the expression in the large square brackets is identically zero, and it is valid for all subsets $\mathcal{C} \in \mathcal{B}$ and $[t_1, t_2] \subset [0, T]$. The formula (4.13), among other things, is the fundamental identity behind the definition of a space–time path independent dynamic J-integral, of utmost importance for dynamic fracture mechanics.

Secondly, consider the family of mappings $\gamma^\varepsilon(t, X) = (t, \exp(\varepsilon \Omega) X)$, where Ω is a skew–symmetric matrix. The infinitesimal generator is $\xi = (t, \omega \times X)$, where ω is the axial vector of Ω, $\omega = *\Omega$. If the Lagrangian density is independent of X, the family γ^ε is a symmetry whose conserved quantity is

$$\omega^K \left[\int_{\mathcal{C}} \epsilon^{JKL} X_L \, \rho_0 \dot{\varphi}_i F^i{}_J \, dX \Big|_{t_1}^{t_2} - \int_{t_1}^{t_2} \int_{\partial \mathcal{C}} \epsilon^{JKL} X_L \left[P_i{}^I F^i{}_J + (\frac{\rho_0}{2} \|\dot{\varphi}\|^2 - W - \rho_0 V) \delta^I{}_J \right] N_I \, dX \, dt \right] = 0, \tag{4.14}$$

where ϵ^{JKL} is the Levi-Civita permutation tensor. Since equation (4.14) is valid for all $\omega \in \mathbb{R}^3$, the expression in the large square brackets is equal to zero. Here too, it is valid for all subsets $\mathcal{C} \subset \mathcal{B}$ and $[t_1, t_2] \subset [0, T]$. The path independence of the dynamic fracture mechanics L-integral is obtained from equation (4.14).

Static continuum mechanics. In this case Eshelby's energy-momentum tensor reduces to

$$C_J{}^I = -P_i{}^I F^i{}_J + (W + \rho_0 V) \delta^I{}_J. \tag{4.15}$$

We assume $V = 0$ in equations (4.13-4.14), and recall that we are considering time independent deformation mappings. In this case we obtain that

$$\int_{\partial\mathcal{C}} (P_i{}^I F^i{}_J - W\delta^I{}_J) N_I \; dX = 0 \tag{4.16}$$

and

$$\int_{\partial\mathcal{C}} \epsilon^{JKL} X_L (P_i{}^I F^i{}_J - W\delta^I{}_J) N_I \; dX = 0 \tag{4.17}$$

for all subsets $\mathcal{C} \subset \mathcal{B}$. Equations (4.16) and (4.17) are the path independent integrals associated to the translational and rotational symmetries in the reference configuration. These identities are the basis to define the fracture mechanics J and L integrals, respectively.

For the particular case in which the strain energy density W does not depend explicitly on X and is homogeneous of degree m, the dimension of $\mathcal{B}$, an additional path independent integral appears. Under these hypotheses we have that $W(\lambda F) = \lambda^m W(F)$ for all $\lambda > 0$, and the potential energy is invariant under the one–parameter family of transformations $\gamma^\lambda(X) = \lambda X$ of the reference configuration. To see this denote $Y = \lambda X$, and note that

$$\int_{\mathcal{C}} W(\nabla_X \varphi) \; dX = \int_{\lambda\mathcal{C}} W(\lambda \nabla_Y \varphi(Y/\lambda)) \; \frac{dY}{\lambda^m} = \int_{\lambda\mathcal{C}} W(\nabla_Y \varphi(Y/\lambda)) \; dY.$$

The infinitesimal generator of this symmetry is $\xi = X$. After replacing in (4.12) we obtain

$$\int_{\mathcal{C}} (P_i{}^I F^i{}_J - W\delta^I{}_J) N_I X^J \; dX = 0, \tag{4.18}$$

which is the fundamental identity to derive the path-independence of the M-integral.

A thorough discussion on configurational forces and conserved integrals can be found in Gurtin [2000], Knowles and Sternberg [1972], Rice [1985] or Eshelby [1970].

4.1.6 Multisymplecticity

Finite–dimensional mechanical systems possess a symplectic form that is preserved along the motion, as discussed in section 2.5 for example. Likewise, infinite–dimensional mechanical systems have a symplectic form that is preserved by the motion as well. This form is referred to as the *multisymplectic form*. The reason for the prefix "multi" is that it is not longer a bilinear or two–form, but an $m+2$–form, where $m+1$ is the dimension of $\mathcal{X}$.

The preservation of the multisymplectic form as well as the multisymplectic form itself can be derived by following similar steps to those in the derivation of the symplectic form in section 2.5. Nevertheless, without introducing intrinsic notation this is a rather cumbersome computation. We refer to Lew et al. [2003a]; Marsden and Shkoller [1999] for the details.

We would like to remark, however, one of the important consequences of the preservation of the multisymplectic form in elasticity, namely, the static and dynamic reciprocity relations for linearized problems, as shown in Lew et al. [2003a].

Linearized static continuum mechanics equations. In the following developments, we assume γ to be the identity. Recall that we say that ϕ is a solution of the Euler–Lagrange equations with displacement and traction boundary conditions (4.3) if it satisfies

$$DS(\phi) \cdot v = \int_{\partial_\tau \mathcal{B}} \tau \cdot v \; dA \; dt$$

for all variations v which are zero on the displacement boundary $\partial_d \mathcal{B}$. With DS we indicate the derivative[1] of S with respect to ϕ. We now define W to be a *solution of the linearized problem* at ϕ if

$$D(DS(\phi) \cdot v) \cdot w = 0$$

for all v vanishing on the displacement boundary. More generally, we say that w is a solution of the linearized problem with *incremental body force* $B(w)$ and *incremental traction* $\tau(w)$ if

$$D(DS(\phi) \cdot v) \cdot w = \int_{\mathcal{B}} B(w) \cdot v \; dX + \int_{\partial_\tau \mathcal{B}} \tau(w) \cdot v \; dA$$

for all v vanishing on $\partial_d \mathcal{B}$.

We now use the fact that if S is smooth the order of the two derivatives of S in the directions of v and w can be interchanged, for any two variations v and w not necessarily vanishing anywhere. In other words, $D(DS(\phi) \cdot v) \cdot w = D(DS(\phi) \cdot w) \cdot v$. This is what the multisymplectic form is in this case, and it implies that

$$\int_{\mathcal{B}} B(w) \cdot v \; dX + \int_{\partial_\tau \mathcal{B}} \tau(w) \cdot v \; dA = \int_{\mathcal{B}} B(v) \cdot w \; dX + \int_{\partial_\tau \mathcal{B}} \tau(v) \cdot w \; dA,$$

which is exactly the statement of Betti reciprocity (see, for example, Marsden and Hughes [1994] or Truesdell and Noll [1965]).

In classical mechanics it is also common to write a dynamic reciprocity theorem which holds at a given instant of time (see, for instance, Marsden and Hughes [1994]). This is done by including the linear momentum in the body force terms in the above system. This is not the same as a fully space–time reciprocity theorem, which can be derived exactly as above by simply considering the dynamic continuum mechanics case and following the same steps. By taking space–time slices of the form $[t, t + (\Delta t)] \times \mathcal{B}$ and letting Δt go to zero, the fully space–time reciprocity theorem then can be used to derive the standard dynamic reciprocity theorem.

[1] Of course, since we are in a functional space setting this is the Fréchet derivative of S.

4.2 Time adaption and discrete path independent integrals

In perfect analogy to the continuous case, we obtain next the energy balance equation and configurational force equilibrium for the discrete system. As we shall see, this task is accomplished by identifying the discrete reference configuration $\mathcal{X}$ with the mesh used to approximate it, and by obtaining the Euler–Lagrange equations corresponding to continuously varying this mesh. We shall develop these ideas further subsequently.

4.2.1 Discrete energy conservation for ODEs

Consider first a synchronous, as opposed to asynchronous, discretization of an ordinary differential equation. The mesh on the reference configuration consists of a partition $0 < t_1 < \ldots < t_{N-1} < T$ of the interval $[0, T]$. The discrete action sum can be regarded as a function of both the coordinates $\{q_k\}$ and the set of times $\{t_k\}$. Alternatively, we may consider the discrete action sum as a function of generalized coordinates $\mathbf{q}_k = (t_k, q_k)$.

Next, as proposed in Kane et al. [1999a], we extend the discrete variational principle to the extended configuration by regarding both the coordinates and the times on an equal footing. We request the discrete action sum to be stationary with respect to the generalized coordinates $\mathbf{q}_k$, i.e., with respect to *both* the coordinates q_k and the times t_k. In addition, we assume the discrete Lagrangian L_d to be a function of $t_k - t_{k-1}$ only, the general case will be developed later in the asynchronous setting. The resulting discrete Euler–Lagrange equations are

$$0 = D_2 L_d(q_{k-1}, q_k, t_k - t_{k-1}) + D_1 L_d(q_k, q_{k+1}, t_{k+1} - t_k) \tag{4.19}$$

$$0 = D_3 L_d(q_{k-1}, q_k, t_k - t_{k-1}) - D_3 L_d(q_k, q_{k+1}, t_{k+1} - t_k). \tag{4.20}$$

The first equation coincides of course with equation (2.7). Of particular interest is equation (4.20), which says that the quantity

$$E_k = -D_3 L_d(q_k, q_{k+1}, t_{k+1} - t_k) \tag{4.21}$$

should be conserved for all times, i.e., $E_k = E_{k+1}$. By analogy to the continuous case, E_k is the natural definition of discrete energy. To further motivate this definition, equation (4.20) can be seen as the discrete analog to equation (4.10), which expresses the conservation of Eshelby's energy-momentum tensor, the energy in the one–dimensional case, for a time independent Lagrangian. The discrete Eshelby energy-momentum tensor is therefore E_k.

As an example, for the discrete Lagrangian (2.9) with $\alpha = 0$ the discrete energy is

$$E_d = -D_3 L_d(q_0, q_1, h) = \frac{1}{2}\left(\frac{q_1 - q_0}{h}\right)^{\mathsf{T}} M \left(\frac{q_1 - q_0}{h}\right) + V(q_0).$$

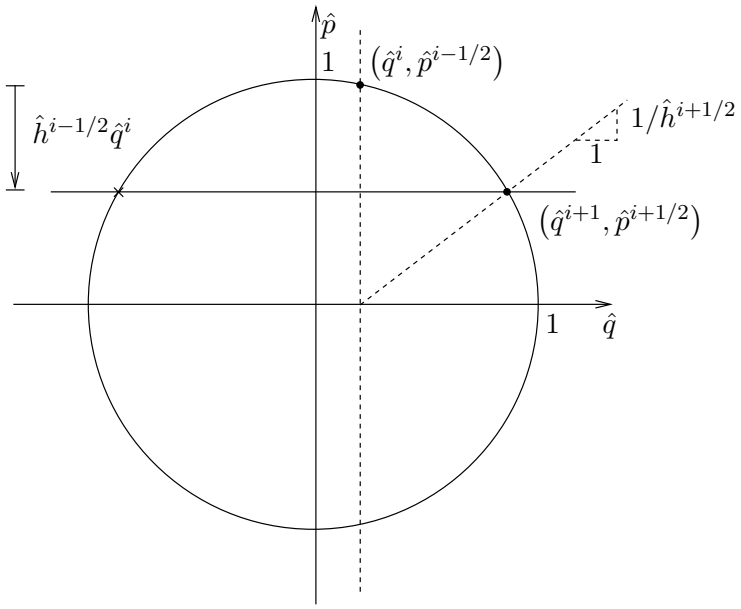

Figure 4.4: Graphical interpretation of the algorithm. There are two intersections of the constant energy and momentum surfaces. The cross denotes a solution rendering a negative value of $\hat{h}^{i+1/2}$, while the circle indicates the positive solution.

In contrast to the continuum case, in which the configurational forces balance equations (4.10) are automatically satisfied whenever the Euler–Lagrange equations (4.2) are, no such property holds in the discrete case. The extension of the discrete variational principle to the extended configuration adds new equations to the discrete mechanical system, namely equations (4.20).

The set of equations (4.19) and (4.20) determines *both* the coordinates $\{q_k\}$ as well as the discrete times $\{t_k\}$. This results in *time adaption*, in as much as the time set $\{t_k\}$ is not prescribed at the outset but is determined as part of the solution instead.

Of course, the viability of the extended configuration approach relies on the solvability of the discrete Euler–Lagrange equations (4.19 - 4.20). However, Kane et al. [1999a] pointed out that it is not always possible to determine a positive time step from the discrete energy-conservation equation, especially near *turning points* where velocities are small. In Kane et al. [1999a] this difficulty was overcome by formulating a minimization problem that returns the exact solution whenever one exists.

The following simple example demonstrates that solvability cannot be always counted on, especially for explicit algorithms. The example concerns a simple harmonic oscillator with mass m and spring constant κ. For this system, the discrete Euler–Lagrange equations for the extended

configuration corresponding to the discrete Lagrangian (2.9) with $\alpha = 0$ are

$$p^{i+1/2} - p^{i-1/2} = -h^{i-1/2}\kappa q^i \tag{4.22}$$

$$\frac{1}{2m}(p^{i-1/2})^2 + \frac{1}{2}\kappa(q^i)^2 = \frac{1}{2m}(p^{i+1/2})^2 + \frac{1}{2}\kappa(q^{i+1})^2 = H, \tag{4.23}$$

where

$$p^{i+1/2} = m\frac{q^{i+1} - q^i}{h^{i+1/2}}, \tag{4.24}$$

and we write

$$h^{i+1/2} = t^{i+1} - t^i. \tag{4.25}$$

It should be noted that equation (4.22) describes a variable time step central-difference scheme, and therefore the algorithm is *explicit*. In terms of the dimensionless variables

$$\hat{p} = \frac{p}{\sqrt{2mH}}, \qquad \hat{q} = q\sqrt{\frac{\kappa}{H}}, \qquad \hat{h} = \frac{h}{\sqrt{m/\kappa}}, \tag{4.26}$$

equations (4.22), (4.23) and (4.24) may be recast in the form:

$$\hat{p}^{i+1/2} - \hat{p}^{i-1/2} = -\hat{h}^{i-1/2}\,\hat{q}^i \tag{4.27}$$

$$(\hat{p}^{i-1/2})^2 + (\hat{q}^i)^2 = (\hat{p}^{i+1/2})^2 + (\hat{q}^{i+1})^2 = 1 \tag{4.28}$$

$$\hat{h}^{i+1/2} = \frac{\hat{q}^{i+1} - \hat{q}^i}{\hat{p}^{i+1/2}}. \tag{4.29}$$

The problem is now to solve these equations for $(\hat{q}^{i+1}, \hat{p}^{i+1/2}, \hat{h}^{i+1/2})$, subject to the constraint $\hat{h}^{i+1/2} > 0$, given $(\hat{q}^i, \hat{p}^{i-1/2}, \hat{h}^{i-1/2})$, $\hat{h}^{i-1/2} > 0$.

This problem can readily be solved graphically in the phase plane $(\hat{q}, \hat{p}) \in \mathbb{R}^2$, Figure 4.4. Equation (4.28) defines a constant energy surface, which in the present case reduces to a circle, and equation (4.27) defines the constant linear momentum surface, which here reduces to a horizontal line. The intersections of this line with the circle return two possible solutions of the system. The value of $\hat{h}^{i+1/2}$ is given by the inverse of the slope of the segment joining $(\hat{q}^i, 0)$ with $(\hat{q}^{i+1}, \hat{p}^{i+1/2})$. Valid solutions correspond to segments with positive slopes.

It is clear from this construction that solutions fail to exist for sufficiently large $|\hat{h}^{i-1/2}\hat{q}^i|$, as under such conditions the constant linear-momentum line does not intersect the constant-energy circle. Since both $\hat{q}^i$ and $\hat{h}^{i-1/2}$ are given as initial conditions, this lack of solvability implies that the explicit algorithm may not be able to conserve energy over some time steps. It does not appear to be known at present whether it is always possible to formulate—most likely *implicit*—discrete Lagrangians such that the discrete Euler–Lagrange equations (4.19 - 4.20) are always solvable.

Time-dependent Lagrangians. When the Lagrangian depends explicitly on time, the value of the energy is not preserved but grows or decays accordingly. In this case, the discrete Lagrangian will *not* be a function of $t_k - t_{k-1}$ only, and new terms will appear in the discrete energy balance equation (4.20) stemming from taking derivatives with respect to the times of the discretization.

4.2.2 Discrete energy conservation for AVIs

The additional freedom provided by AVIs to choose local time steps not only provides indisputable computational advantages but also sheds light into how energy is transferred between the different elements. In this case we regard the discrete action sum as a function of the coordinates x_a^i of each node a and the time of each element t_K^j. In other words, we consider the action sum to be function of generalized coordinates $\mathbf{q}_a^i = (t_a^i, x_a^i)$, in which we restrict the time component t_a^i to coincide with the time t_K^j of one of the elements K. The extended discrete variational principle acting on the generalized coordinates results in the discrete Euler–Lagrange equations

$$D_a^i S_d = 0 \tag{4.30}$$

$$D_K^j S_d = 0, \tag{4.31}$$

for all $t_a^i \in (0,T)$ and $t_K^j \in (0,T)$, where $D_K^j S_d$ indicates the partial derivative of the discrete action with respect to the elemental time t_K^j. The linear momentum balance equation (3.42) appears again as equation (4.30). The second equation above, equation (4.31), expresses a balance in the energy transfer between the different subsystems. The system of equations (4.30 - 4.31) should be satisfied by solving for *both* the coordinates x_a^i and the times t_K^j.

As an example, for the AVI algorithm described by the discrete action sum (3.35) equation (4.31) reads

$$T_K^{j-} + \Phi_K\left(x_K^j, t_K^j\right) + (t_K^j - t_K^{j-1}) D_2\Phi_K\left(x_K^j, t_K^j\right) = T_K^{j+} + \Phi_K\left(x_K^{j+1}, t_K^{j+1}\right). \tag{4.32}$$

In this expression

$$T_K^{j-} \equiv \sum_{a\in K} \frac{1}{2}\left(v_{K,a}^{j-}\right)^{\mathsf{T}} m_a\, v_{K,a}^{j-} \tag{4.33}$$

$$T_K^{j+} \equiv \sum_{a\in K} \frac{1}{2}\left(v_{K,a}^{j+}\right)^{\mathsf{T}} m_a\, v_{K,a}^{j+} \tag{4.34}$$

are the kinetic energies carried by the nodes of K before and after the element strikes those nodes and changes their linear momenta according to (3.43), and $v_{K,a}^{j-}$ and $v_{K,a}^{j+}$ are the velocities of a node a in K also before and after t_K^j, respectively.

It is evident that equation (4.32) encodes a discrete local balance of energy. It should be noted that the local energy balance equation (4.32) allows for energy transfer between the elements, as required. Specifically, the energy is transferred between elements by the conduit of the variations in kinetic energy. Thus, in general $T_K^{j+} \neq T_K^{(j+1)-}$, which implies that part of the kinetic energy is exchanged between neighboring elements. In particular, $T_K^{(j+1)-} - T_K^{j+}$ equals the work done on element K between two successive elemental updates.

The relative ease with which the discrete dynamics formalism yields a complete and internally consistent set of equations of motion and balance equations, such as (3.43) and (4.32) for the discrete Lagrangian (3.39), can hardly be overstated. Thus, while in hindsight (3.43) and (4.32) are eminently reasonable, arriving at them without the benefit of a formal procedure would require uncommon intuition (or luck).

Energy conservation properties. The energy conservation properties of AVI can be analyzed by looking at the effects of translating the time axis on the action sum. To this end, introduce the time parametrization $(\Delta\Theta, \tau)$, where $\tau \in \mathbb{R}$ is some reference time and $\Delta\Theta = \Theta - \tau = \{t - \tau,\ t \in \Theta\}$. Let $\bar{S}_d(\Xi, \Delta\Theta, \tau) = S_d(\Xi, \Theta)$ be the action sum in the new parametrization. Finally, let $S_{d,\alpha}$ be the one–parameter family of action sums defined as

$$S_{d,\alpha} = S_d\left(\Xi, \Theta + \alpha\right) \tag{4.35a}$$

$$= \bar{S}_d(\Xi, \Delta\Theta, \tau + \alpha) \tag{4.35b}$$

$$= \bar{S}_d(\Xi, \Delta\Theta + \alpha, \tau) \tag{4.35c}$$

for all $\alpha \in \mathbb{R}$, where $\Theta + \alpha = \{t + \alpha \mid t \in \Theta\}$. This leads to

$$\left.\frac{dS_{d,\alpha}}{d\alpha}\right|_{\alpha=0} = \sum_{K\in\mathcal{T}} D_K^1 S_d + \sum_{K\in\mathcal{T}} D_K^{N_K} S_d + \sum_{K\in\mathcal{T}} \sum_{1<j<N_K} D_K^j S_d \tag{4.36a}$$

$$= D_\tau \bar{S}_d(\Xi, \Delta\Theta, \tau), \tag{4.36b}$$

where D_K^j denotes differentiation with respect to t_K^j. Assume now that the discrete time set Θ is chosen such that equations (4.31) are satisfied for all $K \in \mathcal{T}$ and all $1 < j < N_K$. Then it follows that

$$\sum_{K\in\mathcal{T}} D_K^1 S_d + \sum_{K\in\mathcal{T}} D_K^{N_K} S_d = D_\tau \bar{S}_d. \tag{4.37}$$

Notice that equation (4.37) is the global energy conservation equation for a possibly-time-dependent Lagrangian. In the particular case in which the discrete Lagrangian is invariant under time transla-

tion, $D_\tau \bar{S}_d = 0$ and (4.37) reduces to

$$E_d = -\sum_{K\in\mathcal{T}} D_K^{N_K} S_d = \sum_{K\in\mathcal{T}} D_K^1 S_d, \tag{4.38}$$

where E_d is the conserved value of the global energy of the discrete system. Equation (4.37) expresses the precise way in which the discrete system satisfies global energy balance between the initial and final configurations.

It is also possible to establish global energy balance between any two configurations of the system, not necessarily coincident with the initial and final configurations. An identity analogous to (4.36) holds for each partial action sum. However, satisfying equation (4.31) does not necessarily imply that $D_K^j S_{d,m} = 0$ for all of the elemental times in $\Theta_{K,m}$. Equation (4.31) expresses a relationship between the derivatives of *all* the discrete Lagrangians that have t_K^j as a degree of freedom, whereas possibly not all of these contribute to $S_{d,m}$. In particular, if $t_K^j < t_f^m = \min_K t_K^{N_{K,m}}$, equation (4.31) does imply that $D_K^j S_{d,m} = 0$. Then, specializing (4.37) for two configurations $m_1 < m_2$ gives

$$\sum_{K\in\mathcal{T}} \sum_{\substack{t_K^j\in\Theta_{K,m_1} \\ t_K^j \geq t_f^{m_1},\ j>1}} D_K^j S_{d,m_1} + \sum_{K\in\mathcal{T}} D_K^1 S_{d,m_1} \quad = \quad D_\tau \bar{S}_{d,m_1} \tag{4.39}$$

$$\sum_{K\in\mathcal{T}} \sum_{\substack{t_K^j\in\Theta_{K,m_2} \\ t_K^j \geq t_f^{m_2},\ j>1}} D_K^j S_{d,m_2} + \sum_{K\in\mathcal{T}} D_K^1 S_{d,m_2} \quad = \quad D_\tau \bar{S}_{d,m_2}. \tag{4.40}$$

Assuming that m_1 and m_2 are such that $t_f^{m_2} \geq t_f^{m_1} > t_0$, and subtracting these equations, we obtain

$$\sum_{K\in\mathcal{T}} \left[\sum_{\substack{t_K^j\in\Theta_{K,m_2} \\ t_K^j \geq t_f^{m_2}}} D_K^j S_{d,m_2} - \sum_{\substack{t_K^j\in\Theta_{K,m_1} \\ t_K^j \geq t_f^{m_1}}} D_K^j S_{d,m_1} \right] = D_\tau(\bar{S}_{d,m_2} - \bar{S}_{d,m_1}), \tag{4.41}$$

which expresses a global energy balance between configurations m_1 and m_2. Finally, for the special case of a discrete Lagrangian invariant under time translation (4.41) reduces to

$$-E_d = \sum_{K\in\mathcal{T}} \sum_{\substack{t_K^j\in\Theta_{K,m_1} \\ t_K^j \geq t_f^{m_1}}} D_K^j S_{d,m_1} = \sum_{K\in\mathcal{T}} \sum_{\substack{t_K^j\in\Theta_{K,m_2} \\ t_K^j \geq t_f^{m_2}}} D_K^j S_{d,m_2}, \tag{4.42}$$

which generalizes (4.38).

In order to determine the form of the global energy balance equation for discrete Lagrangian

(3.39), we note that the right–hand side of equation (4.37) evaluates to

$$D_\tau \bar{S}_d = - \sum_{\substack{t_K^j \in \Theta \\ t_K^j \neq t_0}} \left(t_K^j - t_K^{j-1} \right) D_2 V_K \left(\mathbf{x}_K^j, t_K^j \right), \tag{4.43}$$

whereupon the global energy conservation equation (4.37) becomes

$$\begin{aligned} \sum_{\substack{t_K^j \in \Theta \\ t_K^j \neq t_0}} & \left(t_K^j - t_K^{j-1} \right) D_2 V_K \left(\mathbf{x}_K^j, t_K^j \right) \\ & + \sum_{a \in \mathcal{T}} \sum_{K \in \mathcal{T}_a} \frac{1}{2} \left(\mathbf{v}_{K,a}^{1+} \right)^{\mathsf{T}} m_{K,a} \left(\mathbf{v}_{K,a}^{1+} \right) + \sum_{K \in \mathcal{T}} V_K \left(\mathbf{x}_K^2, t_K^2 \right) = \\ & \sum_{a \in \mathcal{T}} \sum_{K \in \mathcal{T}_a} \frac{1}{2} \left(\mathbf{v}_{K,a}^{N_K-} \right)^{\mathsf{T}} m_{K,a} \left(\mathbf{v}_{K,a}^{N_K-} \right) + \sum_{K \in \mathcal{T}} V_K \left(\mathbf{x}_K^{N_K}, t_K^{N_K} \right), \end{aligned} \tag{4.44}$$

where $\mathcal{T}_a = \{K \in \mathcal{T} \mid a \in K\}$. For simplicity, in equation (4.44) we assumed that the velocities of the nodes do not change for times $t \geq t_f$. The global conservation of energy for intermediate configurations takes an analogous form.

The parallel with the continuous system is insightful here too. After a close inspection, we note that equation (4.36) is the discrete analog to equation (4.9), which expresses the variations of the actions under variations of the reference configuration. While in the continuous case equation (4.12) in Noether's theorem is a consequence of the Euler–Lagrange equations (4.2), we need to recourse to the extended variational principle and obtain equation (4.31) to recover the conserved quantity in the discrete case.

Solving for the time step is not necessary in practice. As seen from the numerical examples in section §3.5, Figure 3.20, and in Lew et al. [2003a], the total energy of the system oscillates around a constant value for very long times without overall growth or decay. This occurs in spite of keeping the time step in each element constant and not enforcing equation (4.31).

The residual of the energy equation (4.32), given by the left–hand side of equation (4.31), is of considerable interest. The evolution of this residual in time, together with the elemental total energy as given by the left–hand side of equation (4.32), is shown in Figure 4.5 for an element chosen at random. This curves were obtained from the third case of the helicopter blade example in section §3.5. In this case, the time steps are chosen to satisfy the Courant condition instead of the energy balance in equation (4.31). The absolute value of the energy "imbalance" is negligible when compared with the total energy of the element, so for all practical purposes, the energy balance is "nearly" satisfied at the local level as well. To further support this statement we have also plotted the residual of the energy equation as a function of time for one element chosen at random in the

Neohookean block and the L-shaped beam examples. These plots are shown in Figures 4.6 and 4.7, respectively. Additionally, we plotted the accumulated residual as a function of time, which indicates the total amount of "imbalanced" energy that has been lost or gained by the element until then. In both cases the local energy behavior shows that the "energy" imbalance is relatively small with respect to the amount of energy flowing into and out from the element. Finally, Figure 4.8 shows a histogram of the distribution of the maximum relative error for each element in the Neohookean block example, up to time $t = 8.8$ ms, or a maximum/minimum number of updates equal to 689,512/34,107 updates. The relative error is defined as the absolute value of the quotient between the residual of the the local energy equation and the instantaneous total energy in the element. More that 50% of the elements have a maximum relative error smaller than 0.1%, while 97.5% of the elements have a maximum relative error smaller that 1%. These numerical tests suggest that both the local and global energy behavior of the AVI algorithm are excellent even when equation (4.31) is not enforced.

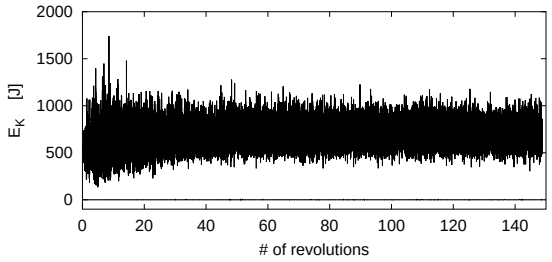

(a) Total energy (top) and residue of the energy equation (bottom) in one element.

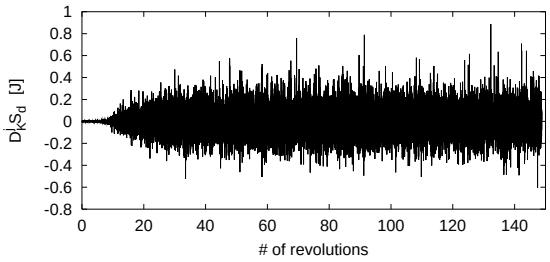

(b) Blow up of the residue of the energy equation shown in the figure on the left.

Figure 4.5: Evolution of the residual of the energy balance equation (4.31) (or energy "imbalance") and the total energy of the same element for one element of the mesh chosen at random. Even though the residual of the energy equation is not exactly zero, the absolute size of the energy "imbalance" is negligible when compared with the total energy in the element. The local energy balance is "nearly" satisfied at all times, even though this equation is never enforced. This curves were obtained from the case 3 of the helicopter blade example in section §3.5.

4.2.3 Implementation of time step adaption for AVIs

Even though the numerical evidence suggests that it is not necessary to solve the complete system (4.30 - 4.31) for both the coordinates and the times in order to obtain energy conservation, if one wished to do it, there is an algorithm that accomplishes this task. It is briefly described below.

The algorithm proceeds similarly to the one explained in Figure 3.4. The basic additional idea is that after updating the positions and velocities of an element according to the linear momentum balance equation, we should reschedule this element and all those sharing nodes with it to satisfy

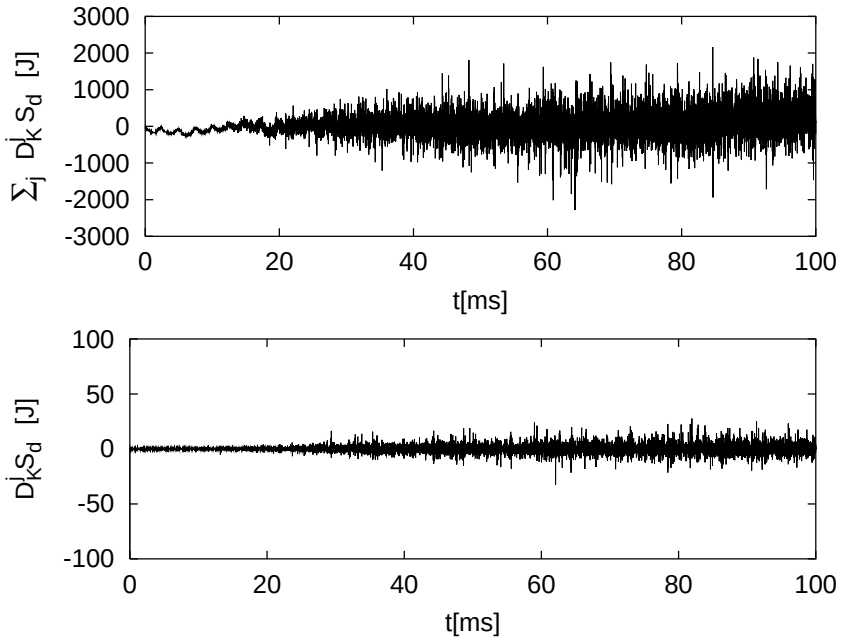

Figure 4.6: Neohookean block example. Instantaneous and accumulated local energy residual as a function of time for an element of the mesh. The accumulated energy residual remains below 0.3% of the value of the elemental energy at all times after an initial transient. Some high-frequency ringing is evident, as is typical of quadratic triangular elements.

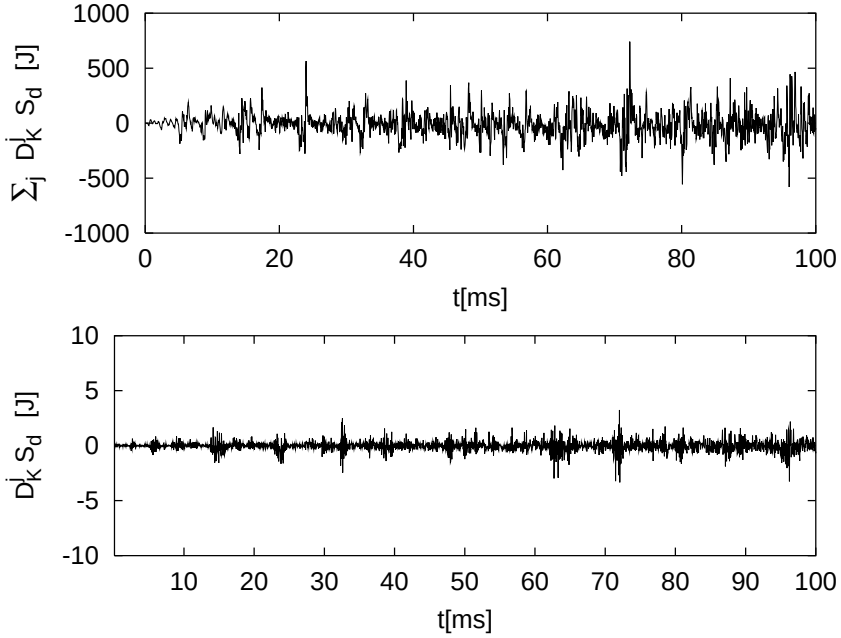

Figure 4.7: L-shaped beam example. Instantaneous and accumulated local energy residual as a function of time for an element of the mesh. The accumulated energy residual remains below 0.03% of the value of the elemental energy at all times.

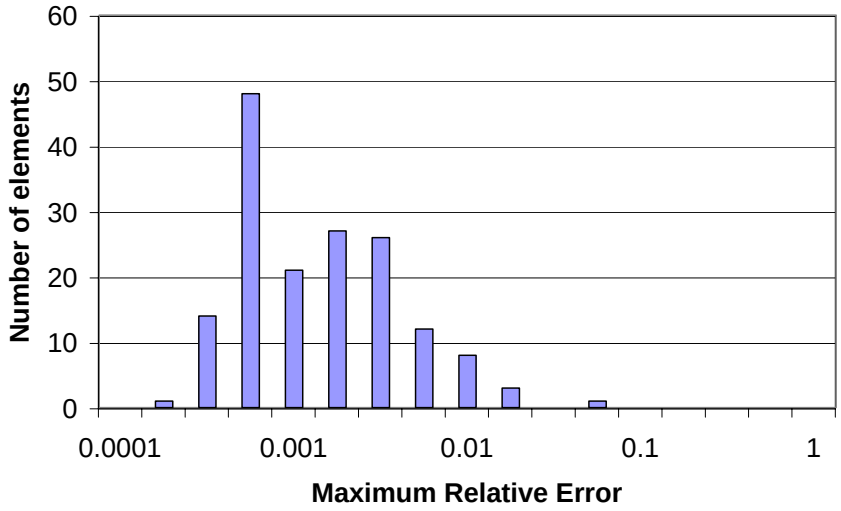

Figure 4.8: Neohookean block example. Histogram of the distribution of maximum relative error in satisfying the local energy equation on each element up to time $t = 8.8$ ms. The relative error is defined as the absolute value of the quotient between the residual of the the local energy equation and the instantaneous total energy in the element. More than 50% of the elements have a maximum relative error smaller than 0.1%, while 97.5 % of the elements have a maximum relative error smaller that 1%.

the energy balance equation for each of them. In this way, the time t_K^{j+1} at which any element K is extracted from the priority queue corresponds to the solution of the energy balance equation $D_K^j S_d = 0$.

Of course a strategy to overcome the occasional lack of solutions of the energy balance equation is needed to ensure the computation of a time step, similarly to Kane et al. [1999a]. One possibility is discussed in section 4.2.4.

The satisfaction of the energy balance equation introduces, as expected, a growth in the computational cost of the algorithm, since the resulting equations are intrinsically nonlinear in the elemental time.

4.2.4 Energy reservoirs and time step adaption

To implement the algorithm explained in section 4.2.3, which accounts for the local energy balance, it is necessary to guarantee that a valid time step for each element will always be determined. However, as seen in section 4.2.1, trying to satisfy the local energy equation leads to the absence of suitable solutions in many occasions. We discuss next an alternative approach to take equation (4.32) into account during the computations.

4.2.4.1 Energy reservoirs and optimal energy balance

The following algorithm is based on two ideas. The first idea consists on looking for time step solutions in the closed interval $[f_l \Delta t_K^c, f_u \Delta t_K^c]$, where $0 < f_l < f_u \leq 1$, $\Delta t_K^c \approx h/c$ as given by equation (3.59), and (f_l, f_u) are parameters of the algorithm. This precludes the time step from acquiring very large or very small values, but still provides a range in which it can be adjusted to satisfy the energy balance. The second idea is to create an energy reservoir per element, R_K, where the element can store a part of its energy whenever a time step that satisfies the local energy equation cannot be found. The amount of energy added to R_K at each time step is given by the residue of the local energy equation, i.e.,

$$R_K^{j+1} = R_K^j + \underbrace{T_K^{j-} + \Phi_K\left(x_K^j, t_K^j\right) + (t_K^j - t_K^{j-1}) D_2\Phi_K\left(x_K^j, t_K^j\right) - T_K^{j+}}_{\Phi_K^{pred,j+1}} - \Phi_K\left(x_K^{j+1}, t_K^{j+1}\right) \quad (4.45)$$

$$= R_K^j + D_{K,j} S_d. \quad (4.46)$$

A part or all of this stored energy is returned to the element at later times, by considering it as a source term in the energy equation. Thus, equation (4.32) is replaced by an optimization problem, in which the absolute value of R_K^{j+1} is minimized by adjusting the value of t_K^{j+1}. More precisely, let

$$R_K^{\text{abs},j+1}(\tau) = \left| R_K^j + \Phi_K^{pred,j+1} - \Phi_K\left(x_K^{j+1}(\tau), \tau\right) \right|, \quad (4.47)$$

where $x_K^{j+1}(\tau)$ returns the value of x_K^{j+1} as a function of τ, a trial value for t_K^{j+1}, according to the local linear momentum balance equations (3.43)– (3.44). The objective is to find $t_K^{j+1} \in I = [f_l \Delta t_K^c, f_u \Delta t_K^c]$ such that

$$R_K^{\text{abs},j+1}(t_K^{j+1}) = \min_{\tau \in I} R_K^{\text{abs},j+1}(\tau). \quad (4.48)$$

In this way the energy in the reservoir is returned to the element as soon as it is possible to do so. Whenever $R_K^j = 0$, solving the optimization problem is equivalent to exactly solving the energy equation (4.32), as long as a solution exists in the bounded interval I. This is a one–dimensional optimization problem, and can be solved by many well-known optimization techniques.

The simulation of the Neohookean block of section 3.5.1 has been used to test the algorithm under consideration. A plot of the total energy as a function of time for the solution thus obtained is shown in Figure 4.9. A glance at the picture immediately tells that the energy is drifting and it is not longer preserved, as it happens when the time step on each element is kept constant. The energy drift has been observed for relatively long times. For instance, by the end of the horizontal axis in Figure 4.9 the maximum/minimum number of updates for a single element was 1,938,815/116,958. This result leads to the conclusion that the dynamics imposed by the optimization procedure described herein

is unstable, and damages the nice energy behavior rather than improving it. It should be noted, however, that this does not preclude the possibility of crafting other dynamics for the reservoirs, which are stable, and such that the local energy conservation can be *almost always* achieved without damaging the other conservation properties. Such a construction is not yet known.

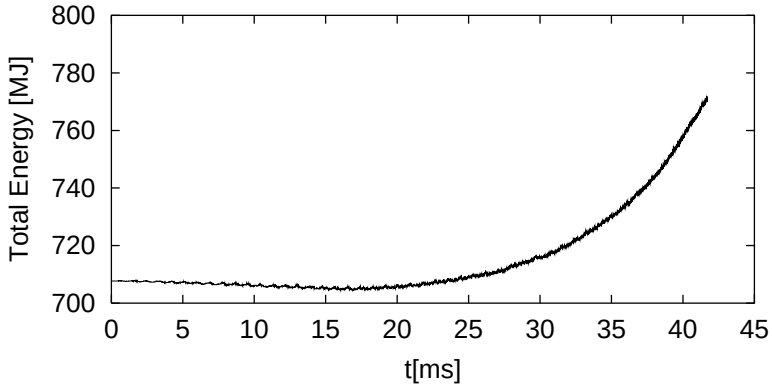

Figure 4.9: Total energy as a function of time for the Neohookean block example, when the dynamics of the local energy reservoirs are chosen to be determined by the optimization procedure.

4.2.5 Conserved discrete path integrals

The theory of discrete mechanics provides a way to define discrete path integrals, and therefore discrete J and L integrals, whose value is independent of the discrete path chosen. We begin by identifying the finite element mesh on the undeformed shape of the continuum body as the discrete reference configuration. The discrete parametric configuration can be identified with several copies of the reference finite element. Then, the discrete version of the mapping γ in section §4.1.3 is constructed with the isoparametric mappings from the reference element to each of the elements in the mesh, while the discrete analog to the mapping ϕ is the traditional finite element isoparametric interpolation. The variables of the isoparametric mapping are of course the positions X_a of the nodes in the reference configuration, while those of the isoparametric interpolation are the positions of the nodes x_a in the deformed one.

Let $\tau \subset \mathcal{T}$ be a subset of elements of the finite element mesh, and let

$$S_{d,\tau} = \sum_{K \in \tau} V_K = \sum_{K \in \tau} \int_K W(\nabla \varphi_h, X)\, dX$$

be the discrete action sum, in this case the potential energy, corresponding to τ. We regard now $S_{d,\tau}$ as a function of (x_a, X_a). Consider next the one–parameter family of mappings $(X_a)^\varepsilon = \exp(\Omega\varepsilon)X_a + \varepsilon v$, for a skew–symmetric matrix Ω and a vector $v \in \mathbb{R}^3$. If the strain-energy density W does not depend explicitly on X, i.e., the material is homogeneous, then the discrete action sum

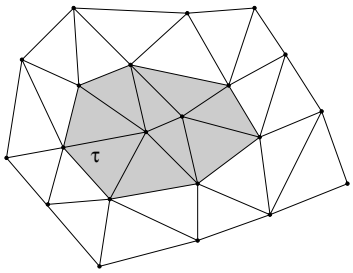

Figure 4.10: Example of a subset of elements τ in a finite element mesh. The elements in the shaded region contribute with their elemental potential energy to the discrete action sum $S_{d,\tau}$.

is invariant under the rotation or translation of the mesh with the family of mappings $(X_a)^\varepsilon$. This uses the fact that W is assumed to be material frame indifferent. Therefore

$$0 = \frac{\partial}{\partial \varepsilon} S_{d,\tau}\bigg|_{\varepsilon=0} = \sum_{a\in\tau} \frac{\partial S_{d,\tau}}{\partial X_a} \cdot v + \sum_{a\in\tau} X_a \times \frac{\partial S_{d,\tau}}{\partial X_a} \cdot \omega, \tag{4.49}$$

where $\omega \in \mathbb{R}^3$ is the axial vector of Ω, which in terms of the Hodge star operator is $\omega = *\Omega$. Since this holds for all v and ω, we have that

$$0 = \sum_{a\in\tau} \frac{\partial S_{d,\tau}}{\partial X_a} \tag{4.50}$$

$$0 = \sum_{a\in\tau} X_a \times \frac{\partial S_{d,\tau}}{\partial X_a}. \tag{4.51}$$

As we have seen with the energy conservation, in the discrete case we need to request the equilibrium of configurational forces, the analog to equation (4.10), separately, since it is not implied by the discrete Euler–Lagrange equations. Equilibrating the discrete configurational forces by repositioning the nodes of the mesh has been originally proposed, analyzed and implemented by Thoutireddy and Ortiz [2003]. Following their development, we request then

$$\frac{\partial S_d}{\partial X_a} = 0 \tag{4.52}$$

for all nodes a in $\mathcal{T} \setminus \partial\mathcal{B}$. Nodes on the boundary of the domain admit constrained variations only, since they should preserve the original geometry of the reference configuration. We note that S_d in equation (4.52) is the action sum over the whole mesh, not only over τ. For a node a in the interior of τ, we have that $\partial S_d/\partial X_a = \partial S_{d,\tau}/\partial X_a$. This is not the case for a node a on the boundary of τ, since S_d may contain contributions of elements having a as a node which are not in τ. By eliminating

the corresponding terms in equations (4.50) and (4.51) we are left with

$$0 = \sum_{a \in \partial\tau} \frac{\partial S_{d,\tau}}{\partial X_a} \tag{4.53}$$

$$0 = \sum_{a \in \partial\tau} X_a \times \frac{\partial S_{d,\tau}}{\partial X_a}. \tag{4.54}$$

Since equations (4.53) and (4.54) are valid independently of the choice of τ, we obtain the discrete analogs to equations (4.16)-(4.17), respectively. The definition of the discrete path independent J-integral and L-integral follows directly from here.

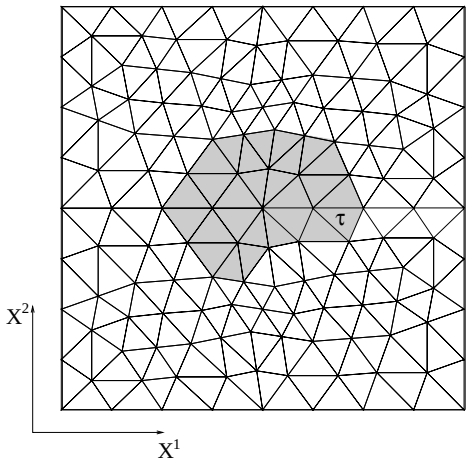

Figure 4.11: Example finite element mesh for a two–dimensional fracture mechanics simulation. If the configurational forces are in equilibrium, then expression (4.53) evaluated on $\partial\tau$ is equal to the J-integral. The value of the J-integral is the same when computed on the boundary of any submesh τ that contains the node at the crack tip.

As an application of (4.53), we discuss next the computation of the value of the J-integral on a two–dimensional crack tip (see Figure 4.11). As proposed in Thoutireddy and Ortiz [2003], the value of the J-integral can be computed, from a finite element elastostatics simulation, as the configurational force conjugate to varying the node at the crack tip in the direction of crack advance, in this case the X^1-direction. We consider then a submesh τ containing the node at the crack tip, which we denote b. From (4.53) we have that

$$J = \frac{\partial S_{d,\tau}}{\partial X^1_b} = -\sum_{a \in \partial\tau \setminus b} \frac{\partial S_{d,\tau}}{\partial X^1_a}.$$

The sum on the right–hand side includes null contributions from those nodes that belong to the crack faces. These nodes can be varied in the X^1 direction, since this preserves the geometry, and therefore the X^1-component of their conjugate configurational force should be zero. Only those nodes on $\partial\tau$ that do not belong to the crack face will contribute to the right–hand side, in an exact

analogy to the continuous J-integral.

4.2.6 Discrete horizontal and vertical variations: discussion

Perhaps one of the most perplexing features of the discrete mechanics picture when compared against the continuous mechanics picture is the fact that DEL (discrete Euler–Lagrange) equations corresponding to horizontal variations are not automatically satisfied whenever the DEL equations corresponding to vertical variations are. As discussed in section 4.1.3, this is true in the continuous case. In addition, it should be clear at this point that this feature is responsible for the need to adjust the time step to achieve exact local energy balance and to accommodate the nodes in the mesh to get the discrete path-independent integrals.

The reasons for this discrepancy between the discrete and the continuous pictures can be understood graphically, and it is shown in Figure 4.12. Recall that in the continuous case any vertical variation can also be written as a horizontal variation. Therefore, finding a stationary point of the action with respect to all vertical variations automatically implies that it also is a stationary point with respect to all horizontal ones. In the discrete case a vertical variation is not always equivalent to a horizontal variation. This is illustrated in Figure 4.12 for a finite element discretization. Consequently, the stationarity conditions should be imposed independently for both sets of variations. It is not yet known whether it is possible to construct a discretization for which both sets of variations are equivalent.

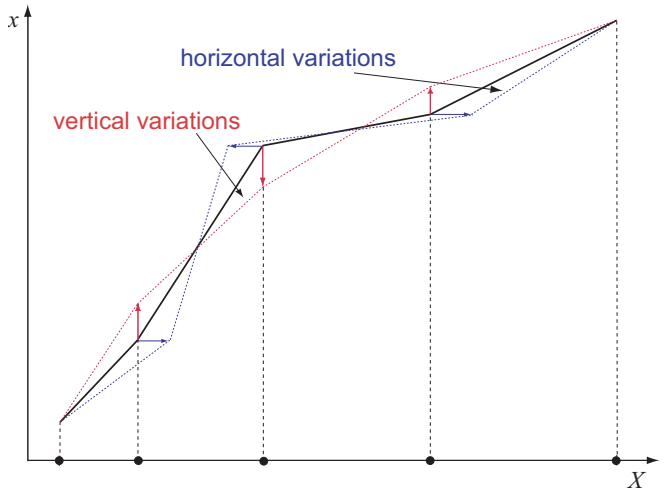

Figure 4.12: Graphical representation of horizontal and vertical variations for a finite element discretization. The discrete functional space is composed by all continuous and elementwise affine functions. Notice that a horizontal variation generally leads to a function outside the original discrete functional space, and therefore, can never be restated as a vertical variation.

4.3 Discrete multisymplecticity

In the same way every variational integrator for finite–dimensional mechanical systems is symplectic, every variational integrator for continuum mechanics is multisymplectic. In other words, the variational structure uniquely defines the $m+2$-form that is preserved by the motion of the discrete mechanical system, where $m+1$ is the dimension of $\mathcal{X}$. This form is derived as the boundary term when considering free action variations, just as in the continuous case.

The derivation of the discrete multisymplectic form formula, though interesting and relevant, is a rather cumbersome procedure to perform without recourse to intrinsic notation. We shall not obtain the formula here, but refer the reader to Lew et al. [2003a].

The discrete multisymplectic formula defines a discrete version of Betti's reciprocity theorem in linear elastostatics, similar to the continuous case discussed in section 4.1.6. This is equivalent to the symmetry of the stiffness matrix, which, as is well known, results automatically from variational discretizations.

4.4 Discrete Noether's theorem (Asynchronous case)

The statements of conservation of linear and angular momentum for AVIs discussed in section 3.4 can, more generally, be deduced from a discrete version of Noether's theorem for asynchronous discretizations. Moreover, Noether's theorem can be formulated for both horizontal and vertical variations provided the discrete Euler–Lagrange equations associated with horizontal variations are also satisfied. Nevertheless, this section will consider Noether's theorem for vertical symmetries only.

Denote with $\mathcal{X}_K^j = [t_K^j, t_K^{j+1}] \times K$ the subset of space–time corresponding to the j-th time step of element K. Let $\Theta_{\mathcal{Y}} \subseteq \Theta$ be any subset of the set of elemental times. Define

$$\mathcal{Y} = \bigcup_{t_K^j \in \Theta_{\mathcal{Y}}} \mathcal{X}_K^j, \qquad \Xi_{\mathcal{Y}} = \bigcup_{t_K^j \in \Theta_{\mathcal{Y}}} \Xi_K^j,$$

and let

$$S_{d,\mathcal{Y}}(\Xi_{\mathcal{Y}}, \Theta_{\mathcal{Y}}) = \sum_{t_K^j \in \Theta_{\mathcal{Y}}} L_d^{K,j}$$

be the discrete action associated with $\mathcal{Y}$. Let $\Xi_{\mathcal{Y}}^{\varepsilon}$ be a one–parameter group of nodal positions, with $\Xi_{\mathcal{Y}}^0 = \Xi_{\mathcal{Y}}$, and such that

$$S_{d,\mathcal{Y}}(\Xi_{\mathcal{Y}}^{\varepsilon}, \Theta_{\mathcal{Y}}) = S_{d,\mathcal{Y}}(\Xi_{\mathcal{Y}}, \Theta_{\mathcal{Y}}) \tag{4.55}$$

for all ε. The infinitesimal symmetry associated with this invariance is

$$\xi_a^i = \frac{\partial x_a^{i,\epsilon}}{\partial \varepsilon}\Big|_{\varepsilon=0},$$

and, after differentiating equation (4.55) with respect to ε, the following identity is obtained

$$\frac{\partial S_{d,\mathcal{Y}}}{\partial \varepsilon}(\Xi^{\varepsilon}_{\mathcal{Y}}, \Theta_{\mathcal{Y}})\Big|_{\varepsilon=0} = \sum_{X^i_a \in \mathcal{Y}} D^i_a S_{d,\mathcal{Y}} \cdot \xi^i_a = 0. \tag{4.56}$$

Assume next that the set $\Xi_{\mathcal{Y}}$ is part of a trajectory of the discrete mechanical system. The discrete Euler–Lagrange equations (3.42) imply then that $D^i_a S_{d,\mathcal{Y}} = 0$ for all $X^i_a \in \overset{\circ}{\mathcal{Y}}$. Introducing this last identity into equation (4.56) we obtain

$$\sum_{X^i_a \in \partial \mathcal{Y}} D^i_a S_{d,\mathcal{Y}} \cdot \xi^i_a = 0, \tag{4.57}$$

which is the statement of Noether's theorem over $\mathcal{Y}$.

Chapter 5

Concluding remarks and future directions

We have developed in this thesis the theory of Discrete Mechanics to address solid mechanics problems. We began by reviewing in very simple and elementary terms the formulation of variational integrators for finite–dimensional mechanical systems. Additionally, we developed the formulation of two–point constraints within this framework, necessary for some solid and fluid mechanics applications (e.g., to deal with incompressibility), discussed necessary and sufficient conditions for an algorithm, "as written," to be variational, and for a variational algorithm to derive from an incremental minimum principle. We found that unveiling the variational structure of an algorithm is equivalent to finding the underlying symplectic structure. Even in the continuous case, it is only possible to test if, given a symplectic structure, a set of equations is Euler–Lagrange, but it is not generally known how to answer the converse question. The discrete picture was found to be exactly similar, as the example on the variational nature of Newmark's algorithms shows.

We proposed a class of asynchronous discretizations of space–time, and developed the corresponding abstract components of the theory, namely, the elemental discrete Lagrangians, the discrete action sum, the discrete variational principle, Noether's theorem, the symplectic structure and the extension to dissipative or forced systems. The framework is rather general, allowing each element to have a different time step, with no constraints on the ratio of time step between adjacent elements. In particular, we formulated a discrete Lagrangian of the explicit type and implemented the resulting algorithm. The implementation was accomplished via the notion of a *priority queue*. Several numerical examples in nonlinear elastodynamics were used to illustrate the excellent accuracy, conservation and convergence properties the algorithms possess. Also, their suitableness to efficiently address problems where multiresolution is needed was demonstrated via cases that could only be performed thanks to the asynchronous nature of the algorithms In these tests AVI were found to result in substantial speedups, at equal accuracy, relative to explicit Newmark. In some sense, AVI breaks traditional rules of trade-off, since it provides highly desirable properties while

still lowering computational cost.

Not directly related to the variational framework, but still relevant to the type of applications we showed here, is the formulation of the artificial viscosity scheme tailored to finite-deformation Lagrangian calculations of shocks in materials, on unstructured tetrahedral meshes of arbitrary order. The artificial viscous stresses satisfy material-frame indifference exactly, i.e., are invariant under superposed rigid-body rotations. The artificial viscosity scheme returns stable and ostensibly oscillation-free solutions on meshes which greatly underresolve the actual shock thickness. The scheme typically spreads the shock over 4 to 6 elements and captures accurately the shock velocities and jump conditions.

An extension of Hamilton's principle that provides an elegant generalization of Lagrangian mechanics was presented, including temporal, material and spatial variations and symmetries as special cases. This unites energy, configurational forces and the Euler–Lagrange equations within a single picture. In particular, it provides an insightful interpretation of configurational forces and the associated conserved quantities. By mimicking this formulation, the discrete variational principle was restated to obtain the discrete balance of linear momentum, energy and configurational forces as Euler–Lagrange equations. In this context, we showed that in the continuum picture vertical and horizontal variations are equivalent, and discussed why this is not true in the discrete case. The equivalence of the variations implies that whenever linear momentum balance is satisfied, so are the balance of energy and configurational forces. In the discrete setting, the newly obtained Euler–Lagrange equations for energy and configurational forces have to be enforced independently, by taking advantage of the novel additional degree of freedom, the elemental time step, and by rearranging the positions of the nodes in the reference configuration. In particular, we analyzed the solvability of the discrete energy balance equation to determine the elemental time step, and found this not always possible to do. Nevertheless, even without deliberately adjusting the time step, the local energy balance is remarkably well satisfied when the time steps are chosen according to the Courant condition. The total energy of the system was found to oscillate around a mean value for very long times, as long as computations were performed, a fact that can probably be traced to the symplectic nature of the algorithm.

Elastostatics has been shown to be a special case of the extended space–time Lagrangian framework. The inclusion of the reference configuration as an unknown in the variational principle leads to a very simple and straightforward understanding of the origin of configurational forces and associated conservation laws. In this setting, the J, L and M integrals are a direct consequence of Noether's theorem. For elastodynamics, dynamic versions naturally emanated from the framework as well. We have also, for the first time, obtained discrete path integrals that are independent of the discrete path chosen. These were derived from the discrete Noether theorem as the conserved quantities associated with the same symmetries considered in the continuous case. As an example,

the expression for the discrete path independent J-integral around a two–dimensional crack tip was obtained.

One of the most appealing aspects of Discrete Mechanics, widely used throughout the thesis, is that the clear understanding of the continuous systems is used to guide the development of discrete analogues of the geometric structure, such as discrete conservation laws and discrete symplectic forms. This point of view truly induces a change in the understanding and generation of numerical algorithms. Once the action sum has been defined, all mechanical quantities automatically follow from the theory, eliminating the room for guessing in the computation of discrete quantities and revealing that many of the properties of the continuous system are preserved by the discrete approximation. This point of view is expected to be further developed in the near future, in particular in relation to the formulation of a Discrete Exterior Calculus (DEC) (see Desbrun et al. [2003] for a preliminary version) that will provide, for instance, a discrete version of Stokes theorem.

Perhaps the next immediate step needed to definitively show the full advantage of using AVI for problems of engineering interest is to implement and optimize a parallel version of the algorithm. A trivial first parallel asynchronous algorithm was easily constructed and presented, but certainly much optimized versions can be built. The coupling of AVI with Adaptive Mesh Refinement schemes would then be the only missing ingredient to truly begin a new generation of computational mechanics technology.

From the numerical analysis perspective, a systematic study to check for the appearance of resonance instabilities, as reported by other authors in related algorithms, should be performed. So far, we have not been able to find them in our numerical examples. More interesting, and perhaps more relevant, would be to take advantage of the variational framework to understand the convergence of asynchronous schemes in nonlinear elasticity. In particular, Γ-convergence promises to be the method of choice to carry out this endeavor. The study of AVI or, more generally, multisymplectic discretizations with backward error analysis techniques would surely enhance the understanding of the approximating properties of the theory, specially with regards to its energy conservation properties.

The theory is by no means concluded. There are numerous applications still to be developed, such as to the evolution of microstructure, to electrodynamics, fluid mechanics and numerical relativity, where more complex symmetries are involved. The main difficulty here lies in constructing discrete action sums that preserve the symmetries the continuous systems have. Similarly to continuum mechanics, the clear understanding of the continuous picture is used to guide the development of discrete analogues of the geometric structure. This is one of the most appealing and distinguishing aspects of this methodology, and truly makes pursuing this task a worthy one.

Bibliography

J. H. Argyris and D. W. Scarpf. Finite elements in time and space. *Aer. J. Royal Aer. Soc.*, 73:1041–1044, 1969.

F. Armero and I. Romero. On the formulation of high-frequency dissipative time-stepping algorithms for nonlinear dynamics. Part I: low-order methods for two model problems and nonlinear elastodynamics. *Computer Methods in Applied Mechanics and Engineering*, 190:2603–2649, 2001a.

F. Armero and I. Romero. On the formulation of high-frequency dissipative time-stepping algorithms for nonlinear dynamics. Part II: second-order methods. *Computer Methods in Applied Mechanics and Engineering*, 190:6783–6824, 2001b.

T. Belytschko. Partitioned and adaptive algorithms for explicit time integration. In W. Wunderlich, E. Stein, and K. J. Bathe, editors, *Nonlinear Finite Element Analysis in Structural Mechanics*, pages 572–584. Springer-Verlag, 1981.

T. Belytschko and R. Mullen. Mesh partitions of explicit–implicit time integrators. In K. J. Bathe, J. T. Oden, and W. Wunderlich, editors, *Formulations and Computational Algorithms in Finite Element Analysis*, pages 673–690. MIT Press, 1976.

D. J. Benson. Computational methods in Lagrangian and Eulerian hydrocodes. *Computer Methods in Applied Mechanics and Engineering*, 99:235–394, 1992.

J. J. Biesiadecki and R. D. Skeel. Dangers of multiple time steps methods. *Journal of Computational Physics*, 109:318–328, 1993.

T. C. Bishop, R. D. Skeel, and K. Schulten. Difficulties with multiple time stepping and fast multipole algorithm in molecular dynamics. *Journal of Computational Chemistry*, 18(14):1785–1791, 1997.

M. Borri. Helicopter rotor dynamics by finite-element time approximation. *Computers & Mathematics with Applications-Part A*, 12(1):149–160, 1986.

C. L. Bottasso. A new look at finite elements in time: a variational interpretation of Runge-Kutta methods. *Applied Numerical Mathematics*, 25(4):355–368, 1997.

C. L. Bottasso and O. A. Bauchau. Multibody modeling of engage and disengage operations of helicopter rotors. *J. Amer. Helic. Soc.*, 46, 2001.

R. E. Cohen and O. Gülseren. Thermal equation of state of tantalum. http://arxiv.org/ps/cond-mat/0006213, 2000.

G. Dal Maso. *Introduction to* Γ*-convergence*. Birkhäuser, Boston, MA, 1993.

W. J. T. Daniel. Analysis and implementation of a new constant acceleration subcycling algorithm. *International Journal for Numerical Methods in Engineering*, 40:2841–2855, 1997a.

W. J. T. Daniel. The subcycled Newmark algorithm. *Computational Mechanics*, 20:272–281, 1997b.

M. Desbrun, A. N. Hirani, M. Leok, and J. E. Marsden. Discrete Exterior Calculus. (preprint), 2003.

J. D. Eshelby. Energy relations and the energy-momentum tensor in continuum mechanics. In M.F. Kanninen et al., editor, *Inelastic behavior of solids*, pages 77–115. N.Y.:McGraw-Hill, 1970.

R. Fetecau, J. E. Marsden, M. Ortiz, and M. West. Nonsmooth Lagrangian mechanics. (preprint), 2002.

W. Ficket and W. Davis. *Detonation*. University of California Press, 1979.

I. Fried. Finite-element analysis of time-dependent phenomena. *AIAA Journal*, 7(6):1170–, 1969.

P. P. Friedmann. Numerical-methods for the treatment of periodic systems with applications to structural dynamics and helicopter rotor dynamics. *Computers & Structures*, 35(4):329–347, 1990.

Z. Ge and J. E. Marsden. Lie-Poisson integrators and Lie-Poisson Hamilton-Jacobi theory. *Phys. Lett. A*, 133:134–139, 1988.

O. Gonzalez. Time integration and discrete Hamiltonian systems. *J. Nonlinear Sci.*, 6:449–468, 1996.

O. Gonzalez and J. C. Simo. On the stability of symplectic and energy-momentum algorithms for non-linear Hamiltonian systems with symmetry. *Computer Methods in Applied Mechanics and Engineering*, 134(3-4): 197–222, 1996.

H. Grubmüller, H. Heller, A. Windemuth, and K. Schulten. Generalized Verlet algorithm for efficient molecular dynamics simulations with long-range interactions. *Mol. Sim.*, 6:121–142, 1991.

M. E. Gurtin. *Configurational forces as basic concepts of continuum physics*. Springer, 2000.

E. Hairer and C. Lubich. The life-span of backward error analysis for numerical integrators. *Numerische Mathematik*, 76:441–462, 1997.

E. Hairer and C. Lubich. Long time energy conservation of numerical methods for oscillatory differential equations. *SIAM J. Numer. Anal.*, 38(2):414–441 (electronic), 2000. ISSN 1095-7170.

E. Hairer, C. Lubich, and G. Wanner. *Geometric numerical integration: structure–preserving algorithms for ordinary differential equations*. Springer–Verlag, 2002.

T. J. R. Hughes. *The Finite Element Method : linear static and dynamic finite element analysis*. Prentice-Hall, 1987.

T. J. R. Hughes and W. K. Liu. Implicit-explicit finite elements in transient analysis: Stability theory. *Journal of Applied Mechanics*, 78:371–374, 1978.

T. J. R. Hughes, K. S. Pister, and R. L. Taylor. Implicit-explicit finite elements in nonlinear transient analysis. *Computer Methods In Applied Mechanics And Engineering*, 17/18:159–182, 1979.

J. A. Izaguirre, S. Reich, and R. D. Skeel. Longer time steps for molecular dynamics. *Journal of Chemical Physics*, 110(20):9853–9864, 1999.

C. Johnson. *Numerical solution of partial differential equations by the finite element method*. Cambridge University Press, New York, 1987.

C. Kane, J. E. Marsden, and M. Ortiz. Symplectic energy-momentum integrators. *J. Math. Phys.*, 40: 3353–3371, 1999a.

C. Kane, J. E. Marsden, M. Ortiz, and M. West. Variational integrators and the Newmark algorithm for conservative and dissipative mechanical systems. *International Journal for Numerical Methods in Engineering*, 49(10):1295–1325, 2000.

C. Kane, E. A. Repetto, M. Ortiz, and J. E. Marsden. Finite element analysis of nonsmooth contact. *Computer Methods in Applied Mechanics and Engineering*, 180:1–26, 1999b.

J. K. Knowles and E. Sternberg. On a class of conservation laws in linearized and finite elastostatics. *Archive for Rational Mechanics and Analysis*, 44(3):187–210, 1972.

D. Knuth. *The art of computer programming*. Addisson-Wesley, 1998.

A. Lapidus. A detached shock calculation by second-order finite differences. *Journal of Computational Physics*, 2:154–177, 1967.

A. Lew, J. E. Marsden, M. Ortiz, and M. West. Asynchronous variational integrators. *Archive for Rational Mechanics and Analysis*, 2:85–146, 2003a.

A. Lew, J. E. Marsden, M. Ortiz, and M. West. Variational time integrators. *International Journal for Numerical Methods in Engineering*, 2003b. (to appear).

A. Lew, R. Radovitzky, and M. Ortiz. An artificial-viscosity method for the Lagrangian analysis of shocks in solids with strength on unstructures, arbitrary-order tetrahedral meshes. *Journal of Computer-Aided Materials Design*, 8:213–231, 2001.

C. Mader. *Numerical modeling of detonations*. University of California Press, 1979.

J. E. Marsden and T. J. R. Hughes. *Mathematical foundations of elasticity*. Dover Publications, 1994.

J. E. Marsden, G. W. Patrick, and S. Shkoller. Multisymplectic geometry, variational integrators, and nonlinear PDEs. *Communications in Mathematical Physics*, 199(2):351–395, 1998.

J. E. Marsden and T. Ratiu. *Introduction to Mechanics and Symmetry*, volume 17 of *Texts in Applied Mathematics*. Springer-Verlag, 1994.

J. E. Marsden and S. Shkoller. Multisymplectic geometry, covariant Hamiltonians and water waves. *Math. Proc. Camb. Phil. Soc.*, 125:553–575, 1999.

J. E. Marsden and M. West. Discrete mechanics and variational integrators. In *Acta Numerica*, volume 10. Cambridge University Press, 2001.

E. Morano and J. Shepherd. Introduction to high-explosives engineering. 1999.

S. Müller and M. Ortiz. On the γ-convergence of discrete dynamics and variational integrators. To appear, 2003.

M. O. Neal and T. Belytschko. Explicit-explicit subcycling with non-integer time step ratios for structural dynamic systems. *Computers & Structures*, 6:871–880, 1989.

J. Von Neumann and R. D. Richtmyer. A method for the numerical calculation of hydrodynamic shocks. *Journal of Applied Physics*, 21:232–237, 1950.

N. Newmark. A method of computation for structural dynamics. *ASCE Journal of the Engineering Mechanics Division*, 85(EM 3):67–94, 1959.

W. F. Noh. Errors for calculations of strong shocks using an artificial viscosity and an artificial heat flux. *Journal of Computational Physics*, 72:78–120, 1987.

M. Ortiz and L. Stainier. The variational formulation of viscoplastic constitutive updates. *Computer Methods in Applied Mechanics and Engineering*, 171(3-4):419–444, 1999.

A. Pandolfi, C. Kane, J. E. Marsden, and M. Ortiz. Time-discretized variational formulation of non-smooth frictional contact. *International Journal for Numerical Methods in Engineering*, 53:1801–1829, 2002.

R. Radovitzky and M. Ortiz. Error estimation and adaptive meshing in strongly nonlinear dynamic problems. *Computer Methods in Applied Mechanics and Engineering*, 172:203–240, 1999.

S. Reich. Backward error analysis for numerical integrators. *SIAM Journal on Numerical Analysis*, 36(5): 1549–1570, 1999.

J. R. Rice. Conserved integrals and energetic forces. In K.J. Miller B.A. Bilby and J.R. Willis, editors, *Fundamentals of deformation and fracture (Eshelby memorial symposium)*, pages 33–56. Cambridge Univ. Press, 1985.

R. D. Richtmyer and K. W. Morton. *Difference methods for initial-value problems*. Interscience Publishers, second edition, 1967.

G. Sheng, T. C. Fung, and S. C. Fan. Parametrized formulations of Hamilton's law for numerical solutions of dynamic problems: Part II. time finite element approximation. *Computational Mechanics*, 21(6):449–460, 1998.

J. C. Simo, N. Tarnow, and K. K. Wong. Exact energy-momentum conserving algorithms and symplectic schemes for nonlinear dynamics. *Computer Methods in Applied Mechanics and Engineering*, 100:63–116, 1992.

P. Smolinski and Y. S. Wu. An implicit multi-time step integration method for structural dynamics problems. *Computational Mechanics*, 1998.

P. A. Thopmson. *Compressible-fluid dynamics*. Maple Press Co., 1984.

P. Thoutireddy and M. Ortiz. A variational arbitrary Lagrangian Eulerian (VALE) method of mesh adaption and optimization. To appear, 2003.

C. Truesdell and W. Noll. The non-linear field theories of mechanics. In S. Flugge, editor, *Handbuch der Physik III/3*. Springer–Verlag, Berlin, 1965.

M. Tuckerman, B. J. Berne, and G. J. Martyna. Reversible multiple time scale molecular dynamics. *J. Chem. Phys.*, 97:1990–2001, 1992.

M. Wilkins. Use of artificial viscosity in multidimensional fluid dynamic calculations. *Journal of Computational Physics*, 36:281–303, 1980.